Observation of the Nuclear Magnetic Octupole Moment of $^{137}Ba^{+}$

Matthew Hoffman

A dissertation
submitted in partial fulfillment of the
requirements for the degree of

Doctor of Philosophy

University of Washington

2014

Reading Committee:

Boris Blinov, Chair

Subhadeep Gupta

Alejandro Garcia

Program Authorized to Offer Degree:
Physics

University of Washington

Abstract

Observation of the Nuclear Magnetic Octupole Moment of $^{137}Ba^{+}$

Matthew Hoffman

Chair of the Supervisory Committee:
Associate Professor Boris Blinov
Physics

Single trapped ions are ideal systems in which to test atomic physics at high precision, which can in turn be used for searches for violations of fundamental symmetries and physics beyond the standard model, in addition to quantum computation and a number of other applications. The ion is confined in ultra-high vacuum, is laser cooled to mK temperatures, and kept well isolated from the environment which allows these experimental efforts. In this thesis, a few diagnostic techniques will be discussed, covering a method to measure the linewidth of a narrowband laser in the presence of magnetic field noise, as well as a procedure to measure the ion's temperature using such a narrowband laser.

This work has led to two precision experiments to measure atomic structure in $^{138}Ba^{+}$, and $^{137}Ba^{+}$ discussed here. First, employing laser and radio frequency spectroscopy techniques in $^{138}Ba^{+}$, we measured the Landé-g_J factor of the $5D_{5/2}$ level at the part-per-million level, the highest precision to date. Later, the development of apparatus to efficiently trap and laser cool $^{137}Ba^{+}$ has enabled a measurement of the hyperfine splittings of the $5D_{3/2}$ manifold, culminating in the observation of the nuclear magnetic octupole moment of $^{137}Ba^{+}$.

TABLE OF CONTENTS

Page

List of Figures iv

List of Tables vi

Glossary vii

Chapter 1: Introduction 1

Chapter 2: Atomic Theory 3
2.1 Atomic Structure of $^{138}Ba^{+}$ 4
2.1.1 Ba^{+}Atomic Stucture 4
2.1.2 Zeeman Effect 5
2.2 Atomic Structure of $^{137}Ba^{+}$ 8
2.2.1 Isotope Shifts 8
2.2.2 Dipole Hyperfine Structure 10
2.2.3 Multipole Hyperfine Structure 13
2.2.4 $^{137}Ba^{+}$ Hyperfine Structure with Zeeman Effect 15
2.3 Interaction with Radiation 21
2.3.1 Coherent Excitation by Monochromatic Radiation 21
2.3.2 Adiabatic Rapid Passage 24
2.3.3 E1, E2, and M1 Transition Selection Rules 25
2.3.4 Optical Pumping Strategies for $^{138}Ba^{+}$ and $^{137}Ba^{+}$ 28
2.3.5 Destabilization of Dark States 29

Chapter 3: Ion Trapping and Cooling 32
3.1 Ion Trapping 32
3.2 The Linear Paul Trap 33
3.3 Photoionization 37
3.4 Laser Cooling of Trapped Ions 39
3.5 Micromotion Compensation 41

3.6 Quantum Jump Spectroscopy 44

Chapter 4: Apparatus 47
4.1 Laser Systems and their Characterization 47
4.1.1 986/493 nm Laser 47
4.1.2 650 nm Laser 54
4.1.3 455 nm Laser 58
4.1.4 1228/614 nm Laser 60
4.1.5 2051 nm Laser 61
4.1.6 Photoionization Lasers at 791 nm and 337 nm 65
4.2 Radio-frequency Sources 67
4.3 The Linear Paul Trap and Support Apparatus 70
4.3.1 Modifications to Trapping Apparatus and Electrodes 71
4.3.2 Photon Collection System 73
4.3.3 Future Upgrade - Magnetic Shielding 75

Chapter 5: Ion Decoherence Measurements with the 2051 nm Laser 81
5.1 Measurement of the temperature of laser cooled $^{138}Ba^{+}$ 81
5.2 2051 nm laser linewidth measurement with adiabatic rapid passage 85

Chapter 6: Measurement of the Landé g_J factor of $^{138}Ba^{+}$, $5D_{5/2}$ 88
6.1 Experimental Procedure 89
6.2 Systematic Effects 93
6.3 Conclusions and Future Directions 96

Chapter 7: Measurement of the $^{137}Ba^{+}$ hyperfine intervals and observation of the nuclear magnetic octupole moment 98
7.1 Experimental Procedure 100
7.2 Data analysis 105
7.2.1 Extraction of resonance frequencies from spectroscopy 105
7.2.2 Calibration of Magnetic Field and 60 Hz Correction. 105
7.2.3 Extrapolating to find the zero-field hyperfine splittings 108
7.3 Systematic Effects 112
7.3.1 Magnetic Field Fluctuations 112
7.3.2 Magnetic Field Gradient 113
7.3.3 ac-Zeeman Effects 114

7.3.4 ac Stark Shifts . . . 115
7.3.5 Higher Order Zeeman Effects . . . 115
7.3.6 Summary . . . 116
7.4 Calculation of Hyperfine Constants . . . 116
7.5 Conclusions . . . 117

Chapter 8: Conclusions and Future Directions . . . 119
8.1 Parity Nonconservation in Ba^+ . . . 119

Bibliography . . . 123

Appendix A: 650 nm Side-of-the-Fringe Locking Circuit . . . 131

LIST OF FIGURES

Figure Number Page

2.1 Energy levels and important transitions in $^{138}Ba^{+}$ 6
2.2 Addition of the A and B multipole hyperfine shifts to $5D_{3/2}$ in $^{137}Ba^{+}$ 16
2.3 Energy levels with HFS, and relevant transitions of $^{137}Ba^{+}$ 17
2.4 $5D_{5/2}$ $F = 3$ and $F = 4$ hyperfine Zeeman levels 20
2.5 Fixed square pulse duration lineshapes for coherent excitation 24
2.6 Transition amplitudes for E2 transitions 27
2.7 Optical pumping strategy for $^{138}Ba^{+}$ 29
2.8 Optical pumping strategy for $^{137}Ba^{+}$ 30

3.1 Cross-section of Paul trap with hyperbolic electrodes 33
3.2 Radial cross-section of linear Paul trap 34
3.3 Electric Potential produced by linear Paul Trap 35
3.4 Motion of the ion in the radial direction 36
3.5 Energy level diagram for Ba with relevant photoionization transitions 38
3.6 Micromotion compensation using correlation between scattered photon rate and rf phase 43
3.7 Photons collected by the PMT when the ion is cycling on the cooling transition and shelved 46

4.1 Schematic for 986/493 nm SHG system with bow tie cavity 48
4.2 Schematic for 986 nm laser stabilization to reference cavity 50
4.3 493 nm laser spectrum and absorption lines in $^{137}Ba^{+}$ 53
4.4 Schematic for 650 nm additional laser frequency generation and recombination 55
4.5 Absorption lines of the $5D_{3/2} \leftrightarrow 6P_{1/2}$ transition and 650 laser spectrum for $^{137}Ba^{+}$ 57
4.6 Tm,Ho:YLF laser stabilization schematic. 63
4.7 Loading rates of $^{138}Ba^{+}$ with Doppler effect 66
4.8 Frequency switching characteristics of HP 8656B synthesizer 69
4.9 Exploded view of the ion trap with spherical mirror 70
4.10 Top view of trap with laser access shown 72

4.11 Ion trap vacuum chamber with UHV pumping system 74
4.12 False-color images of a laser-cooled single $^{138}Ba^{+}$ and double on the EMCCD camera 76
4.13 Observed magnetic field fluctuations in the vertical direction in the laboratory 77
4.14 Exploded view of magnetic shield assembly 79
4.15 Semi-transparent view of shielding installed on ion trap. 79
4.16 Observed magnetic field fluctuations in laboratory after transit repair 80

5.1 Rabi oscillation using the 2051 nm laser with decoherence due to finite ion temperature 83
5.2 Normalized transfer efficiency from adiabatic passage as a function of sweep rate, α, for the 2051 nm laser 87

6.1 Energy levels and transitions employed for the Landé g factor measurement . 89
6.2 Results of rf spectroscopy of Zeeman transitions in $5D_{5/2}$ and $6S_{1/2}$ 92
6.3 Summary of measurements of the Landé g factor of $5D_{5/2}$ 93

7.1 $5D_{3/2}$ Hyperfine manifold energy level diagram with relevant transitions . . . 99
7.2 Typical resonance scans for the $\Delta m_F = 0$ transitions between hyperfine levels of $^{137}Ba^{+}$, $5D_{3/2}$ 103
7.3 Typical resonance scans for the $\Delta m_F = \pm 1$ transitions between hyperfine levels of the $5D_{3/2}$ level of $^{137}Ba^{+}$ 104
7.4 60- and 120-Hz ac magnetic field observed at the ion trap. 107
7.5 The $5D_{3/2}, F = 3 \leftrightarrow F = 2, \Delta m_F = 0$ hyperfine splitting extrapolated to zero-field. 109
7.6 The $5D_{32}, F = 2 \leftrightarrow F = 1, \Delta m_F = 0$ Hyperfine splitting extrapolated to zero-field. 110
7.7 The $5D_{32}, F = 1 \leftrightarrow F = 0, \Delta m_F = 0$ Hyperfine splitting extrapolated to zero-field. 111

A.1 Circuit diagram for the 650 nm laser side-of-the-fringe lock 132
A.2 Circuit diagram for the 650 nm laser frequency sweep 133

LIST OF TABLES

Table Number Page

2.1 Landé g_J factors for low-lying Ba^+states 7
2.2 Isotope shift data for $^{138}Ba^+$ to $^{137}Ba^+$ 10
2.3 Multipole Hyperfine Geometric Coefficients for $^{137}Ba^+$ 15
2.4 Hyperfine Coupling Constants for $^{137}Ba^+$ 18
2.5 Calculated linear and quadratic Zeeman dependence for $^{137}Ba^+$, $6S_{1/2}$ and $5D_{3/2}$ 21
2.6 Selection rules for E1, M1, and E2 transitions 25

4.1 650 nm laser frequency shifts and beam powers 58
4.2 Isotope and Hyperfine Shifts for the 791 nm laser transitions 67

6.1 A summary of systematic error estimates for our experimental apparatuses. 96

7.1 Measured hyperfine splittings of the $5D_{3/2}$ level of $^{137}Ba^+$in Hz, and measured quadratic Zeeman effects with comparison to theory 108
7.2 Measured Hyperfine Constants for the $5D_{3/2}$ level of $^{137}Ba^+$ 117
7.3 Summary of octupole measurements compared to theoretical predictions . . . 118

GLOSSARY

AC: Alternating current

AOM: Acousto-optic modulator / modulation

ARP: Adiabatic rapid passage

CW: Continuous wave

DAQ: Data acquisition

DC: Direct current

DPSS: Diode-pumped solid-state (laser)

DPAOM: Double pass(ed) acousto-optic modulator

E1, E2: Electric dipole and quadrupole moments, respectively

ECDL: External-cavity diode laser

EMCCD: Electron multiplying charge-coupled device

EOM: Electro-optic modulator

FM: Frequency modulation

FSR: Free spectral range

FWHM: Full-width at half maximum

HCL: Hollow cathode lamp

HF(I){S}: Hyperfine (interaction){structure}

HWP: Half-wave plate

IR: Infrared (radiation)

M1,M3: Magnetic dipole and octupole moments, respectively

MM(F): Multi-mode (fiber)

PBS: Polarizing beam splitter

PDH: Pound-Drever-Hall, a technique for frequency stabilizing a laser to a reference cavity, where the laser is phase modulated, and the back-reflected light is monitored to generate an error signal.

PM: Polarization maintaining (for optical fibers), or phase modulation

PMT: Photo-multiplier tube

PNC: Parity non-conservation

PPLN: Periodically poled lithium niobate, a nonlinear crystal used for frequency doubling

PZT: Lead-zirconate-titanate, a material used for the piezoelectric effect where mechanical stress causes charge to accumulate (and the reverse as well)

QED: Quantum electrodynamics

QWP: Quarter-wave plate

RF: Radio-frequency

SHG: Second harmonic generation

SM(F): Single mode (fiber)

SMA: SubMiniature A, a type of coaxial cable connector

SPDT: Single pole, double-throw, an electrical switch

TA: Tapered Amplifier

TEC: Thermo-electric cooler

TEM: Transverse electromagnetic, which refers to the mode of radiation propagating in a waveguide or free space

TTL: Transistor-transistor logic. Used frequently in our lab, +5 V is high, 0 V is low.

UHV: Ultra-high vacuum

ULE®: Ultra-low expansion, a proprietary glass made by Corning

UV: Ultraviolet (radiation)

VCO: Voltage-controlled oscillator

ACKNOWLEDGMENTS

First, and foremost thank you to my parents, Kirk and Linda Hoffman and my brother, Beau, for so very much love, encouragement and support as I made the choice to study physics in college, and pursue a PhD.

Many thanks to Professors Boris B. Blinov and E. Norval Fortson for teaching me the fundamentals of atomic physics, as well as the fine details of experimental technique. Boris has a mastery of chasing immediately to a potential solution to a problem, and such a vast storeroom of experimental knowledge, making it easy to overcome difficult problems. Norval posses what seems like limitless understanding of atomic physics, and the ability to bring you with him as he tackles how to perform a given experiment.

Thank you to Professors Steve Sharpe, and Subhadeep Gupta for providing excellent mentoring resources and advice through my career at the University of Washington. The department staff deserve much appreciation for the work that they contribute to the department, specifically Eric Lindahl and Jim Greenwell for much advice about constructing μ-metal shielding, and Ron Musgrave for teaching me the basics of machining.

Many thanks to fellow graduate students and friends, Adam Beardsley, Brian Burkholder, Andrew Laszlo, Max Hansen, and Grant Aivazian, for many great adventures within Seattle and beyond.

Additionally many thanks to the past and present researchers on the precision barium ion project: Anupriya Jayakumar, Adam Kleczewski, Spencer Williams, Eric Magnson, Eric Josberger, Yonatan Cohen, and Jeffery Sherman. Thank you to many contemporary colleagues in the Blinov research group for for so many great discussions and camaraderie, (especially over an after-work IPA): Thomas Noel and John Wright especially, Chen-Kuan Chou, Gang (Rick) Shu, Matthew Dietrich, Nathan Kurz, Carolyn Auchter, Richard Graham, Zichao Zhou, and Tomasz Sakrejda.

DEDICATION

To my beloved fiancée, Nani, who is undoubtedly the best thing that has ever happened to me, and who has made this journey so worthwhile.

Chapter 1

INTRODUCTION

Equipped with his five senses, man explores the universe around him and calls the adventure Science.

– Edwin Hubble

This adventure will be an exploration of how one probes the atomic structure at very fine levels, specifically, how does the structure of the nucleus influence the surrounding electrons. Along the way, we will also investigate how one answers such a question, and what tools are necessary for such an investigation. The whole experiment relies upon the nearly ideal conditions we can create in a laboratory - a single barium ion, suspended in vacuum, relatively unperturbed by collisions with other atoms. It is cooled to a temperature well below that of liquid helium or the cosmic microwave background, and an experimenter can exact control over its internal and external degrees of freedom by means of electromagnetic fields and radiation. This level of precision and control requires a complex apparatus with lasers, radio frequency sources, and photon counters, all working in concert so that we can glean basic information about our ion's fundamental makeup.

In this manuscript, we will cover many topics to explain this work from the motivation through to execution, as well as suggestions for the path ahead. This story will begin in Chapter 2, which will contain much of the theoretical framework for the atomic structure, which will ultimately span nearly 14 orders of magnitude in frequency space. In Chapter 3, we'll address some of the basics for how one goes about confining ions and performing the operations that are necessary to interrogate the atomic structure in a somewhat abstract sense. We will get into the real world in Chapter 4, and characterize the ion trapping apparatus, laser sources, and other supporting equipment. With many of these techniques in mind, Chapter 5 will walk through a pair of experiments that will tell us about how well we are doing at laser cooling our ion, and how that ion can be used as a sensor to measure

the linewidth of one of our narrow lasers.

Arriving in Chapter 6, we will begin to probe the atom's fundamental structure by performing a measurement that describes how the atom interacts with a magnetic field at the part per million level. All of this work leads to the end goal of this experiment – to understand how the nuclear structure influences the electronic energy levels. This experiment will be found in Chapter 7, but will rely heavily on all of the foundational work found in the preceding chapters. Chapter 8 will serve to offer a suggestion for the path ahead, namely towards a measurement of parity nonconservation in a single trapped ion, that could serve to answer questions about fundamental symmetries of the universe. These investigations will be left for another explorer to ponder, who must blaze the trail and live to tell the tale of their own adventure.

Chapter 2

ATOMIC THEORY

It is often said that the atomic theory of Ba^+ is as easy as the hydrogen atom, since one needs only really consider a single electron orbiting around what looks like a singly charged nucleus. However, in this statement alone, we have brushed a lot of non-trivial details under the rug. The goal of this chapter is to flesh out some of those details to figure out why $^{138}Ba^+$ and $^{137}Ba^+$ have the atomic structure they do, and what the goal of the measurement is. This discussion will be broken up into two major parts. The first part will be to describe the various interactions that lead to broken degeneracy of the energy levels of $^{138}Ba^+$ and $^{137}Ba^+$, namely the 'fine structure', the Zeeman effect, the hyperfine structure and the isotope shifts when one switches from $^{138}Ba^+$ to $^{137}Ba^+$. In the second part of this chapter, we will discuss the interaction of the ion with oscillatory fields, and how we drive transitions, including various selection rules and geometry considerations which are used for optical pumping and population of a single sublevel. Discussions of some directly applicable techniques, like ion trapping and laser-cooling, will be reserved for the Experimental Techniques section, in Chapter 3.

While this chapter will largely focus on Ba^+, much of the treatment applies to other atoms and ions. All of this discussion should be considered old news, and there are many sources that will offer a more generalized treatment than what will be presented here ([1], [2], [9], [13], [17], [67], [85]). This is intended to be a theoretical running start for someone wanting to bite into the experimental details of our project.

2.1 Atomic Structure of $^{138}Ba^{+}$

2.1.1 Ba^{+} Atomic Stucture

Throughout this work, we will be interrogating energy levels with splittings as large as 600 THz, and perturbations to these energy levels at the sub-Hz level[1]. These interactions span effectively 14 orders of magnitude, so it is necessary to investigate this broad range of frequencies.

The two ions we employ in our work are $^{138}Ba^{+}$ and $^{137}Ba^{+}$. They both possess 56 protons, 82 and 81 neutrons in the nucleus, respectively, with a single valence electron. Every interaction we discuss from here on out will perturb the electron's wavefunction in the states to a large or small degree. The largest effect comes simply from solving the radial part of the Schrödinger equation, which has the standard $1/n^2$ dependence, famous from the hydrogen atom, where n is the principal quantum number. Since many of the orbitals are filled by the other 54 electrons involved in the problem, the ground state of valence electron is $n = 6$. As the electron occupies higher n levels, its mean position is further away from the positively charged nucleus, resulting in less Coulomb attraction and higher energy levels.

When we include the angular wavefunctions, we find different shapes and orbital distributions of the electron's wavefunction, resulting in different binding energies of the electron. At this point, we will introduce the spectroscopic notation, nL, with L taking on letters {S,P,D,F,...}, for the orbital quantum number, $L = \{0, 1, 2, 3, ...\}$. This leads to the $6P$ levels being less bound than the $6S$ level, by the tune of approximately 600 THz. This also leads to the $5D$ levels being at an intermediate energy level (more bound than the $6P$, but less than $6S$), creating the "Λ" structure of the Ba^{+}, which has a number of benefits and complications.

Once we get beyond the simple Coulomb interaction in the Schrödinger equation, we next have to consider angular momentum in all of its forms. First, the electron has intrinsic spin, $S = \frac{1}{2}$, as well as orbital angular momentum, L. The vector addition of these angular

[1] We will frequently refer to energy differences in frequency units. Implicitly, we are describing E/h, where h is Planck's constant. A convenient conversion factor is 1 eV/h = 241.8 THz.

momenta, $\boldsymbol{J} = \boldsymbol{L} + \boldsymbol{S}$ will break the degeneracy of the $6P$ and $5D$ levels, through the spin-orbit interaction. This leads us to the full spectroscopic notations that will be employed heavily throughout the rest of this work, $n^{2S+1}L_J$, however, we will drop the redundant $2S+1$ term, because for any energy level of Ba^+, $S = 1/2$.

Because the electron is moving relativistically, if we boost to the frame of the electron, it will "see" a magnetic field $\boldsymbol{B}$. The electron itself possesses a magnetic moment $\boldsymbol{\mu}_S$, resulting in the Spin-Orbit Interaction $\boldsymbol{L} \cdot \boldsymbol{S}$. One can do a little bit of manipulation of the vector addition of angular momenta to find that:

$$\boldsymbol{L} \cdot \boldsymbol{S} = \frac{1}{2}\big(J(J+1) - L(L+1) - S(S+1)\big) \tag{2.1}$$

this interaction will break the degeneracy of the $6P$ and $5D$ levels. The difference between $6P_{1/2}$ and $6P_{3/2}$ being 50.7 THz, and $5D_{3/2}$ and $5D_{5/2}$ being 24.0 THz [30]. All of this information can be depicted in an energy level diagram as shown in Figure 2.1, along with the wavelength of radiation that addresses the pair of levels shown.

2.1.2 Zeeman Effect

With the basic structure of Ba^+ under our belt we can now start delving into some gritty, but very important atomic structure, namely the Zeeman Effect. In a few words, this is the interaction of the electron's magnetic moment with an externally applied, static magnetic field, which breaks the $2J+1$ degeneracy of the atomic states. Let's write the Hamiltonian for this interaction:

$$H_{\text{Zeeman}} = -\boldsymbol{\mu}_{\text{eff}} \cdot \boldsymbol{B} \tag{2.2}$$

where the electron's magnetic moment $\boldsymbol{\mu}_{\text{eff}}$ must align with the total angular momentum, $\boldsymbol{J}$, leading to:

$$\boldsymbol{\mu}_{\text{eff}} = -g_J \mu_B \boldsymbol{J}. \tag{2.3}$$

In this equation, $\mu_B = 5.788\ 381\ 8066(38) \times 10^{-5}$ eV/T is the Bohr magneton [48], and g_J is the Landé g-factor, which has the relation:

$$g_J(L,S,J) = \frac{J(J+1) + L(L+1) - S(S+1)}{2J(J+1)} + g_S \frac{J(J+1) - L(L+1) + S(S+1)}{2J(J+1)} \tag{2.4}$$

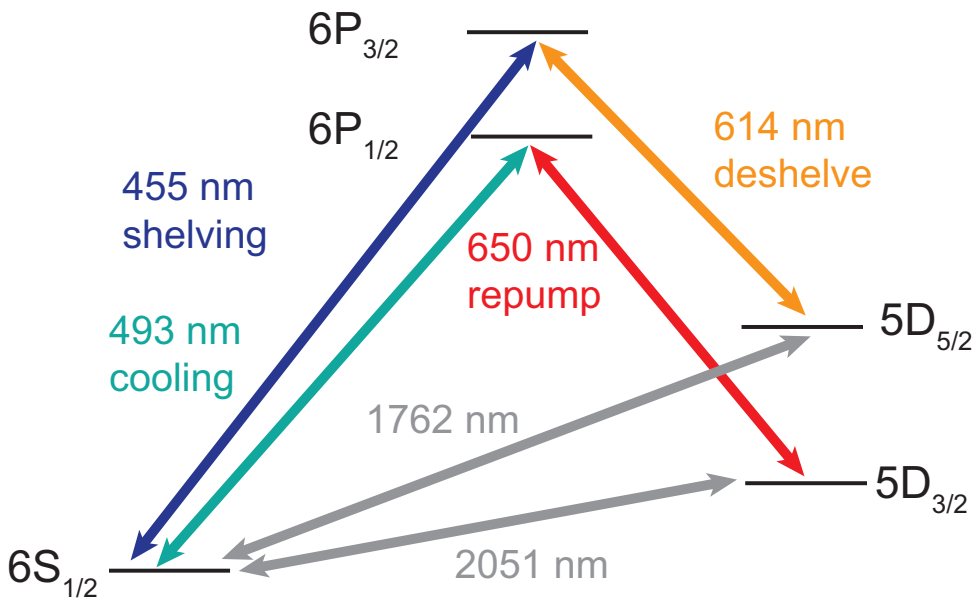

Figure 2.1: Energy levels and important transitions in $^{138}Ba^{+}$ (not to scale). The ion is laser cooled with the 493 nm transition, and is repumped from the long lived $5D_{3/2}$ state with 650 nm light. The ion can be 'shelved' using 455 nm light, via the $6P_{3/2}$ state, where it will remain in the metastable $5D_{5/2}$ state until a pulse of 614 nm light returns it to the cooling cycle. The electric quadrupole transitions at 2051 and 1762 nm are used to populate Zeeman sublevels of the $5D_{3/2}$ and $5D_{5/2}$ manifolds, respectively.

with $g_S = 2.002\ 319\ 304\ 3617(76)$ being the bound electron g-factor from [54]. The Landé-g factors for the low lying states of $^{138}Ba^+$ can be found in Table 2.1.

State	$g_J(L,S,J)$	Measured g_J	Reference
$6S_{1/2}$	2	2.002 490 6(11)	[35]
	2	2.002 491 92(3)	[46]
$6P_{1/2}$	2/3	0.672(6)	[57]
$6P_{3/2}$	4/3	1.328(8)	[57]
$5D_{3/2}$	5/4	0.799 327 8(3)	[36]
$5D_{5/2}$	6/5	$1.200\ 371(4)_{\text{stat}}(7)_{\text{sys}}$	[27]

Table 2.1: Landé g factors for low-lying Ba^+states with their first order calculations, as well as the highest precision experimental measurements. The work in Ref. [57] was performed with a fast beam of $^{138}Ba^+$, while that of Ref. [36] was performed in a Penning trap, and the work in Ref. [27] will be described in greater detail in this work in Chapter 6.

Since the magnetic field, $\boldsymbol{B}$, defines the ion's quantization axis, it is easy to find the shifts of the energy levels for $^{138}Ba^+$ using first order perturbation theory, where all other quantum numbers have been lumped into γ:

$$\begin{aligned}\Delta E_{\text{Zeeman}}(\gamma, J, m_J) &= \langle \gamma, J, m_J |\, g_J \mu_B \boldsymbol{J} \cdot \boldsymbol{B} \,| \gamma, J, m_J \rangle \\ &= \langle \gamma, J, m_J |\, g_J \mu_B J_z B \,| \gamma, J, m_J \rangle \\ &= g_J \mu_B B m_J. \end{aligned} \tag{2.5}$$

The shifts due to the Zeeman effect are linear in both magnetic field, and m_J, the projection of the total angular momentum onto the quantization axis, for all of the states in $^{138}Ba^+$ at the fields attainable in our laboratory $\boldsymbol{B} < 10$ G. We will address the second-order Zeeman effect later in Section 2.2.4, as it is highly relevant for $5D_{3/2}$ and $5D_{5/2}$ in $^{137}Ba^+$. However for $^{138}Ba^+$, the energy denominators are too large for the second-order Zeeman effect to really play a role, so first-order perturbation theory is sufficient.

For the proposed work in $^{137}Ba^+$, previous measurements of the Landé g_J factor for

$5D_{5/2}$ were not known to sufficient accuracy for the octupole experiment. For this reason, Tom Noel and I performed a measurement of this g factor in each of our ion traps, which is detailed in both Tom's PhD thesis [51], and in this manuscript in Chapter 6.

It is worth a quick moment to highlight that high-precision measurements of the electron g-factors are still of interest to theorists and experimentalists. Recently described in [22], these g-factor anomalies arise due to "relativistic corrections to the magnetic moment operator" which scales as $\sim -\alpha^2$, where $\alpha = 7.297\ 352\ 5698(24) \times 10^{-3}$ [48] is the fine structure constant, and "exchange core polarization and the spin orbit operator" which scales as $\sim Z^4\alpha^4$. Additionally, these measurements can shed light on higher-order QED corrections as described in Ref. [44]. A nice review of foundational work as well as theory can be found in Ref. [73].

2.2 Atomic Structure of $^{137}Ba^+$

In $^{138}Ba^+$, at low magnetic fields, the structure is relatively simple - each of the levels has $2J + 1$ Zeeman sublevels, and they have a nice, linear Zeeman effect. Experimentally, it is nice because $^{138}Ba^+$ is the most abundant isotope in naturally occurring barium, and the laser cooling described in Section 3.4 can be done with just two lasers. All of this simplicity exists because there is no nuclear spin in any of the even isotopes of Ba, but that changes when we go to the odd isotopes, namely, $^{137}Ba^+$ for this work, where $I = 3/2$.

2.2.1 Isotope Shifts

First we must account for the missing neutron, which slightly alters the wavefunctions of the energy levels, and thus affects the transition frequencies between the energy levels. There are two shifts we must concern ourselves with, namely the *mass shift* and the *volume shift*, which are described in general in [17]. Following this treatment, we will suppose that we have a transition between two energy levels of a hypothetical atom that has a nucleus with infinite mass, with frequency ν_∞. An atom with finite mass then has a transition frequency given by:

$$\nu = \nu_\infty \frac{M_N}{m_e + M_N} \tag{2.6}$$

where M_N is the mass of the nucleus and $m_e = 9.11 \times 10^{-31}$ is the electron mass. Since ν_∞ is impossible to measure, we can instead relate two different atomic masses M_N and M'_N, so that:

$$\begin{aligned} \Delta\nu^{\text{mass shift}} &= \nu_N - \nu_{N'} \\ &\simeq \frac{m_e}{m_p}\frac{N-N'}{NN'}\nu_\infty \end{aligned} \tag{2.7}$$

where $m_p = 1.67 \times 10^{-11}$ kg is the proton mass, having made the approximation that $M_N = Nm_p$. This effect is called the *normal mass shift*. Changing from $^{138}Ba^+$ to $^{137}Ba^+$, this mass effect has a relative difference of $\sim 3 \times 10^{-8}$, or shifts on the order of 10 MHz for all of the visible transitions utilized in this work. Foot [17] explains that there is a second effect of similar order to the *normal mass shift*, but it is much more difficult to calculate. The calculation of the so-called *specific mass shift* can be found in [85].

The second effect, the *volume shift*, occurs because of the electron's wavefunction overlaps with the nucleus. This effect is largest for s-shell wavefunctions because they have finite probability amplitude near the nuclear center[2]. An estimate of this shift, derived in [17] is given by:

$$\Delta\nu^{\text{volume shift}} = \frac{\langle r_N^2\rangle}{a_0^2}\frac{(N-N')}{N}\frac{Z^2}{(n^*)^3}R_\infty \tag{2.8}$$

where the nuclear size predicted by the nuclear drop model is $r_N \sim 1.2N^{1/3}$ fm, $a_0 = 0.529$ Å is the Bohr radius, Z is the atomic number, n^* is the quantum defect, and $R_\infty = 13.6$ eV is the Rydberg constant.

Knowing the order of magnitude of these shifts is important, however any attempt to do a calculation using these equations would be somewhat fruitless. Many effects can cause deviations from these shifts, (for instance, the fact that the nuclear shell model will predict different nuclear sizes depending on whether it has a closed or open shell), so it would be more useful to look to experiments to determine the isotope shifts on relevant transitions in Ba^+. A summary of these shifts can be found in Table 2.2, which are used when comparing frequencies for $^{137}Ba^+$ and $^{138}Ba^+$. The shifts for the 2051 nm and 1762 nm lasers can be

[2]Though it is certainly jumping the gun, this amplitude $|\psi(0)|^2$ leads to PNC effects for $6S_{1/2}$, because the electron can interact with the neutrons via the weak interaction.

calculated from this table as well. We will need to know the isotope shifts for one transition in neutral Ba, to tune the photoionization laser at 791 nm. This will be described further in Section 3.3

Table 2.2: Isotope shift data for $^{138}Ba^{+}$ to $^{137}Ba^{+}$. The experiments were performed with fast beams of Ba^{+}, and contain isotope shift data for other sets of naturally occurring isotopes within the references.

Transition	λ [nm]	$\delta^{137-138}$ [MHz]	Reference
$6S_{1/2} \leftrightarrow 6P_{1/2}$	493.5	271.1(1.7)	[79]
$6S_{1/2} \leftrightarrow 6P_{3/2}$	455.5	279.0(2.6)	[79]
$5D_{3/2} \leftrightarrow 6P_{1/2}$	649.9	13.0(0.4)	[78]
$5D_{5/2} \leftrightarrow 6P_{3/2}$	614.3	2.3(0.4)	[78]

2.2.2 Dipole Hyperfine Structure

It was alluded to earlier, but in $^{137}Ba^{+}$, the nucleus has nuclear spin $I = 3/2$, which leads to the hyperfine structure of the electron's energy levels. References like [17] usually only handle the nuclear magnetic dipole moment's ($\boldsymbol{\mu}_I$) contribution to the structure, but we will consider the next two moments as well: the nuclear electric quadruple moment ($\boldsymbol{Q}$), and the nuclear magnetic octupole moment ($\boldsymbol{\Omega}$), which is the pursuit of our experiment proposed in [3], and will be derived in Section 2.2.3.

First, though, we shall work through the derivation of the hyperfine structure from the nuclear magnetic dipole moment following [17] and [85], which is the only contribution for $6S_{1/2}$ and $6P_{1/2}$ because they only have $J = 1/2$. When the nucleus has spin, it also has a magnetic dipole moment, $\boldsymbol{\mu}_I$ which is proportional to the nuclear spin $\boldsymbol{I}$

$$\boldsymbol{\mu}_I = g_I \mu_N \boldsymbol{I}. \tag{2.9}$$

Here, $g_I = 0.623\ 786(3)$, is the neutron's g-factor [46], and $\mu_N = 3.152\ 451\ 2605(22) \times 10^{-8}$ eV/T is the nuclear magneton, which is related to the Bohr magneton by the electron

to proton mass ratio:

$$\mu_N = \mu_B \frac{m_e}{m_p}. \tag{2.10}$$

Loosely speaking, the electron's motion creates a magnetic flux density, $\boldsymbol{B}_e$ (not to be confused with the external magnetic field $\boldsymbol{B}$) that the nuclear magnetic dipole moment ($\boldsymbol{\mu}_I$) interacts with, leading to the Hamiltonian:

$$H_{\text{dipole HFS}} = -\boldsymbol{\mu}_I \cdot \boldsymbol{B}_e. \tag{2.11}$$

At this point, one could dig into finding the magnetic flux density, $\boldsymbol{B}_e$ like in Ref. [17], or we could simply lump the details into the dipole hyperfine constant A. Recognizing that $\boldsymbol{\mu}_I \propto \boldsymbol{I}$ and that $\boldsymbol{B}_e \propto \boldsymbol{J}$, we rewrite our Hamiltonian as:

$$H_{\text{dipole HFS}} = A\boldsymbol{I} \cdot \boldsymbol{J}, \tag{2.12}$$

effectively brushing the details under the metaphorical rug of A. Should one want to really get at this calculation, one could refer to Refs. [45] and [63], where the hyperfine constants for $^{137}Ba^+$ are calculated explicitly. Experimental measurements and theoretical calculations are summarized in Table 2.4.

Since this effect will be relatively tiny compared to the fine-structure, it's safe to look at the total angular momentum of the ion as $\boldsymbol{F} = \boldsymbol{I} + \boldsymbol{J}$, which remains constant for a given state. If one looks at the vector addition of $\boldsymbol{I}$ and $\boldsymbol{J}$, they will find that $\boldsymbol{I} \cdot \boldsymbol{B}$ and $\boldsymbol{J} \cdot \boldsymbol{B}$ are not constant as $\boldsymbol{I}$ and $\boldsymbol{J}$ both precess around $\boldsymbol{F}$ like in [65]. Ultimately this means that at low magnetic field, m_I and m_J are not good quantum numbers anymore[3]. Instead the eigenstates are in the F, m_F basis, so we can write our states as $|\gamma, I, J, F, m_F\rangle$

We now quickly work though an identity useful for the addition of angular momenta to find the $\boldsymbol{I} \cdot \boldsymbol{J}$ operator

$$\begin{aligned} \boldsymbol{F}^2 &= (\boldsymbol{I} + \boldsymbol{J})^2 \\ &= \boldsymbol{I}^2 + \boldsymbol{J}^2 + 2\boldsymbol{I} \cdot \boldsymbol{J}. \end{aligned} \tag{2.13}$$

[3]As we will see in Section 2.2.4, this will be somewhat quickly violated in $5D_{5/2}$, because the hyperfine interaction and the Zeeman effect are at a similar scale, so our states become mixed, and there really aren't any good quantum numbers anymore.

Quickly rearranging we find that

$$\boldsymbol{I}\cdot\boldsymbol{J} = \frac{\boldsymbol{F}^2 - \boldsymbol{I}^2 - \boldsymbol{J}^2}{2} \tag{2.14}$$

and it is easy to remember how these operators work [65], namely that

$$\boldsymbol{F}^2\,|\gamma, I, J, F, m_F\rangle = |\gamma, I, J, F, m_F\rangle\, F(F+1) \tag{2.15}$$

$$F_z\,|\gamma, I, J, F, m_F\rangle = |\gamma, I, J, F, m_F\rangle\, m_F \tag{2.16}$$

with $\boldsymbol{J}$ and $\boldsymbol{I}$ behaving in similar ways. This identity was used for $\boldsymbol{L}$ and $\boldsymbol{S}$ in Eq. 2.1.

Finally, we can write the energy shift due to the dipole hyperfine interaction:

$$\begin{aligned}\Delta E_{\text{dipole HFS}} &= A\langle \boldsymbol{I}\cdot\boldsymbol{J}\rangle \\ &= A\,\frac{F(F+1) - J(J+1) - I(I+1)}{2}.\end{aligned} \tag{2.17}$$

Now that we have found the basis for our new eigenstates, we should quickly look at what the degeneracy of our states will be, and what values of F we will find for our various states. Much like the addition of spin, $\boldsymbol{S}$ and orbital angular momentum $\boldsymbol{L}$, the values of F are:

$$F \in \{|I-J|, |I-J|+1, ..., I+J\}, \tag{2.18}$$

with degeneracy 2(F+1) and each sublevel defined by the projection of the total angular momentum operator, m_F such that

$$m_F \in \{-F, -F+1, ..., F\}, \tag{2.19}$$

The degeneracy will be broken by the introduction of a magnetic field, described in Section 2.2.4.

Finally, we will end with a reminder of the interval rule between adjacent hyperfine states:

$$\Delta E_{\text{dipole HFS}}(F) - \Delta E_{\text{dipole HFS}}(F-1) = AF. \tag{2.20}$$

The interval rule is a nice rule of thumb for the hyperfine splittings for low angular momentum states, because A is usually larger than B, the quadrupole hyperfine constant which is introduced in Section 2.2.3. We will soon see, however, that for $5D_{3/2}$ and $5D_{5/2}$, that B is on the order or larger than A, making for a more complicated structure.

2.2.3 Multipole Hyperfine Structure

For many systems, considering the dipole moment is all that is necessary, especially for ground state hyperfine splittings (like the ones used in microwave frequency standards, like NIST-F2, which defines the second using two ground-state Cs hyperfine levels [29]), so, one need only employ the $\boldsymbol{I} \cdot \boldsymbol{J}$ operator. However, generally, a nucleus with spin I has $2I + 1$ multipole moments, and the 2^k moment contributes to the hyperfine structure to first order if $J \geq k/2$, where k is the rank of the operator [4]. Then, using parity symmetry considerations, we can determine which moments are allowed: electric monopole (E0), magnetic dipole (M1), electric quadrupole (E2), magnetic octupole (M3), electric hexadecapole (E4), etc., depending on the nuclear spin[4]. The alternation between electric and magnetic moments should be familiar from Jackson's treatment of multipolar radiation [28]. Trivially, all atomic nuclei possess an electric monopole moment (E0), which is just the charge, so we will ignore this moment from here on. Since $^{138}Ba^+$ has $I = 0$, it has no multipole moments, and thus no hyperfine structure. In $^{137}Ba^+$ and $^{135}Ba^+$ though, $I = 3/2$, so the $6S_{1/2}$ and $6P_{1/2}$ levels have only M1 contributing, $6P_{3/2}$ can have M1, E2, and M3, but is too short lived ($\tau = 6.3(0.1)$ ns [56]) for a measurement of M3 to be possible. In the long-lived $5D_{3/2}$ and $5D_{5/2}$, where M1, E2, and M3 contribute to the hyperfine structure, it is possible to measure each of these multipole moments' contributions to the atomic structure [3]. This is the ultimate goal of this experiment, and will be explored in more detail in Chapter 7.

For now, we will ignore the experiment, and work through these moments' contributions to the structure of $^{137}Ba^+$ theoretically. Following the treatment of [2], we can look at the further moments dependence on I, and J as:

$$\Delta E_{\mathrm{HFS}} = A\boldsymbol{I} \cdot \boldsymbol{J} + Bf_{\mathrm{E2}}(\boldsymbol{I}, \boldsymbol{J}) + Cf_{\mathrm{M3}}(\boldsymbol{I}, \boldsymbol{J}) \tag{2.21}$$

[4]M1, E2, and M3 are also referred to as $\boldsymbol{\mu}$, $\boldsymbol{Q}$ and $\boldsymbol{\Omega}$ in the literature respectively [4], [28].

with

$$
\begin{aligned}
f_{\mathrm{E2}}(\boldsymbol{I},\boldsymbol{J}) &= \frac{3(\boldsymbol{I}\cdot\boldsymbol{J})^2+\frac{3}{2}(\boldsymbol{I}\cdot\boldsymbol{J})-I(I+1)J(J+1)}{2I(2I-1)J(2J-1)} && (2.22)\\
f_{\mathrm{M3}}(\boldsymbol{I},\boldsymbol{J}) &= \Big\{10(\boldsymbol{I}\cdot\boldsymbol{J})^3+20(\boldsymbol{I}\cdot\boldsymbol{J})^2 \\
&+ 2(\boldsymbol{I}\cdot\boldsymbol{J})\big[-3I(I+1)J(J+1)+I(I+1)+J(J+1)+3\big] && (2.23)\\
&- 5I(I+1)J(J+1)\Big\}/\big[I(I-1)(2I-1)J(J-1)(2J-1)\big].
\end{aligned}
$$

Or we can package this information all more neatly using Wigner $3j$ and $6j$ Symbols as in [4], by using a geometric weighting factor for rank k, $X_k(IJF)$ defined by:

$$
X_k(I,J,F) = (-1)^{I+J+F}\frac{\begin{Bmatrix} F & J & I \\ k & I & J \end{Bmatrix}}{\begin{pmatrix} J & k & J \\ -J & 0 & J \end{pmatrix}\begin{pmatrix} I & k & I \\ -I & 0 & I \end{pmatrix}} \qquad (2.24)
$$

so the hyperfine structure for a state $|\gamma,I,J,F\rangle$ is:

$$
\Delta E_{\mathrm{HFS}} = AIJX_1(I,J,F)+4BX_2(I,J,F)+CX_3(I,J,F). \qquad (2.25)
$$

Either method gives the same result, which have been calculated for the reader's convenience for all of the relevant states of $^{137}\mathrm{Ba}^+$ in Table 2.3.

To complete the hyperfine structure, we need the hyperfine coupling constants, A, B, and C, which can be calculated theoretically or measured in the laboratory. For convenience to the spectroscopist, the values of these constants are often reported in frequency units, and some can be found in Table 2.4.

At this point, we have much of the theoretical tools necessary to look at the basic structure of $^{137}\mathrm{Ba}^+$. It is instructive to see how the addition of the multipole hyperfine structure perturbs the energy levels of $5D_{3/2}$, as shown in Figure 2.2, where first the dipole HFI is included, and then the quadrupole HFI. An energy level diagram for all of the low-lying energy levels with relevant transitions can be found in Figure 2.3. This information is necessary for laser cooling $^{137}\mathrm{Ba}^+$, which requires additional frequencies of 493 nm light and 650 nm light to address all sublevels of the $6S_{1/2}$ and $5D_{3/2}$ manifolds. Namely, the 493 nm

light must have two frequency components separated by approximately 8 GHz, and the 650 nm light must have at least four frequency components, to repump the four hyperfine levels.

The hyperfine constants A, B, and C can be related to their moments $\boldsymbol{\mu}$, $\boldsymbol{Q}$, and $\boldsymbol{\Omega}$, respectively with detailed knowledge of the $^{137}Ba^{+}$wavefunctions, which we will rely on theorists for. For all intents and purposes, the goal of the precision hyperfine structure measurement will be to extract A, B, and C.

2.2.4 $^{137}Ba^{+}$ Hyperfine Structure with Zeeman Effect

To break the $2F+1$ degeneracy of a given state of $^{137}Ba^{+}$, an external magnetic field can be applied. The addition of nuclear spin, I, changes the g_F-factor of a given m_F level by the following relation, which now includes the electronic g_J-factor and the nuclear g_I-factor:

$$g_F = g_J \frac{F(F+1)+J(J+1)-I(I+1)}{2F(F+1)} - g_I \frac{\mu_N}{\mu_B} \frac{F(F+1)-J(J+1)+I(I+1)}{2F(F+1)}. \quad (2.26)$$

Table 2.3: Multipole Hyperfine Geometric Coefficients for $^{137}Ba^{+}$. One can think of these as weighting factors for the hyperfine constants A, B, and C found in Table 2.4.

State		$\boldsymbol{I}\cdot\boldsymbol{J}$	f_{E2}	f_{M3}
$6S_{1/2}$ and $6P_{1/2}$	F=1	-5/4	—	—
	F=2	3/4	—	—
$5D_{3/2}$ and $6P_{3/2}$	F=0	-15/4	5/4	-35
	F=1	-11/4	1/4	21
	F=2	-3/4	-3/4	-7
	F=3	9/4	1/4	1
$5D_{5/2}$	F=1	-21/4	7/10	-42/5
	F=2	-13/4	-1/10	54/5
	F=3	-1/4	-11/20	-27/5
	F=4	15/4	1/4	1

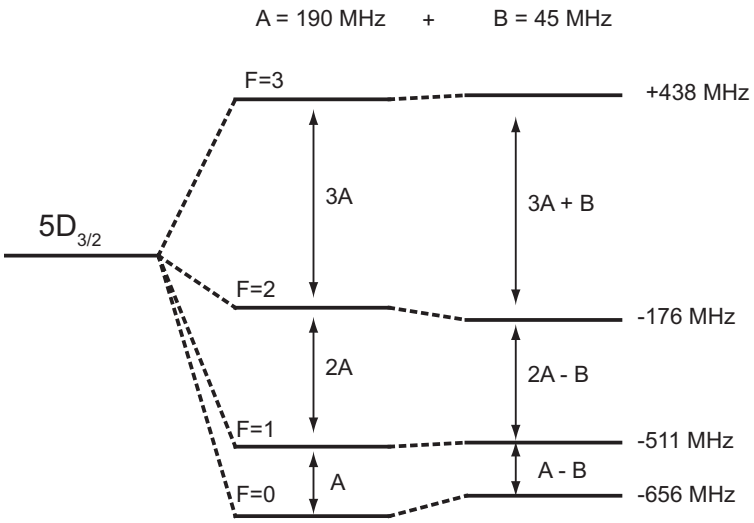

Figure 2.2: Addition of the A and B multipole hyperfine shifts to $5D_{3/2}$ in $^{137}Ba^{+}$. Note the interval rule shown with the inclusion of the magnetic dipole A, and its violation with the inclusion of B. The final shifts from the unperturbed level are shown to the right, not including the isotope shift. Inclusion of the octupole moment's contribution, C, would not be resolvable on this scale, and is not shown.

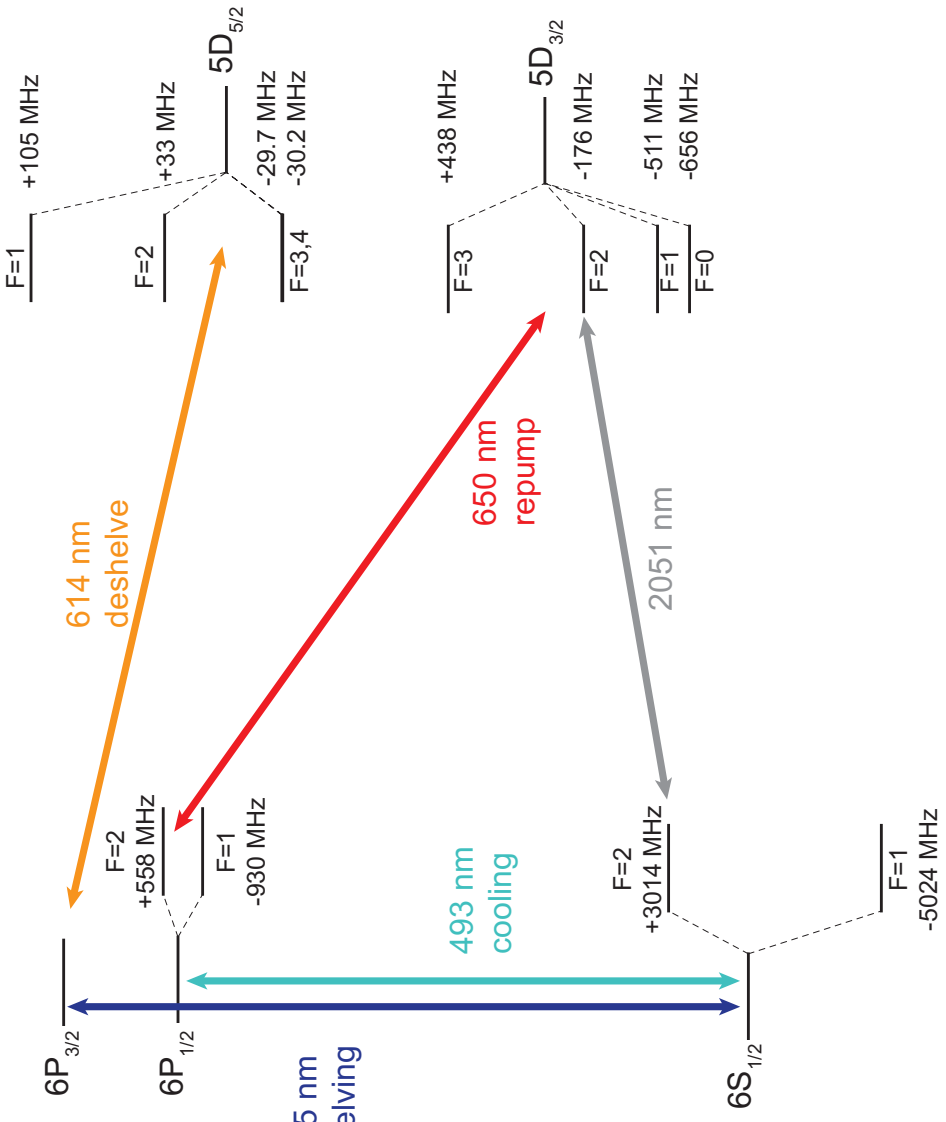

Figure 2.3: Energy levels with HFS, and relevant transitions of $^{137}Ba^{+}$. Each hyperfine manifold's HFS splittings are to scale, but difference between different energy levels is not.

Table 2.4: Experimentally measured hyperfine coupling constants for $^{137}Ba^{+}$. More historical measurements for $6P_{1/2,3/2}$ can be found in [78]. Citations lacking uncertainty should be taken as theoretical calculations. This list should not be considered to be exhaustive, but merely a representation of some of the values found in the literature.

State	A [MHz]	B [MHz]	C [Hz]	Reference
$6S_{1/2}$	4018.870 833 85(18)	—	—	[74]
	4020.3(2.3)	—	—	[79]
	4072.83	—	—	[63]
	3997.39	—	—	[61]
$6P_{1/2}$	741.1(1.6)	—	—	[79]
	743.7(0.3)	—	—	[78]
	736.98	—	—	[63]
	733.98	—	—	[61]
$6P_{3/2}$	126.7(1.1)	95.0(3.7)	—	[79]
	127.2(0.2)	92.5(0.2)	—	[78]
	130.94	—	—	[63]
	121.35	—	—	[61]
$5D_{3/2}$	189.730 531 1(15)	44.538 767 9(7.3)	33.74(36)	This work
	189.730 524 90(31)	44.538 793 6(10)	32.465(42)	[43][5]
	189.7288(6)	44.5417(16)	Not Observed	[76]
	188.76	—	—	[63]
	191.53	—	—	[61]
	190.89	46.82	—	[64]
$5D_{5/2}$	-12.029 234(11)	59.525 520(110)	-12.41(77)	[42]
	-12.028(11)	59.533(43)	Not Observed	[69]
	-9.99	—	—	[61]
	-11.99	62.27	—	[64]

When $I = J$ as in $5D_{3/2}$ of $^{137}Ba^+$, there is a nice simplification for the g_F factor, that does not depend on F:

$$g_F = \frac{1}{2}\left(g_J - \frac{\mu_N}{\mu_B} g_I\right). \tag{2.27}$$

In $^{137}Ba^+$, the most accurate measurement of g_I to date is 0.623 786(3) [46], and $\mu_N/\mu_B = (1836.152\ 672\ 45(75))^{-1}$ [48]. To first order, the Zeeman effect is given by:

$$\Delta E_{\text{Zeeman}}(\gamma, F, m_F) = g_F \mu_B B m_F. \tag{2.28}$$

In $^{137}Ba^+$, there are now $m_F = 0$ sublevels of each state where there is no linear Zeeman effect. However, there will be a quadratic Zeeman effect that is new to the system with the introduction of hyperfine structure. Employing second-order perturbation theory as in [65] (neglecting the contribution from the nuclear g_I-factor, as it is a factor 10^{-3} from g_J), the Hamiltonian is as follows:

$$\Delta E_{\text{Quad.Zeeman}}(\gamma, F, m_F) = \sum_{F', m'_F} \frac{|\langle \gamma F m_F | J_z | \gamma' F' m'_F \rangle|^2 g_J^2 \mu_B^2 B^2}{E_{F,m_F} - E_{F',m'_F}}. \tag{2.29}$$

At low magnetic fields (approximately < 2 G), this is good approximation for $6S_{1/2}$ and $5D_{3/2}$, but it all goes out the window for $5D_{5/2}$, especially for $F = 3$ and $F = 4$, as the difference in energy between these two states is on the order of 500 kHz. In this hyperfine manifold at magnetic fields > 0.5 G, the $|F, m_F\rangle$ basis is no longer a good basis for states, nor is the $|m_I, m_J\rangle$ basis commonly used at very high fields [17]. In this intermediate regime, we will need to diagonalize the Zeeman Hamiltonian to understand the magnetic field dependence of these sublevels.

To do this, we will need to rewrite the Hamiltonian and use the raising and lowering operators in the $|m_I, m_J\rangle$ basis. Recall that [65]:

$$J_+ |J, mJ\rangle = \sqrt{(J - m_J)(J + m_J + 1)}\, |J, mJ + 1\rangle \tag{2.30}$$

$$J_- |J, mJ\rangle = \sqrt{(J + m_J)(J - m_J + 1)}\, |J, mJ - 1\rangle \tag{2.31}$$

and similarly for I_+ and I_-. The $\boldsymbol{I} \cdot \boldsymbol{J}$ operator is then:

$$\boldsymbol{I} \cdot \boldsymbol{J} = \frac{1}{2}(I_+ J_- + I_- J_+) + I_z J_z \tag{2.32}$$

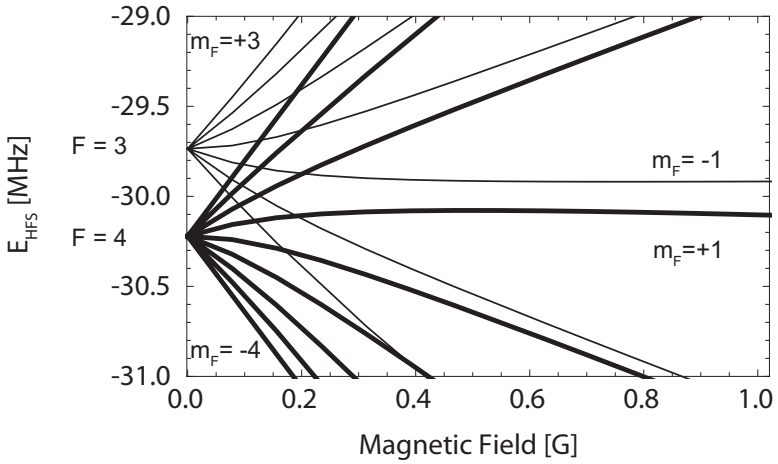

Figure 2.4: $5D_{5/2}$ $F = 3$ (fine lines)and $F = 4$ (thick lines) hyperfine Zeeman levels. This plot shows the mixing of these hyperfine levels at even low laboratory $\boldsymbol{B}$ fields. Note that at approximately 1 G, $|F = 3, m_F = -1\rangle$ and $|F = 4, m_F = +1\rangle$ are nearly $\boldsymbol{B}$-field independent.

which we can insert into Eqns. 2.21, 2.22, and 2.23. We then just use the Zeeman effect Hamiltonian, separating out the effects of the electron and nuclear spin (or equivalently, not assuming that F and m_F are good quantum numbers like we did in Equation 2.28):

$$H_{\text{Zeeman}} = g_J \mu_B B m_J + g_I \mu_N B m_I. \tag{2.33}$$

Combining all of this, we can then write matrices in the $|m_I, m_J\rangle$ basis, and numerically diagonalize the Hamiltonian to see the sublevels' magnetic field dependence for a given hyperfine manifold.

For $5D_{5/2}$, we can zoom in to the nearly degenerate $F = 3$ and $F = 4$ levels to see the nonlinear magnetic field dependence showing up at fields < 1 G as in Figure 2.4. The effect is much larger at fields that are more convenient in the lab, namely between 3 G and 5 G. Additionally, this effect appears in $5D_{3/2}$, but to a smaller degree at fields less than 3 G where, the quadratic Zeeman effect is dominant, but there are small (tens of Hz shifts) of the $\Delta m_F = 0$ splittings due to higher-order Zeeman effect.

To end this treatment of the Zeeman effect, the first- and second-order Zeeman effects

for the low-lying states of $^{137}Ba^{+}$ have been calculated in Table 2.5 for a quick reference.

Table 2.5: Calculated linear and quadratic Zeeman dependence for $6S_{1/2}$ and $5D_{3/2}$ levels in $^{137}Ba^{+}$. $5D_{5/2}$ is not included because of its complicated structure, as is evident at only 1 G in Figure 2.4 and earlier discussion.

State		$m_F \neq 0$ [kHz/G]	$m_F = 0$ [kHz/G^2]
$6S_{1/2}$	F=1	-700.7 m_F	-0.244
	F=2	+700.7 m_F	+0.244
$5D_{3/2}$	F=0	—	-10.766
	F=1	+559.6 m_F	+7.778
	F=2	+559.6 m_F	+2.070
	F=3	+559.6 m_F	+0.917

2.3 Interaction with Radiation

Now that we have the atomic structure of $^{138}Ba^{+}$ and $^{137}Ba^{+}$ firmly in our grasp, it is necessary to describe the rules by which transitions are driven. We will need this information to describe how various sublevels are populated by the lasers in the laboratory. This is a very thoroughly described subject ([1], [9], [13], [67]), so we will just give a quick summary of the results, and rules that apply to our system.

2.3.1 Coherent Excitation by Monochromatic Radiation

Let us assume that we have the simplest case possible, a two-level system with levels $|1\rangle$ and $|2\rangle$ that have energies E_1 and E_2 respectively ($E_2 > E_1$), where both of the levels have very long lifetimes. In our work, these could be two sublevels of a Zeeman (or hyperfine) manifold of $6S_{1/2}$, $5D_{3/2}$, or $5D_{5/2}$, or one sublevel of $6S$ and one sublevel of $5D$. We do not necessarily have to say which at the moment.

We begin by using the time-dependent Schrödinger equation:

$$i\hbar\frac{\partial\Psi}{\partial t} = H\Psi \tag{2.34}$$

where H now has a time-dependent and time-independent part:

$$H = H_0 + H_I(t). \tag{2.35}$$

H_0 should be considered to be everything we covered through to this point regarding the atomic structure, and $H_I(t)$ is some interaction Hamiltonian which describes the atom's interaction with an oscillating electric or magnetic field that will act as a perturbation. Then we will write the wavefunction for the n-th energy level, E_n:

$$\Psi_n(\boldsymbol{r}, t) = \psi_n(\boldsymbol{r}) e^{-iE_n t/\hbar}. \tag{2.36}$$

It should be noted that the states here are only eigenstates of the stationary Hamiltonian H_0. We will just jump right in and use Dirac ket notation so that $\psi_n(\boldsymbol{r}) = |n\rangle$, and make the substitution $\omega_n = E_n/\hbar$. At any instant of time we can write the full wavefunction as:

$$\Psi(\boldsymbol{r}, t) = c_1(t)\,|1\rangle\, e^{-i\omega_1 t} + c_2(t)\,|2\rangle\, e^{-i\omega_2 t}, \tag{2.37}$$

where

$$|c_1(t)|^2 + |c_2(t)|^2 = 1 \tag{2.38}$$

to satisfy normalization conditions. $c_1(t)$ and $c_2(t)$, when multiplied by their complex conjugate can be thought of as the populations in states $|1\rangle$ and $|2\rangle$ respectively. Typically the treatment specializes at this point to an oscillating electric field interacting the atom, but let's continue in a general sense, and break up our interaction Hamiltonian into

$$H_I(t) = H_I \cos(\omega t), \tag{2.39}$$

where H_I is time-independent and describes the nature of the interaction, and ω is the oscillation frequency of the radiation. Plugging this into the Schrödinger equation, we get:

$$i\dot{c_1}(t) = \Omega \cos(\omega t) e^{-i\omega_0 t} c_2(t) \tag{2.40}$$

$$i\dot{c_2}(t) = \Omega^* \cos(\omega t) e^{+i\omega_0 t} c_1(t) \tag{2.41}$$

where $\omega_0 = (E_2 - E_1)/\hbar$ and Ω is the Rabi frequency:

$$\Omega = \frac{\langle 1|\, H_I\, |2\rangle}{\hbar}. \tag{2.42}$$

For one quick example, the E1 transition, our interaction Hamiltonian is the electric dipole $e\boldsymbol{r}$ interacting with an oscillating electric field $\boldsymbol{E} = \boldsymbol{E_0}\cos(\omega t)$, so the Rabi frequency is given by:

$$\Omega_{E1} = \frac{\langle 1|\, e\boldsymbol{r}\cdot\boldsymbol{E_0}\,|2\rangle}{\hbar}, \tag{2.43}$$

where the matrix element can be found depending on the polarization of the laser. Implicitly, we have already made the electric dipole approximation, assuming that the wavelength of the radiation is larger than the spatial extent of the atom's wavefunction.

Now, we will imagine that the population starts entirely in the lower level, so that $c_1(0) = 1$ and $c_2(0) = 0$. And we can rewrite the differential equations Eq. 2.40 and Eq. 2.41 in exponential form, and apply the rotating wave approximation, namely that a term that contains $e^{i(\omega+\omega_0)}$ rotates rapidly and is neglected:

$$i\dot{c_1}(t) = \frac{\Omega}{2}e^{i(\omega-\omega_0)t}c_2(t) \tag{2.44}$$

$$i\dot{c_2}(t) = \frac{\Omega^*}{2}e^{-i(\omega-\omega_0)t}c_1(t). \tag{2.45}$$

We can combine these into a second-order differential equation and apply the initial conditions to arrive at the result

$$|c_2(t)|^2 = \frac{\Omega^2}{W^2}\sin^2\left(\frac{Wt}{2}\right), \tag{2.46}$$

where $W^2 = \Omega^2 + (\omega-\omega_0)^2$ is called the generalized Rabi frequency. Often another substitution $\delta = (\omega-\omega_0)$ is made for the detuning of the radiation frequency ω from the resonant frequency ω_0. The form of the function shows that the population will coherently oscillate between $|1\rangle$ and $|2\rangle$ on resonance. This process is called Rabi oscillation or Rabi flopping. Sending an on-resonant ($\delta = 0$) pulse of radiation with pulse duration $t = \pi/\Omega$ is called a π pulse, which maximally transfers population from $|1\rangle$ to $|2\rangle$.

If we use pulses that are longer or shorter than a π pulse, we observe quite different line shapes as shown Figure 2.5. Though we will need to account for various experimental processes with some additional parameters, Eq. 2.46 is the function that we will fit most of our rf-spectroscopy to, with Ω and ω_0 as free parameters. Knowledge of the general form of these lineshapes can inform when a transition is being over- or under-driven.

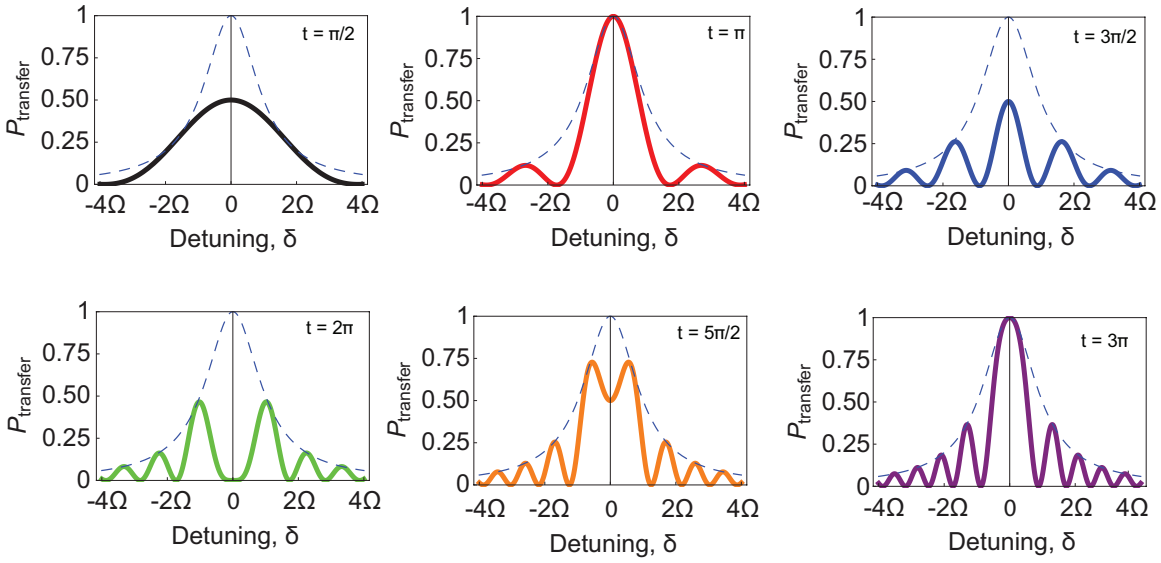

Figure 2.5: Fixed square pulse duration lineshapes for coherent excitation. The probability of transferring population from $|1\rangle$ to $|2\rangle$ as a function of the detuning from the resonance frequency. The solid curves show what spectrum would be observed as the pulse duration increases. The dashed line in each plot is a Lorentzian with width Ω, that represents the envelope of the spectrum as $t \to \infty$.

2.3.2 Adiabatic Rapid Passage

Another technique that is employed often in our laboratory is called Adiabatic Rapid Passage (ARP) which can be shown using the "Bloch Sphere" treatment of coherent radiation as in [17]. This would be where one sweeps the frequency of a source of radiation over a resonance. On first glance, the name is somewhat confusing and contradictory, but makes more sense because one is effectively comparing two different rates in the problem. "Adiabatic", meaning slow compared to the the Rabi frequency; and "rapid", compared to a source of decoherence in the problem which could be spontaneous decay from an excited state with lifetime τ. For an example here, we consider ARP from the ground state $6S_{1/2}$ to the metastable state, $5D_{3/2}$, with an excited lifetime of approximately 80 s [86]. Typical

Rabi frequencies observed for this transition in the lab for the 2051 nm laser used to excite this transition are on the order of $2\pi \times 10$ kHz. We use this technique to achieve good population transfer between two states that is robust against experimental drifts. We will return to this in Section 5.2, including a source of decoherence.

2.3.3 E1, E2, and M1 Transition Selection Rules

To perform experiments in Ba^+, one needs to know the selection rules for the first few orders of transitions. This dictates how lasers must be aligned relative to the quantization axis set by the external magnetic field, $\boldsymbol{B}$, as well as what the polarization of the beam must be. To this end, we use the Wigner-Eckhart theorem, as is discussed in many quantum mechanics texts (e.g. [17], [23], [65]), to derive the selection rules that are summarized in Table 2.6.

Table 2.6: Selection rules for E1, M1, and E2 transitions. The rigorous selection rules are set regardless of whether L and S are good quantum numbers (which is almost always the case for us). The rule regarding Δl refers to the configuration $n_1 l_1 n_2 l_2 n_3 l_3 ... n_x l_x$ and only one electron changes its value of l for E1 and E2 transitions, while no electron may change l or n for M1 transitions. For atoms with nuclear spin ($^{137}Ba^+$ and $^{135}Ba^+$) selection rules for F and m_F follow those of J and m_J. Additional rules for the intermediate coupling regime are not shown.

State	E1	M1	E2
Rigorous	$\Delta J = 0, \pm 1$	$\Delta J = 0, \pm 1$	$\Delta J = 0, \pm 1, \pm 2$
	$(J = 0 \nleftrightarrow 0)$	$(J = 0 \nleftrightarrow 0)$	$(J = 0 \nleftrightarrow 0, 0 \nleftrightarrow 1, \frac{1}{2} \nleftrightarrow \frac{1}{2})$
	$\Delta m_J = 0, \pm 1$	$\Delta m_J = 0, \pm 1$	$\Delta m_J = 0, \pm 1, \pm 2$
	Parity change	No parity change	No parity change
LS Coupling	$\Delta l = \pm 1$	$\Delta l = 0$, $\Delta n = 0$	$\Delta l = 0, \pm 2$
	$\Delta S = 0$	$\Delta S = 0$	$\Delta S = 0$
	$\Delta L = 0, \pm 1$	$\Delta L = 0$	$\Delta L = 0, \pm 1, \pm 2$
	$(L = 0 \nleftrightarrow 0)$		$(L = 0 \nleftrightarrow 0, 0 \nleftrightarrow 1)$

These are good rules to follow in general, but there are additional rules for electric quadrupole (E2) transitions which arise from a linearly-polarized laser's alignment with the quantization axis $\boldsymbol{B}$ and its polarization's orientation as well.[6] To address this, we will closely follow the treatment of [66], which followed [60]. We start by defining the orientation of the magnetic field, $\boldsymbol{B}$, the laser wave-vector, $\boldsymbol{k}$, and the electric field polarization, $\boldsymbol{\epsilon}$ in cartesian coordinates:

$$\boldsymbol{B} = B(0,0,1), \tag{2.47}$$

$$\boldsymbol{k} = k(\sin\phi, 0, \cos\phi), \tag{2.48}$$

$$\boldsymbol{\epsilon} = (\cos\gamma\cos\phi, \sin\gamma, -\cos\gamma\sin\phi)\,, \tag{2.49}$$

where the laser polarization projection onto the quantization axis is at an angle γ, and $\boldsymbol{k}$ is at an angle ϕ with respect to $\boldsymbol{B}$. If we write the electric field of a plane wave as $\boldsymbol{E}e^{i(\boldsymbol{k}\cdot\boldsymbol{r}-\omega t)}$, we can expand the exponential to see the multipole terms:

$$\boldsymbol{E}e^{i(\boldsymbol{k}\cdot\boldsymbol{r}-\omega t)} = Ee^{-i\omega t}\boldsymbol{\epsilon}\,(1 + i(\boldsymbol{k}\cdot\boldsymbol{r}) + ...)\,. \tag{2.50}$$

Taking the first term of the series, we then write the Rabi frequency of the electric dipole transition

$$\Omega_{\mathrm{E1}} = \frac{eE}{\hbar}\left|\left\langle\gamma, J, m_J\right|\boldsymbol{\epsilon}\cdot\boldsymbol{r}\left|\gamma', J', m'_J\right\rangle\right| \tag{2.51}$$

which can also be written as a rank 1 spherical tensor. The second term of the series is the quadrupole moment, and is proportional to a rank 2 spherical tensor:

$$\Omega_{\mathrm{E2}} = \frac{eE}{2\hbar}\left|\left\langle\gamma, J, m_J\right|(\boldsymbol{\epsilon}\cdot\boldsymbol{r})(\boldsymbol{k}\cdot\boldsymbol{r})\left|\gamma', J', m'_J\right\rangle\right|. \tag{2.52}$$

We then recall the Wigner-Eckhart Theorem as in [65]:

$$\left\langle\gamma', J', m'_J\right|T_q^{(k)}\left|\gamma, J, m_J\right\rangle = \frac{1}{2J+1}\langle Jm_J; kq|J'm'_J\rangle \times \langle\gamma J||T^{(k)}||\gamma' J'\rangle, \tag{2.53}$$

where $\langle Jm_J; kq|J'm'_J\rangle$ is a Clebsch-Gordan Coefficient, and $\langle\gamma J||T^{(k)}||\gamma' J'\rangle$ is a reduced matrix element. Equation 2.52 becomes (from [60]):

$$\Omega_{\mathrm{E2}} = \frac{eE}{2\hbar}\langle\gamma J||r^2\boldsymbol{C}^{(2)}||\gamma' J'\rangle \sum_{q=-2}^{+2}\begin{pmatrix} J & 2 & J' \\ -m_J & q & m_J\end{pmatrix}\epsilon_q^{(2)}, \tag{2.54}$$

[6] If one wanted to look at a laser field with some ellipticity, or circular polarization, Spencer William's work [80] offers a nice treatment, as will his future PhD Thesis. Since we are only aiming to use the 2051 nm laser to populate sublevels, this is beyond the scope of this work.

where $\boldsymbol{C}^{(2)}$ is a rank-2 spherical tensor operator, and $\epsilon_q^{(2)}$ are defined in Equations 2.55, 2.56 and 2.57 with a familiar Wigner-3j symbol reappearing. One can do some geometry to determine the angular relations in terms of the alignment angle, ϕ, and the polarization angle, γ,

$$\epsilon_0^{(2)} = \frac{1}{2}|\cos(\gamma)\sin(2\phi)|, \tag{2.55}$$

$$\epsilon_{\pm1}^{(2)} = \frac{1}{\sqrt{6}}\left|\cos(\gamma)\cos(2\phi) + i\sin(\gamma)\cos(\phi)\right|, \tag{2.56}$$

$$\epsilon_{\pm2}^{(2)} = \frac{1}{\sqrt{6}}\left|\frac{1}{2}\cos(\gamma)\sin(2\phi) + i\sin(\gamma)\sin(\phi)\right|. \tag{2.57}$$

For quick reference, contour plots of these functions can be found in Figure 2.6. To compare

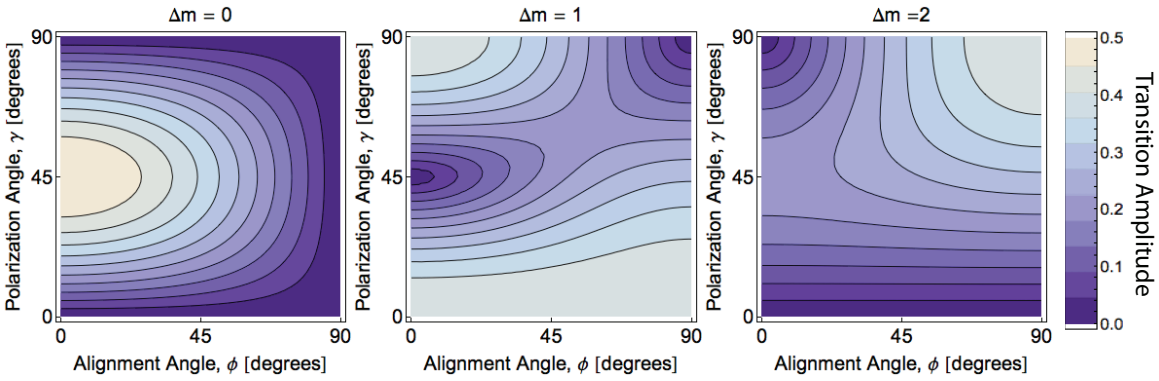

Figure 2.6: Transition amplitudes for E2 transitions depending on polarization angle and orientation angle.

transition strengths for $^{138}Ba^+$ and $^{137}Ba^+$, the addition of nuclear spin alters Equation 2.54 to:

$$\Omega_{\mathrm{E2}} = \frac{eE}{2\hbar}\langle\gamma, I, J, F, m_F||r^2\boldsymbol{C}^{(2)}||\gamma', J', I, F', m_F'\rangle \sum_{q=-2}^{+2}\begin{pmatrix} J & 2 & J' \\ -m_J & q & m_J \end{pmatrix}\epsilon_q^{(2)}. \tag{2.58}$$

So, we need to relate the two reduced matrix elements to understand the transition strengths. We also note that all of the angular dependence on polarization and orientation remains the same. There is a nice relation of spherical tensor operators when the operator commutes

with one of the angular momenta, namely the nuclear spin. This is fleshed out nicely in [37] in Appendix A1, but will be recounted here. We'll use the three angular momenta of our states, but it is a general relation. If an operator T^k commutes with $\boldsymbol{I}$ for states in the basis $|\gamma, I, J, F, m_F\rangle$ we can write:

$$\langle \gamma, I, J, F||T^k||\gamma', J', I, F'\rangle = (-1)^{J+I+F'+k}\langle \gamma, I, J||T^k||\gamma', J'\rangle\sqrt{(2F+1)(2F'+1)}\begin{Bmatrix} J & F & I \\ F' & J' & k \end{Bmatrix}. \quad (2.59)$$

The reduced matrix element found here is now identical to that found in Equation 2.54 once we choose a rank-2 operator, such that $T^{(2)} = r^2 C^{(2)}$, so that the comparison in Rabi frequencies can be made with the addition of these prefactors. Using a relation like this can be employed again, since the electric quadrupole operator commutes with the spin, $\boldsymbol{S}$, but not the orbital angular momentum $\boldsymbol{L}$. This can be useful when comparing theoretical calculations with experimental observations.

2.3.4 Optical Pumping Strategies for $^{138}Ba^+$ and $^{137}Ba^+$

To perform state initialization we need to deterministically populate one of the ground state levels. To describe how to exploit the selection rules, we can rewrite Equation 2.51 using the Wigner-Eckhart Theorem as:

$$\Omega_{\mathrm{E1}} = \frac{1}{2J+1}\langle J m_J; 1q|J' m'_J\rangle \times \langle \gamma J||T^{(1)}||\gamma' J'\rangle. \quad (2.60)$$

Now, depending on the orientation and alignment of a laser with respect to the quantization axis defined by $\boldsymbol{B}$, we can choose to drive only π-transitions with $\Delta m_J = 0$, or $\sigma^{\pm}$-transitions with $\Delta m_J = \pm 1$. For example, if one had a laser co-propagating with the magnetic field with right-handed circular polarization, then only $\Delta m_J = +1$ transitions are driven. If the transition is from $J = \frac{1}{2} \leftrightarrow J' = \frac{1}{2}$, as is illustrated in Figure 2.7, and if the atom is in $m_J = -\frac{1}{2}$, it can be driven up to $m'_J = +\frac{1}{2}$, where it will spontaneously decay to either of the ground states. If it is in $m_J = +\frac{1}{2}$, then the light has no excited state to address, so the ion will remain in $m_J = +\frac{1}{2}$. This process is called optical pumping, and allows us to

prepare the initial state of our atom with high fidelity, as shown for $6S_{1/2}, m_J = -1/2$ in Figure 2.7.

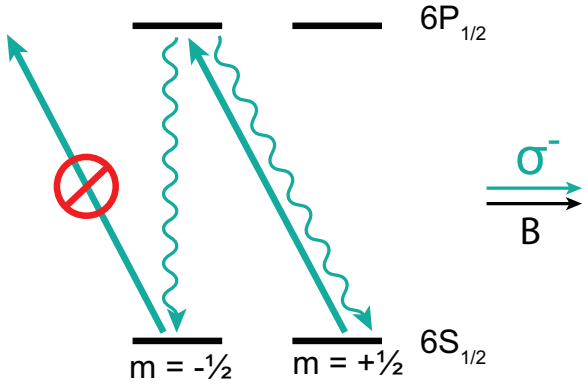

Figure 2.7: Optical pumping strategy for $^{138}Ba^+$, $6S_{1/2}$, $m_J = -1/2$. The repump laser is not shown here, but populates both sublevels of $6P_{1/2}$, which decay into the ground state. The σ^- polarized light drives $\Delta m_J = -1$ transitions, so since there is no possible transition from $6S_{1/2}$, $m_J = -1/2$, the ion will stop fluorescing and has a high probability of remaining there.

The situation is a little bit more complicated in $^{137}Ba^+$, since there is higher angular momentum, however the trick still applies. Light with $\sigma^\pm$ polarization will optically pump the ion to "stretched states" as shown in Figure 2.8, while if one has linear polarization aligned with the magnetic field, only the $m_F = 0 \leftrightarrow m'_F = 0$ transition is forbidden. This can be useful for initializing the ion for the clock transition in $^{137}Ba^+$ as described in [66].

2.3.5 Destabilization of Dark States

If one employs optical pumping, for example with a $\sigma^\pm$-polarized laser beam, the atom quickly ceases to fluoresce, which leads us to say that the ion is in a "dark state". If one has a laser with linear polarization, co-propagating along the quantization axis, however, this light can be thought of as an equal superposition of σ^+ and σ^- light, which will drive all of the transitions out of the ground state. This choice ensures that the atom will be excited repeatedly, constantly absorbing and emitting photons, allowing for such useful processes as

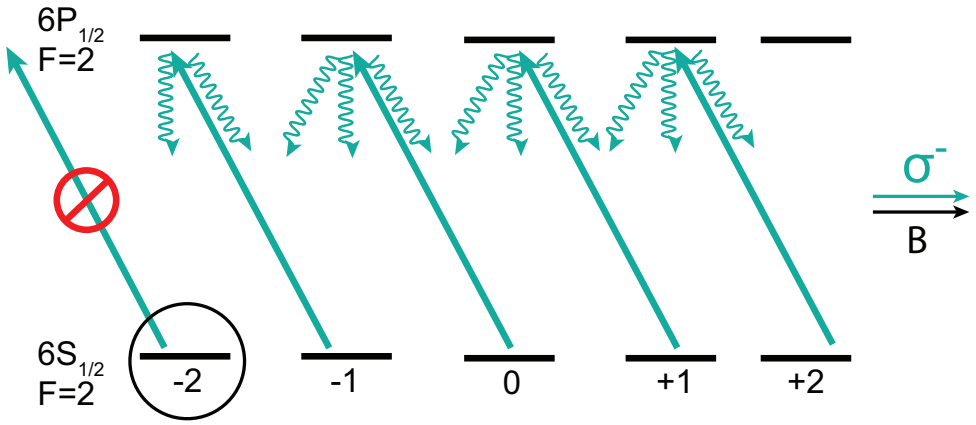

Figure 2.8: Optical pumping strategy for $^{137}Ba^{+}$, $6S_{1/2}$, $m_F = -2$. Similar to the strategy for $^{138}Ba^{+}$, the σ^{-} polarized light drives $\Delta m_F = -1$ transitions, so since there is no possible transition from $6S_{1/2}$, $m_F = -2$, the ion will stop fluorescing and has a high probability of remaining there. Misalignments of the laser to the magnetic field, and ellipticity of the beam are more obvious as there are more possible states, resulting in lower population buildup in $m_F = -2$. The circularly polarized light has an additional frequency component to address the $6S_{1/2}, F = 1 \leftrightarrow 6P_{1/2}, F = 2$ transitions, and all states have an allowed transition.

Doppler cooling, for example. At low magnetic fields, however, dark states can be formed even for linearly polarized light, for a number of reasons, some of which are detailed in [6]. Loosely speaking, this is because the laser's polarization competes with the external magnetic field as the quantization axis. If this is the case, then dark states start to form, making the Doppler cooling ineffective. This makes the experiment difficult for a number of reasons, and therefore must be avoided. An efficient method to destabilize these dark states is by quickly switching the polarization of the electric field with a fast-switching Pockell Cell as in [14].

This problem is obvious in our trap, even when one is using $^{138}Ba^{+}$. As one decreases the magnetic field amplitude, the ion fluorescence begins to drop at approximately 2 G, and it is difficult to hold on to ions at fields below 1 G because Doppler cooling is less efficient. It is even worse for $^{137}Ba^{+}$ ions, making it quite difficult to work at low magnetic fields.

We have not implemented apparatus to destabilize dark states, but instead worked at high enough magnetic fields to avoid the problem. Employing a secondary set of cooling beams orthogonal to the primary beams seems to help keep the ion scattering photons, however to decrease the magnetic field more, it will be necessary to actively destabilize dark states.

Chapter 3

ION TRAPPING AND COOLING

This chapter will detail some of the relevant techniques employed in our spectroscopic measurements. These fall under a few broad categories, namely: producing, trapping, cooling, and performing spectroscopy of a single Ba ion's atomic structure. In this chapter, we won't go into the operation of any of the laser sources used, but rather simply suppose that light at the necessary frequencies is available for use. These apparatus details can be found in Chapter 4.

3.1 Ion Trapping

If one wanted to manipulate a neutral atom, there are only a few handles to use. For magneto-optic traps for example, the relevant "handle" is the the magnetic dipole moment of the atom, proportional to the Bohr magneton, μ_B. As an example found in [17], one such neutral atom with a magnetic moment of $1\mu_B$ in a magnetic field gradient of 10 T/m, will experience a force of $F_{\text{neutral}} \simeq 10^{-22}$ N. Now, if one had a singly charged ion, in a modest electric field of 10^5 V/m, the restoring force is $F_{\text{ion}} \simeq 10^{-14}$ N, 8 orders of magnitude larger, allowing for much stronger manipulation of the ion.

One serious problem is that one cannot confine a charged particle in a static field alone. This is easy to see by looking at Laplace's equation for free-space: $\nabla^2\Phi = 0$, with a static electric potential $\Phi(x, y, z)$. One cannot produce potentials with local maxima or minima in vacuum, only saddle points. This could result in a potential with a local minimum in two spatial directions, but a local maximum in the third to satisfy Laplace's equation. One way to trap ions with only static fields is the Penning trap (reviewed in [17] and [21]). This trap employs overlapping electric quadrupole and magnetic dipole fields, which cause the ion to be confined to cyclotron orbits in the trap. This type of trap was employed by other groups for some of the precision measurements of the $^{137}Ba^+$ hyperfine structure and

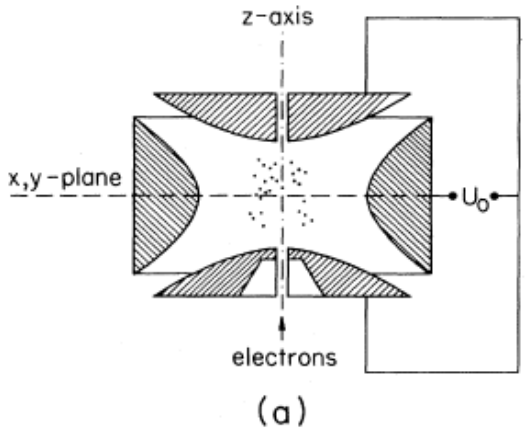

Figure 3.1: Cross-section of Paul trap with hyperbolic electrodes, reproduced from Figure 6a of [55]. The cylindrical geometry, limited optical access, and difficulty of machining the electrodes led to our choice of a linear Paul trap instead.

Landé-g_J factors (e.g. [36] and [74]). Another device that doesn't require a large, static magnetic field uses oscillating fields instead, called the Paul trap [55]. A cross section of this trap can be found in Figure 3.1. This trap design isn't ideal for our experiments, however, mainly because the optical access is very limited for lasers and imaging optics. There are many ways to produce a stable trapping potential, using ring geometries [66], or even blade electrodes, like the "X-Trap" in [51]. We employ a linear configuration with cylindrical electrodes that will be used as an example of how the trap works.

3.2 The Linear Paul Trap

To understand the stability of the linear Paul trap, we will derive the potential, as well as the equations of motion for an ion in these oscillating electric fields. Along the way we will observe "secular" motion as the ion 'sloshes' in the trap, as well as "micromotion" which tracks the oscillation of the electric field itself. For now, let's set up the problem. Suppose we have a singly charged ion, with charge e, and a mass M. It is initially near the center of four electrodes in a configuration like that found in Figure 3.2. There are a pair of endcaps facing into the page that are at a constant, static voltage, but we will ignore them

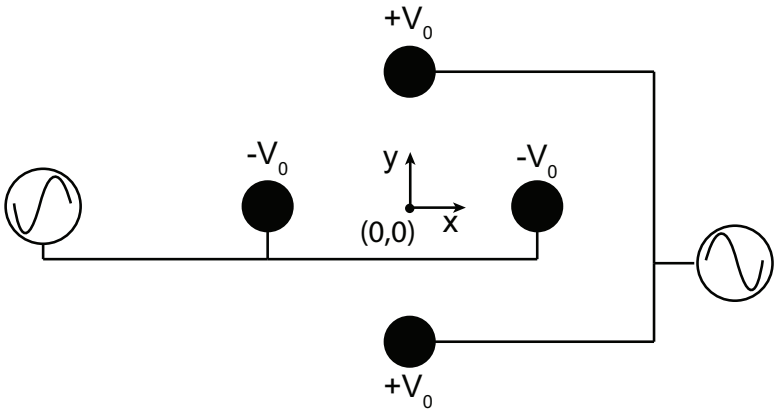

Figure 3.2: Radial cross-section of linear Paul trap (not to scale). The ions are confined at position (0,0), and rf voltage of opposite phase is applied to opposing trap rods a distance r_0 from the trap center. In practice, a pair of the rods are simply grounded, but this produces the same pseudo-potential.

for now. We will suppose that the rods sit a distance r_0 from the center, and that all are at a potential specified by the following boundary conditions:

$$\Phi = \Phi_0 + \frac{V_0}{2}\cos(\Omega_{\rm rf} t) \qquad \text{at} \quad x = \pm r_0, y = 0, \tag{3.1}$$

$$\Phi = \Phi_0 - \frac{V_0}{2}\cos(\Omega_{\rm rf} t) \qquad \text{at} \quad x = 0, y = \pm r_0, \tag{3.2}$$

where $\Omega_{\rm rf}$ is the drive frequency, V_0 is the voltage applied to the electrodes.

These boundary conditions, as well as Laplace's equation are all satisfied by the potential:

$$\Phi(x, y, t) = \Phi_0 + \frac{V_0}{2r_0^2}\cos(\Omega_{\rm rf} t)\left(x^2 - y^2\right). \tag{3.3}$$

This potential has a saddle shape as shown in Figure 3.3. This approximation ignores any effects due to the shape of the electrodes themselves which would need to be hyperbolic to match the potential. These effects are negligible as long as $r = \sqrt{x^2 + y^2} \ll r_0$. Now we take the gradient of the potential to find the electric field:

$$\boldsymbol{E}(x, y, t) = -\frac{V_0}{r_0^2}\cos\left(\Omega_{\rm rf} t\right)\left(x\hat{x} - y\hat{y}\right). \tag{3.4}$$

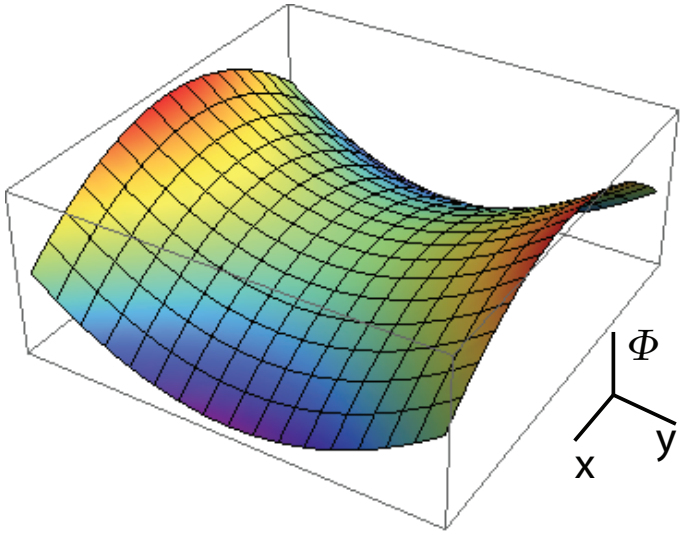

Figure 3.3: Electric potential produced by a linear Paul trap in two spatial dimensions. As time proceeds, this potential "flaps" at a frequency Ω_{rf}. The height and color represent the strength of the potential (red for positive potential and blue for negative potential).

Then in the x-direction, the equation of motion is given by

$$M\frac{\mathrm{d}^2x}{\mathrm{d}t^2} = -\frac{eV_0}{r_0^2}\cos\left(\Omega_{\mathrm{rf}}t\right)x. \tag{3.5}$$

This can be rewritten as

$$\frac{\mathrm{d}^2x}{\mathrm{d}\tau^2} = \frac{-4eV_0}{M\Omega_{\mathrm{rf}}^2r_0^2}\cos(2\tau)x, \tag{3.6}$$

using the change of variable where $\tau = \Omega_{\mathrm{rf}}t/2$. This can be recognized as a particular form of the Mathieu equation:

$$\frac{\mathrm{d}^2x}{\mathrm{d}\tau^2} + \left(a_x - 2q_x\cos(2\tau)\right)x = 0 \tag{3.7}$$

with dimensionless parameters $a_x = 0$ and

$$q_x = \frac{2eV_0}{M\Omega_{\mathrm{rf}}^2r_0^2}. \tag{3.8}$$

There are a family of solutions to the Mathieu equation, but applying approximations relevant to a trapped ion results in a solution of the form:

$$x(\tau) = x_0\cos(A\tau)[1 + B\cos(2\tau)]. \tag{3.9}$$

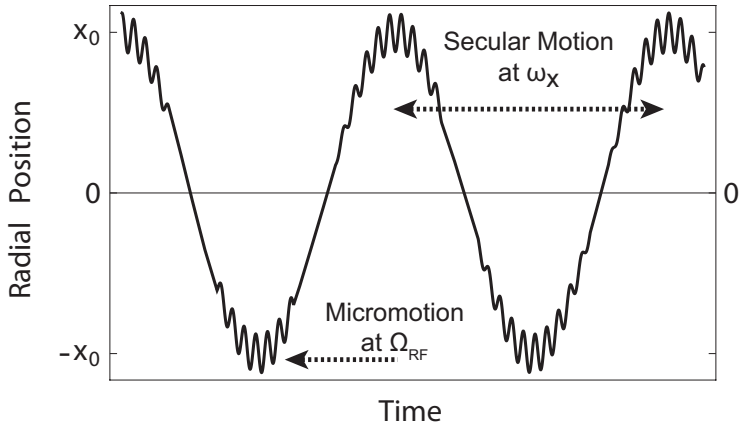

Figure 3.4: Motion of the trapped ion in the radial direction. Parameters used to produce the plot are $a_x = 0, q_x = 0.17$. The slow oscillation is at the secular frequency, ω_x, while the fast oscillation is the driven micromotion at frequency Ω_{rf}.

If we assume that $A, B \ll 1$, then we find that there is a slow oscillation with $A = q_x/\sqrt{2}$, and a fast oscillation at frequency Ω_{rf} with small amplitude $B = -q_x/2$. The frequency of slow oscillation, or secular frequency in the lab parlance is:

$$\omega_x = \frac{q_x \Omega_{\text{rf}}}{2\sqrt{2}}. \tag{3.10}$$

For our trap, we have a driving rf field oscillating at $\Omega_{\text{rf}} \simeq 2\pi \times 11$ MHz, and have observed a radial secular frequency of $\omega_x \simeq 2\pi \times 660$ kHz. This indicates that $q_x \simeq 0.17$. One can also look at stability of the Mathieu equation, and for $a_x = 0$, a stable trapping region exists if $q_x \leq 0.9$ as is found in [17]. We can also make a plot of what the ion's motion looks like in one direction, as shown in Figure 3.4.

Note the small, fast oscillation on the overall slower motion. This fast, driven motion is called "micromotion", and is typically undesirable. Some amount of micromotion is unavoidable, but it can be minimized. Using compensation electrodes, we attempt to minimize excess driven motion by placing the ion as close to the rf-null as possible, as detailed in Section 3.5.

One last note about ion trapping involves the endcap voltages that we ignored earlier. Without endcaps, there is a symmetry axis along the linear Paul trap which is into the

page of Figure 3.2. By applying a positive voltage on the endcaps, we produce a harmonic potential that breaks the symmetry and confines ions between the two endcaps. We call this direction the 'axial' direction, because it lies along the symmetric axis of our trap. We typically have the axial secular frequency lower than the radial secular frequency so that trapped ions will form chains (since they repulse each other) along the trap axis.

3.3 Photoionization

Trivially, to trap Ba^+, one must actually *produce* Ba ions. First, one generates neutral Ba flux by using an "oven". This is typically a small ceramic tube sealed at one end, with a few milligrams of Ba metal deposited into the tube. The tube is pointed at the trapping region with its open end, and is wrapped tightly with tungsten wire, so that when a current is run through the wire, the oven will heat up to a few hundred °C and some Ba evaporates through the trapping region. The ionization energy of neutral Ba is 5.21 eV corresponding to photons at 238 nm [30]. Several methods have been employed in our laboratory to produce the necessary energy to ionize Ba, including an electron beam [66], and a Xe arc lamp, which emits UV light with sufficient energy. These methods, however, are not isotope selective, so one must stochastically load. This is typically fine if one is using $^{138}Ba^+$, which is approximately 70% of natural barium metal. But if one wants to load $^{137}Ba^+$ (only 11% abundance in natural Ba[1]), or another isotope, one must attempt to trap a single ion many times before the desired isotope is the only ion in the trap. It can also prove vexing, because hot, trapped, $^{138}Ba^+$ can make it difficult to tell if a $^{137}Ba^+$ has been successfully loaded into the trap.

For these reasons, we elected to use a two-photon isotope selective photoionization scheme, developed by Michael Chapman's group at Georgia Tech [71], and reproduced in our group by Matt Dietrich [15]. An external cavity diode laser operating at 791 nm excites the neutral barium atom from its ground state $6s^2$ ($^1S_0$) to an excited state $6s6p$ ($^3P_1^o$) via a weak intercombination line (linewidth $\simeq$ 50 kHz). This is a semi-forbidden transition since it changes the spin S (violating one of the selection rules for LS-coupling

[1]One can use an isotopically enriched sample of Ba, but it typically comes in form of barium carbonate, which must be heated to very high temperatures to release barium atoms as in [66].

in Table 2.6). Detailed in [24] and [71], the isotope shifts are resolvable in the spectrum of Ba. For $^{137}Ba^{+}$, the hyperfine structure causes large shifts of the 791 nm transition. After excitation to $6s6p$ ($^{3}P^{o}$), a laser operating at 337 nm completes the ionization. An energy level diagram of this two-photon ionization process can be found in Figure 3.5.

The photoionization laser should be aligned to be perpendicular to the neutral Ba flux to prevent Doppler shifts and minimize Doppler broadening of the 791 nm transition. In a previous version of our ion trapping apparatus, the barium flux was at 45° from the 791 nm beam, and this caused shifts of approximately 400 MHz and reduced isotope selectivity.

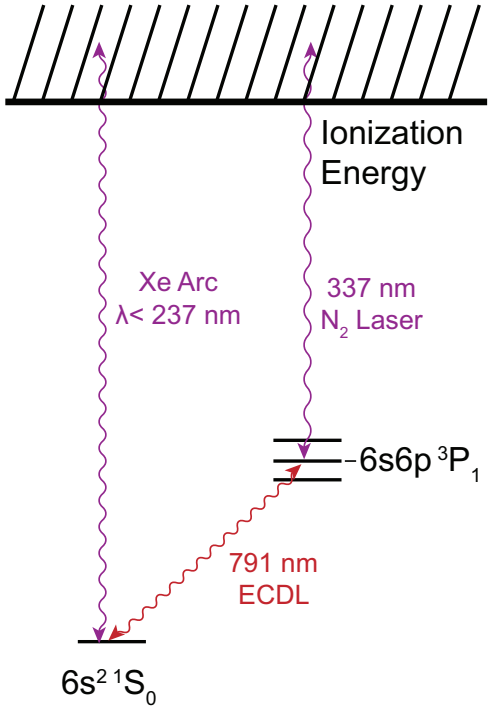

Figure 3.5: Energy level diagram for Ba with relevant photoionization transitions. One can directly ionize with a photon at 237 nm, but this will ionize all isotopes of Ba. Instead a two-photon process allows for isotope selectivity.

3.4 Laser Cooling of Trapped Ions

The newly ionized ion is now confined in the trap, however it is not an ideal system to work with. It still has all of the momentum from being evaporated from the oven, and is not well localized in the trap. Waiting for it to cool to room temperature would take a very long time because the only damping force would be from collisions with background gases, but those are few and far between because the ion is in UHV. Thus, we must actively cool the ion to get the control we need for precision measurements.

Laser cooling is certainly not a new concept, and was first demonstrated in 1978 [81], with a detailed theoretical treatment the following year [82]. The first work brought magnesium ions down to 40 K, with the last sentence of the article being "Cooling to approximately 10^{-3} K should be possible". This certainly does prove possible and has been demonstrated in many ion species over the years. We will now go through the derivation for the Doppler limit of trapped Ba^+.

The whole point of Doppler cooling is to cause the ion to preferentially absorb photons when it is traveling towards a laser beam. Each photon carries a little bit of momentum that serves to slow the ion, which then spontaneously emits a photon in a random direction. What we really care about is how many photons are scattered as a function of the laser's detuning. For this derivation we will assume that we have a 2-level system[2]. Now we setup the problem. Suppose that we have a laser field at 493 nm of intensity I that is near resonant with the $6S_{1/2} \leftrightarrow 6P_{1/2}$ transition (detuning $\delta = \omega - \omega_0$) with a saturation parameter $s = I/I_{\text{sat}} = 2\Omega^2/\Gamma^2$, where Ω is the Rabi frequency. $6P_{1/2}$ has a lifetime, τ, which causes a natural linewidth of $\Gamma = 1/\tau$. The saturation intensity I_{sat} is the radiation intensity where the atom spends approximately half the time in the excited state and half in the ground state. Finally suppose that the ion is sitting in a harmonic potential well with frequency ω_z, and has a velocity ν. The scattering force from this laser field (since

[2]In actuality, since Ba^+ is a Λ-type system, there are three levels, requiring a repumping laser. This adds some complications which are addressed in [47] and changes the resonance spectrum [53]

each photon has momentum $\hbar k$) is given by [17]:

$$F_{\text{scatt}} = \frac{\hbar k \Gamma}{2} \frac{s}{1 + s + \left(\frac{2(\delta + k\nu)}{\Gamma}\right)^2}, \tag{3.11}$$

where k is the wavenumber of the photon. We then perform a Taylor expansion about $\nu = 0$, to first order:

$$F_{\text{scatt}} \simeq \frac{\hbar k \Gamma s}{2} \left(\frac{1}{1 + s + 4\delta^2/\Gamma^2}\right) \cdot \left(1 - \frac{8k\nu\delta/\Gamma^2}{1 + s + 4\delta^2/\Gamma^2}\right). \tag{3.12}$$

We want to express this as a damped harmonic oscillator of the form:

$$F_{\text{total}} = -m\omega_z^2(z - z_0) - \alpha\nu \tag{3.13}$$

where z_0 is the equilibrium position of the ion, and α is the damping coefficient. Identifying the first term of Equation 3.12 with z_0 we find:

$$z_0 = \frac{1}{m\omega_z^2} \frac{\hbar k \Gamma s}{2} \left(\frac{1}{1 + s + 4\delta^2/\Gamma^2}\right), \tag{3.14}$$

and

$$\alpha = -\frac{4\hbar k^2 s\delta/\Gamma}{(1 + s + 4\delta^2/\Gamma^2)^2}. \tag{3.15}$$

This means that our ion is offset from the center of the trap due to radiation pressure. Then to find the maximum damping force, we must maximize α with the free parameters s and δ. This results in $s = 2$ so $I = 2I_{\text{sat}}$ and $\delta = -\Gamma/2$. These parameters inform us that the intensity of the incident light should be half the saturation intensity, and detuned from the resonant frequency by half the linewidth of the transition.

Laser cooling by scattering photons will occur until the ion loses enough kinetic energy such that each photon absorption is essentially balanced by the momentum from the spontaneous emission. The Doppler cooling limited temperature is:

$$T_D = \frac{\hbar\Gamma}{2k_B}, \tag{3.16}$$

where k_B is the Boltzmann constant. We can then invoke the equipartition theorem to look at what the average occupation number $\bar{n}$ of our trap simple harmonic oscillator hamiltonian

is. Since we keep the axial potential the weakest, it will also have the highest average occupation number, $\bar{n}_z$ given by

$$\bar{n}_z \hbar \omega_z = k_B T_D \tag{3.17}$$

so for the Doppler cooling limit we arrive at

$$\bar{n}_z \approx \frac{\Gamma}{2\omega_z}. \tag{3.18}$$

Taking $\Gamma = 1/\tau$ where $\tau = 8$ ns, and $\omega_z = 2\pi \times 440$ kHz we arrive at $\bar{n}_z \approx 23$ for an ion at the Doppler limit, or a temperature of ≈ 500 μK . If there is too much or too little laser power, or if the detuning of the laser(s) is not correct, the ion won't reach the Doppler limit, but we can typically cool to within a few times T_D. In Section 5.1 we will work through how to measure the ion's average occupation number as in [60], and accordingly, the temperature. For now, it will suffice to say that our ion will typically be at a temperature several times larger than the Doppler limit. As long as the ion is near the Doppler limit, we need not worry about the details of its temperature for many aspects of our spectroscopy.

3.5 Micromotion Compensation

There are techniques to effectively cancel out the excess micromotion observed when an ion is displaced from the rf null of the trap, as found in [7], which we have employed at various times. The first is to simply change the depth of the rf trap by adjusting the rf voltage, and then observe how the ion's trapping position changes. If the rf trap is deeper, then the ion will move closer towards the rf-null. One can use this information to change compensation electrode voltages to push the ion towards the rf-null so that the ion's position does not change when the rf trapping potential is changed. We find that in our trap, this procedure must be used nearly every day, and otherwise trapping and cooling may be difficult due to excess micromotion.

The second technique relies on monitoring fluorescence from the ion as it undergoes micromotion. If there is correlation between the drive rf phase and the number of photons detected by our PMT, then the ion is undergoing driven micromotion. The difference in fluorescence is due to preferential absorption via the Doppler shift when the ion is moving towards the laser, as detailed in Section 3.4. At one point, Adam Kleczewki and I borrowed

the necessary equipment to minimize excess micromotion as detailed in [33]. Essentially, a time to amplitude converter (TAC), borrowed from Professor Alejandro Garcia, is triggered on the detection of a photon on the PMT. A TTL signal is generated at the beginning of the trap rf phase, which is used to stop the counter of the TAC. Thus, the time elapsed between the collection of a photon and the end of an rf period is converted to an analog voltage.

This voltage is measured with a pulse height analyzer, borrowed from Dr. David Pengra's advanced laboratories. It binned the number of photons collected at a given rf phase. After a minute or two, enough statistics are accumulated to reveal a signal like that shown in Figure 3.6. The blue and red colors indicate that the micromotion was over and under compensated respectively, and show opposite phase from the trap rf voltage. Tuning up the compensation voltage to produce a histogram like that of the gold plot markers, indicates that the micromotion is well compensated along the $\boldsymbol{k}$-vector of the cooling laser. Since this is typically parallel to the optical table, this means that excess vertical micromotion remains uncompensated. To compensate this direction of micromotion, an additional 493 nm laser beam with a vertical component with respect to the table would be necessary.

For high precision experiments, like the proposed PNC experiment [18], or the measurement of the magnetic dipole transition element of the $6S_{1/2} \leftrightarrow 5D_{3/2}$ [80], implementing a permanent setup to compensate micromotion by correlating photon arrival with the rf phase would be quite useful, and quite possibly necessary for high enough precision[3].

We have observed in our trapping apparatus that long periods of loading cause the micromotion to become uncompensated. The working hypothesis is that as the Ba oven is run over time, Ba collects on all of the trapping rods. When the N_2 laser flashes, it has sufficient energy to ionize some of the deposited barium, creating patch potentials which displace the ion from the rf-null. The work function of barium on metal is approximately 2.5 eV, so even the 493 nm and 455 nm lasers can create these patch potentials [26]. It is essential to ensure that lasers with sufficient energy to ionize the barium metal are not incident on the trapping structures.

[3]This would involve the acquisition of a pulse-height analyzer, and a time to analog converter. Otherwise, with our setup, this would be relatively easy to implement.

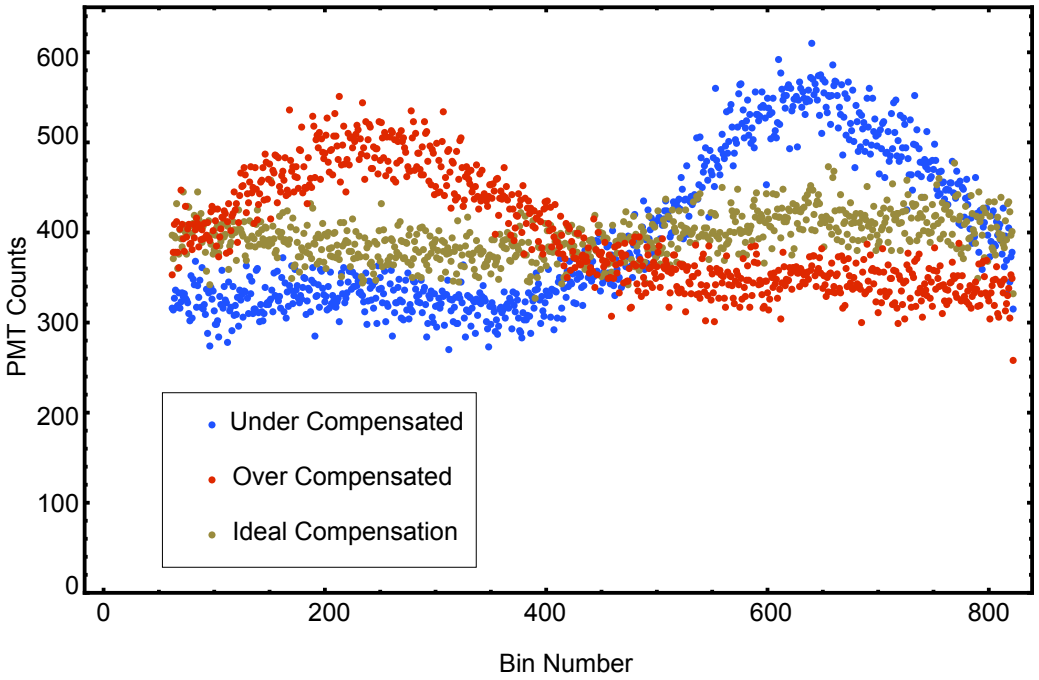

Figure 3.6: Micromotion compensation using correlation between scattered photon rate and rf phase. The three colors show when the compensation electrode voltage was too low (shown in blue), too high (shown in red), and close to perfect (shown in gold).

We have observed similar effects to [26], but have not quantitatively measured them. At one point, when using a 455 nm LED to shelve the ion, the focus of the light was somewhat poor, so light was incident on the barium rods. It got to the point that one could trap a Ba^+, compensate the micromotion, and observe that it was well laser cooled using the EMCCD camera. After a few shelving and deshelving pulses, the ion noticeably drifted from its previous position and micromotion was visibly un-compensated. Upon dumping the ion and re-loading, the micromotion was observed to be compensated until pulses of the 455 nm light were used. This frustrating problem was remedied by running currents of several amperes through each trap rod for a couple of minutes to evaporate barium metal that was deposited. We observed an immediate effect, and temporarily eliminated the recurrence of the problem.

These patch potentials can have lifetimes of several days[4], so loading ions for hours at a time (which requires nearly constant use of the N_2 laser) can make the compensation voltages increase to $\sim$ 500 V. At any rate, a quick and improved method of micromotion compensation would be highly beneficial to our experiment, and improve the ion's temperature

The reason that we care about this is that the ion can experience an ac-Zeeman effect due to its motion in a magnetic field gradient. In the reference frame of the ion, there is an oscillating magnetic field at the trapping frequency $\Omega_{\rm rf}$, which can cause off-resonant shifts to the energy levels, arising as a systematic effect for the high precision experiments we have undertaken. This effect is discussed in detail in Chap 6.

3.6 Quantum Jump Spectroscopy

We will revisit the energy level diagram of Ba^+ as shown in Figure 2.1, and consider an example of how spectroscopy with 2051 nm laser is performed. One begins the process by laser cooling the ion with light at 493 nm and 650 nm as described in the previous section. While both lasers are on, the ion is constantly scattering photons which are observable with the photon collection scheme found in Section 4.3.2. If one was to block the 650 nm laser, then the 493 nm light would excite the ion to $6P_{1/2}$ which could either decay to $5D_{3/2}$ (where it would remain on average for $\approx$ 80 s), or decay back to $6S_{1/2}$ which would be re-excited by the 493 nm light. After only a few scatters it would end up in $5D_{3/2}$ and would stop fluorescing. When we expose the ion to 650 nm light again, it would start scattering photons again. We collect only the photons emitted on the $6P_{1/2} \rightarrow 6S_{1/2}$ decay at 493 nm, so when the ion is cycling between the $6S_{1/2} \leftrightarrow 6P_{1/2} \leftrightarrow 5D_{3/2}$ levels we will say that the ion is "bright".

Now suppose that in addition to the 493 nm and the 650 nm light, we expose the ion to 455 nm light, which excites the ion to $6P_{3/2}$ with a short lifetime $\tau \approx 6$ ns. From here, three things can happen. Approximately 75% of the time, the ion decays back to $6S_{1/2}$ where it is re-excited back to $6P_{3/2}$. Approximately 3% of the time it will decay to $5D_{3/2}$ where it

[4]For example, [26] observed a lifetime of $\tau \sim$11 days.

will be re-excited back to $6P_{3/2}$ via $6P_{1/2}$ and $6S_{1/2}$. The last case, about 23% of the time, it will decay to $5D_{5/2}$, where it will remain for approximately 30 s. It is now completely removed from the cooling cycle. When the ion is in the metastable $5D_{5/2}$ we refer to it being "shelved" or "dark". The ion can be returned to the cooling cycle by exposure to 614 nm light, referred to as "deshelving". This is more convenient than waiting the 30 s for the ion to spontaneously decay. Figure 3.7 shows an example of the number of photons detected on our PMT as a function of time with "shelving" and "deshelving" pulses.

Transferring the ion to $5D_{3/2}$ via the $6P_{3/2}$ is referred to in the literature as indirect-shelving and has a few downsides. The first is that usually the 493 and 650 nm lasers are shuttered during the shelving pulse due to experimental considerations, so the ion is transferred to $5D_{3/2}$ with some probability. With a sufficiently long pulse of 455 nm light, the ion will be transferred to the $5D_{5/2}$ "dark" state approximately 89% of the time, and to the $5D_{3/2}$ which is a "bright" state the other 11% of the time [38]. This results in lower contrast for our experiments, requiring that we take additional data to increase the signal to noise ratio. The 455 nm light will depopulate all of the Zeeman sublevels of $6S_{1/2}$, for better or worse.

The other way to shelve the ion is to use an electric quadrupole transition to directly transition from $6S_{1/2}$ to $5D_{5/2}$ employing a narrow-band laser at 1762 nm. This is often referred to as the direct shelving method. These transitions are state selective and can be tuned such that only one of the Zeeman sublevels of $6S_{1/2}$ is "shelved" with nearly unit probability using either a π-pulse or ARP as in Sections 2.3.1 and 2.3.2.

Through the experiments described in this work, we have employed both direct and indirect shelving at various times. If one is to employ indirect shelving, an experiment must be designed such that the ion is either in $6S_{1/2}$ or $5D_{3/2}$ after a sequence of operations to perform state detection.

As a quick historical note, the technique of quantum jump spectroscopy was famously pioneered here at the University of Washington using Ba^+ by Hans Dehmelt's group (who called it a "shelved optical electron amplifier") [49]. Most specifically, it allows one to observe a single quantum jump with nearly unit certainty. For example, if the ion was sitting in $5D_{5/2}$, one could simply wait with the cooling and repump beams exposed. As

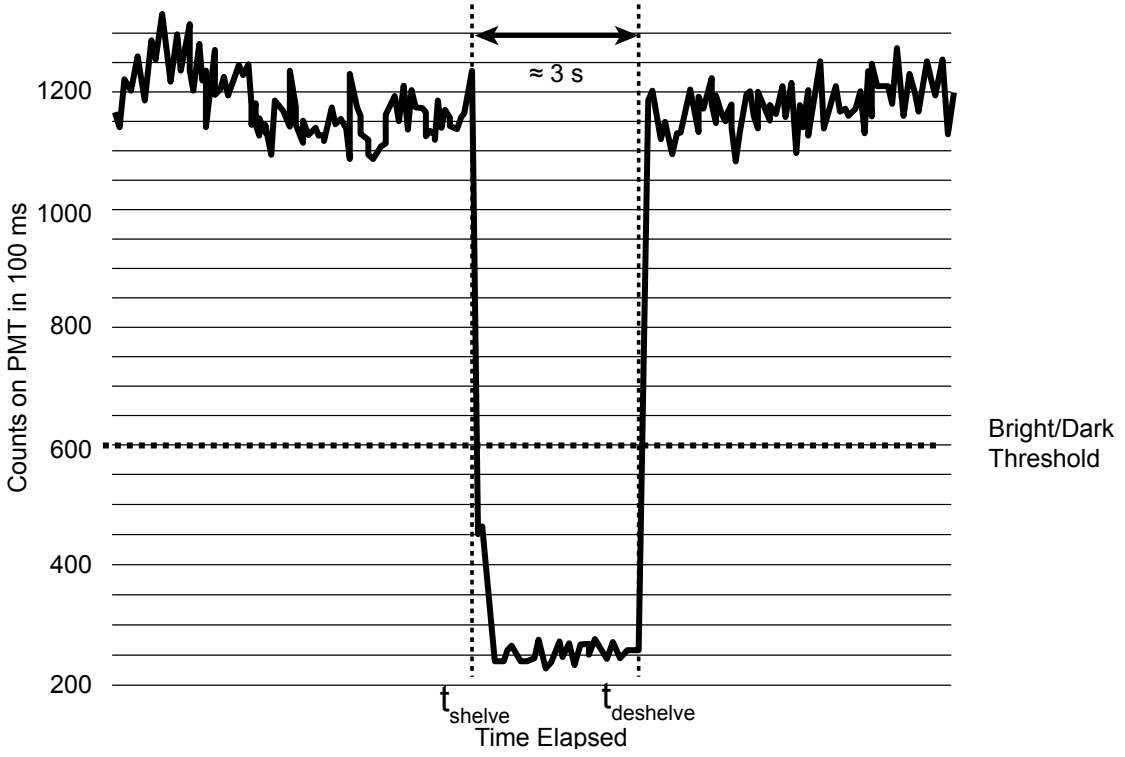

Figure 3.7: Photons collected by the PMT when the ion is cycling on the cooling transition and shelved. The PMT counts in 100 ms bins as a function of time are shown in black. The first vertical dashed line indicates when a 10 ms 'shelving' pulse removed the ion from the cooling cycle, making it 'dark'. Approximately 3 s later, a pulse of 614 nm light 'deshelved' the ion back to the cooling cycle, making it 'bright'. The horizontal dashed line shows a typical threshold between 'bright' and 'dark'. Usually, we count in shorter periods, between 20 and 50 ms.

soon as the ion starts fluorescing, it is obvious that it has transitioned back to one of the cooling levels. The single emitted photon would be nearly impossible to measure, but this technique makes it quite simple to observe that a transition occurred.

Chapter 4

APPARATUS

4.1 Laser Systems and their Characterization

In this section, we'll get into the gritty detail of how our lasers are set up, and discuss their performance. I call it characterization, as it sometimes feels like each laser has its own unique personality. Some are rather finicky, and if perturbed, will 'misbehave' for hours. Others sometimes seem relatively easy going, and aren't tough to get them to do what you want. I fully realize that all of their behavior can be attributed to the control electronics and the semiconductor physics, but in any event, this is how our system is set up and some of the reasons why we chose to set it up this way.

4.1.1 986/493 nm Laser

A future reader of this work will probably ask themselves, "why did anybody ever use 986 nm lasers? Why not just a laser diode at 493 nm?" The obvious answer is that we couldn't. However, even as this text is written, Toptica Photonics sells a number of laser diodes that operate at 493 nm directly, with up to 200 mW of CW laser power. Unfortunately, this is a recent development, so these diodes did not exist when our apparatus was being set up. It would behoove a future researcher, upon experimental breakdown, to replace a 986 nm laser with one at 493 nm. With that caveat in mind, this section will detail the construction and characterization of our 986/493 nm laser system. A schematic of the optical path of this laser beam can be found in Figure 4.1.

Approximately 15 mW of 986 nm light is produced by a Toptica DL Pro ECDL system. The laser itself is remarkably stable, and only mode-hops once a month or so. This owes to the fact that the diode is AR-Coated, additionally allowing for a large mode-hop free range in excess of 15 GHz, and is only slightly susceptible to slow drifts in frequency. This beam is passed through an optical isolator, and anamorphic prism pair, and is then coupled

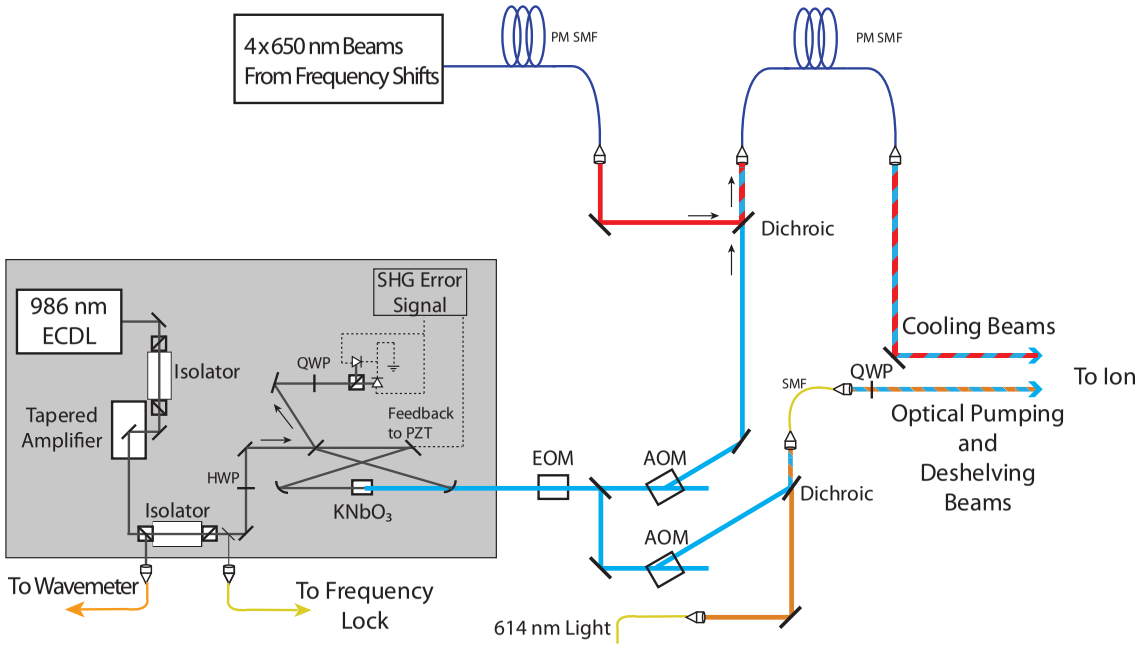

Figure 4.1: Schematic for 986/493 nm SHG system with bow tie cavity. As detailed in the text, 493 nm with sidebands for addressing two $^{137}Ba^{+}$ is created using a "bow-tie" SHG system. This light is split into two paths and combined with the 650 nm laser beams, and 614 deshelving beam respectively.

into a Sacher-Lasertechnik Serval^{TM} Tapered Amplifier (TA) system. The 15 mW of seed power is amplified to approximately 250 mW near the limiting current of $\sim$ 3000 mA to the TA. We suspect that the TA is being under-seeded, resulting in lower output power than one would expect[1]. It also appears that since the TA is not being seeded enough, it is spontaneously emitting light, which degrades the lifetime. For this reason, we replaced the tapered amplifier chip in 2010, and will likely need to do so in the next year or two, as the output power has dropped over time.

The output beam of the TA system is passed through another optical isolator with 60 dB isolation. Some of the light that is rejected by the first polarizer of the isolator (only a few mW) is coupled into a MM fiber which runs to the wavemeter so that we can monitor the laser's frequency easily. The light that passes through the optical isolator is split into two beams. A few percent is coupled into a SM fiber for frequency stabilization, and the remainder is aligned into a "bow tie" enhancement cavity.

The few percent that is picked off is frequency shifted using a double-passed acousto-optic modulator (DPAOM) scheme and coupled into an optical reference cavity as shown schematically in Figure 4.2. We employ a scheme like this for the 650 nm and 2051 nm lasers as well, so this discussion applies to those systems. First, the beam leaves the SMF and is collimated. The horizontal polarization component of the light first transmits through a polarizing beam splitter (PBS), and is then focused through AOM where it is upshifted by a tunable frequency of 200 ± 30 MHz. The first-order upshifted beam is then re-collimated by a spherical lens and passes through a quarter wave-plate (QWP), so its polarization is now circular. The light is then back-reflected by a mirror, through the QWP a second time, so that its polarization is now vertical. The light is refocused through the AOM, where it is upshifted a second time. After being recollimated, the now vertically polarized beam reflects off the PBS.

The laser is frequency shifted twice for a couple of reasons. First, the angle that the light exits the AOM at is proportional to the frequency that the AOM is being driven at. Thus, in a single-pass configuration, changing the frequency of the AOM will also mis-point the beam,

[1]Our TA chip was tested with approximately 30 mW of 988 nm laser power to produce 125 mW at 2.5 A of current by the manufacturer.

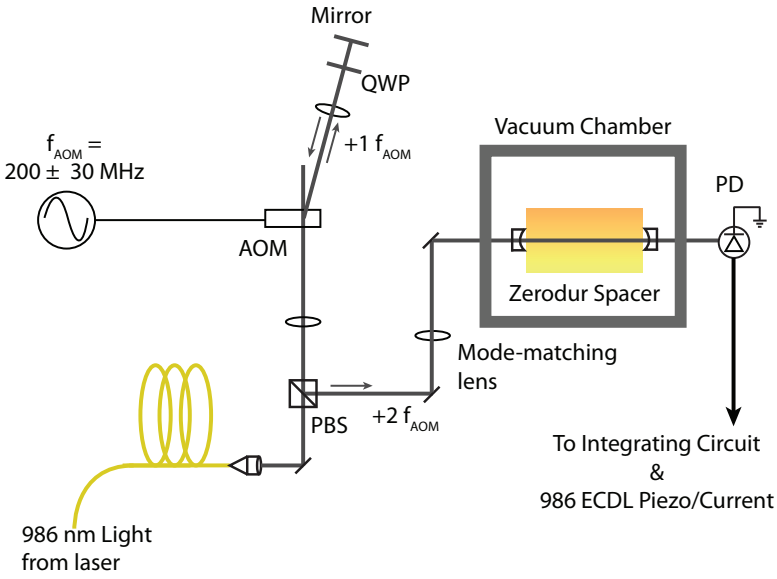

Figure 4.2: Schematic for 986 nm laser stabilization to reference cavity. The light is frequency shifted twice by an AOM, and side-of-the-fringe locked to a Zerodur spaced reference cavity in vacuum.

causing misalignment into the optical reference cavity. In the double-passed configuration, this problem is reduced because the two shifts have equal and opposite angular deflection, which cancel. Secondly, one benefits from the doubled bandwidth of the frequency shift, so that the laser can be tuned by approximately 120 MHz instead of 60 MHz while stabilized to the same mode of the optical reference cavity with only minor repointing to ensure good coupling.

The now doubly upshifted light is then coupled into a Zerodur-spaced reference cavity that was previously used to stabilize the 946 nm laser used in the In^+ experiment as detailed in [75]. This Zerodur cavity was made by Research Electro-Optics and has a free spectral range (FSR) of 509 MHz, and mirrors have a 50 cm radii of curvature, with reflectivity of 99.99% resulting in a finesse of $\mathcal{F}$ ~30,000 at 946 nm [75]. The cavity used to be suspended horizontally by a pair of wires within a vacuum system, however, vibrations on our optical table would cause this cavity to swing for minutes at a time (so that the light

would become uncoupled repeatedly), so it is now resting on a wire rack under vacuum. This mounting solution undoubtedly introduces fast vibrations and thermal coupling, but the length is certainly stable enough so that the laser drifts < 1 MHz/day. Though we are using the cavity at 986 nm instead of 946 nm, the mirrors still have high reflectivity, so that the 986 nm laser is stabilized to a linewidth below what is necessary for effective Doppler cooling.

The transmitted intensity is monitored, and used in a side-of-the-fringe lock. When locked, the laser is observed to "surf" up and down the transmission peak, which undoubtedly broadens the linewidth of the laser, however, the the laser still has a narrow enough linewidth (< 1 MHz) that is sufficient to laser cool on the strong $6S_{1/2} \leftrightarrow 6P_{1/2}$ transition.

Approximately 70 mW of 986 nm light is used for SHG to produce light at 493 nm. This setup is thoroughly detailed in [66], but will be quickly summarized here. The beam passes through a HWP and is mode matched into a "bow tie" cavity. The light passes through the input coupler, and then reflects off of a small mirror mounted to a piezoelectric (PZT) stack. When the voltage applied to the PZT is increased, the stack will expand, decreasing the total length of the cavity and changing the resonant frequency. This reflected light reflects of a high-reflectivity (HR) curved mirror, which brings the beam to a focus. At the waist of the beam lies a Brewster-cut $KNbO_3$ crystal that is temperature stabilized to 28.5 °C, so that it is phase-matched at 986 nm. The details of the SHG process are somewhat beyond the scope of this work, but can be found in a number of sources, for example [75]. Some of the 986 nm light is frequency doubled using the $KNbO_3$ crystal, which overlaps with the 493 nm light. The 986 nm light is reflected off of a custom HR/HT curved mirror for 986/493 respectively, back to the input coupler, while the 493 nm light is transmitted.

The "bow tie" cavity is locked to the 986 nm laser frequency using the Hansch-Coulliaud polarization locking scheme [25]. A schematic can be found in Figure 4.1. The polarization of the light reflected off of the input coupler is monitored keep the cavity resonant to the laser frequency by feeding back to the mirror mounted on the PZT stack. The procedures is as follows. Before being coupled into the "bow tie" cavity, the laser passes through a HWP, which slightly rotates the polarization from vertical. The $KNbO_3$ crystal is a polarization sensitive element, so the doubling cavity has different impedance for horizontal

and vertical polarization (causing a phase shift dependent on whether the light is below resonant frequency, or above). This causes the back-reflected light to be elliptically polarized as a function of frequency, which can be analyzed using a QWP and a PBS. The two outputs of the PBS are monitored by two photodiodes that are connected to a differential amplifier. This produces an error signal, allowing one to feed back to the mirror attached to the PZT stack, and thus stabilize the cavity length to remain resonant to the 986 nm laser frequency. The circuit employed is a custom, homebuilt double integrator circuit. A circuit diagram and discussion of this locking scheme can be found in Appendix A and B of [33].

While the cavity is resonant with the 986 nm light, power will buildup in the cavity resulting in approximately 150 μW of 493 nm light produced by the SHG crystal. This light first passes through an EOM, which generates sidebands at 4018 MHz (half the splitting of the $^{137}Ba^{+}$ ground state hyperfine structure). The microwave signal is generated by a NovaSource G6 direct digital synthesizer that is controlled by the main DAQ computer, passes through an rf switch, and is then amplified using a Minicircuits ZHL16-W-43-S+ amplifier. This amplifier could have a total output power of 16 W, but this much power would destroy the EOM. Approximately 3 W is sent to the EOM to generate sidebands that are approximately 10% of the carrier on the 493 nm light, which can be switched on and off. An approximate spectrum can be found in Figure 4.3. Additionally, for reference in the following discussion, a condensed schematic of the 493 nm laser beam path can be found in Fig 4.1.

The majority of the beam is deflected by a single passed AOM controlled by a TTL signal from the DAQ computer, which acts as a shutter. The +1 deflected spot transmits through a dichroic mirror (so that it can be combined with the 650 nm beams) and is coupled into a polarization maintaining (PM) SMF. The collimated output beam of approximately 40 μW is focused on the ion using an achromatic doublet. When shuttered, a small amount of light ($\sim$ 10 pW) leaks through the optical fiber, but this is on the verge of our detection capabilities. We have observed that this light can cause the ion to be excited to $6P_{1/2}$ and transferred to the $5D_{3/2}$ state during long waits, so to prevent this, we usually cool $^{138}Ba^{+}$ using one of the EOM sidebands, and additionally turn these off when we want to be certain that the light is extinguished. Any light that is leaking is then 4 GHz detuned,

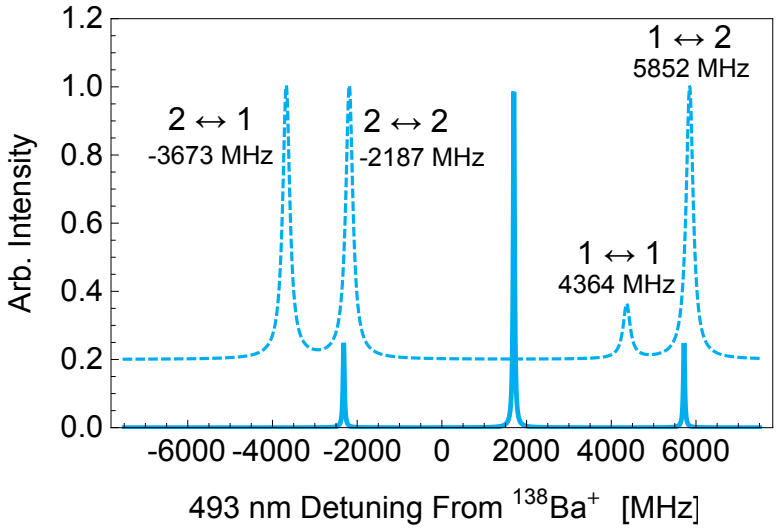

Figure 4.3: 493 nm laser spectrum and absorption lines in $^{137}Ba^{+}$. The solid line shows the laser spectrum with sidebands generated by the EOM. The dashed blue line, offset from zero for clarity shows the four transitions from $6S_{1/2}, F = 1, 2$ to $6P_{1/2}, F = 1, 2$ shifted with respect to the $^{138}Ba^{+}$ transition. The linewidths of the absorption spectrum are not to scale for clarity, however the relative amplitudes are to scale.

causing negligible excitation and light shifts to the ground state.

Approximately 3% of the main beam is picked off using a beam sampler that is wedged at 0.5° to prevent interference fringes. This beam is shuttered using an AOM driven at nearly the same frequency as the main "cooling beam", and is coupled into a PM SMF. The collimated output beam passes through a Glan-Thompson calcite polarizer, and a custom QWP designed for 493 nm light. The adjustable angle of the QWP lets the user retard the beam's polarization so that this light can be linearly, right-handed-circular, or left-handed-circular polarized. Typically the beam is left to be circularly polarized such that it will optically pump the ion into the $m_J = -1/2$ for $^{138}Ba^+$ or $F = 2, m_F = -2$ for $^{137}Ba^+$. The beam of approximately 1 μW is then reflected by a pickoff mirror so that it propagates parallel to the main cooling beam. Using this beam, and the repump laser at 650 nm, one can monitor the ion's fluorescence as the QWP is rotated, observing a minimum as the light becomes circularly polarized. If there is any additional fluorescence, this indicates that there are stray magnetic fields in the horizontal or vertical directions, which can be compensated until the optical pumping beam causes no measurable fluorescence.

4.1.2 650 nm Laser

The prescription for Doppler cooling and photon collection as described in Sections 3.4 and 3.6 would both break down if the ion got stuck in the metastable $5D_{3/2}$ level. To repump the ion so that it can cycle on the cooling transitions, we need resonant light at 650 nm at a single frequency for $^{138}Ba^+$, and several frequencies to repump out of all of the hyperfine levels for $^{137}Ba^+$. To achieve this, we employ an ECDL at 650 nm.

The laser head itself is a New Focus Vortex^{TM} at 469.869 nm [11], with an output power of approximately 8 mW. The light is passed through an optical isolator, such that the beam has linear polarization at 45° relative to the table, which is then split into four beam paths using a PBS and a pair of 50/50 beamsplitters. As depicted in Figure 4.4, a wedged beam sampler takes approximately 3% of one of the four the beams, which is steered to an optical reference cavity for laser frequency stabilization.

One of my first projects in the lab was to design and assemble a reference cavity to

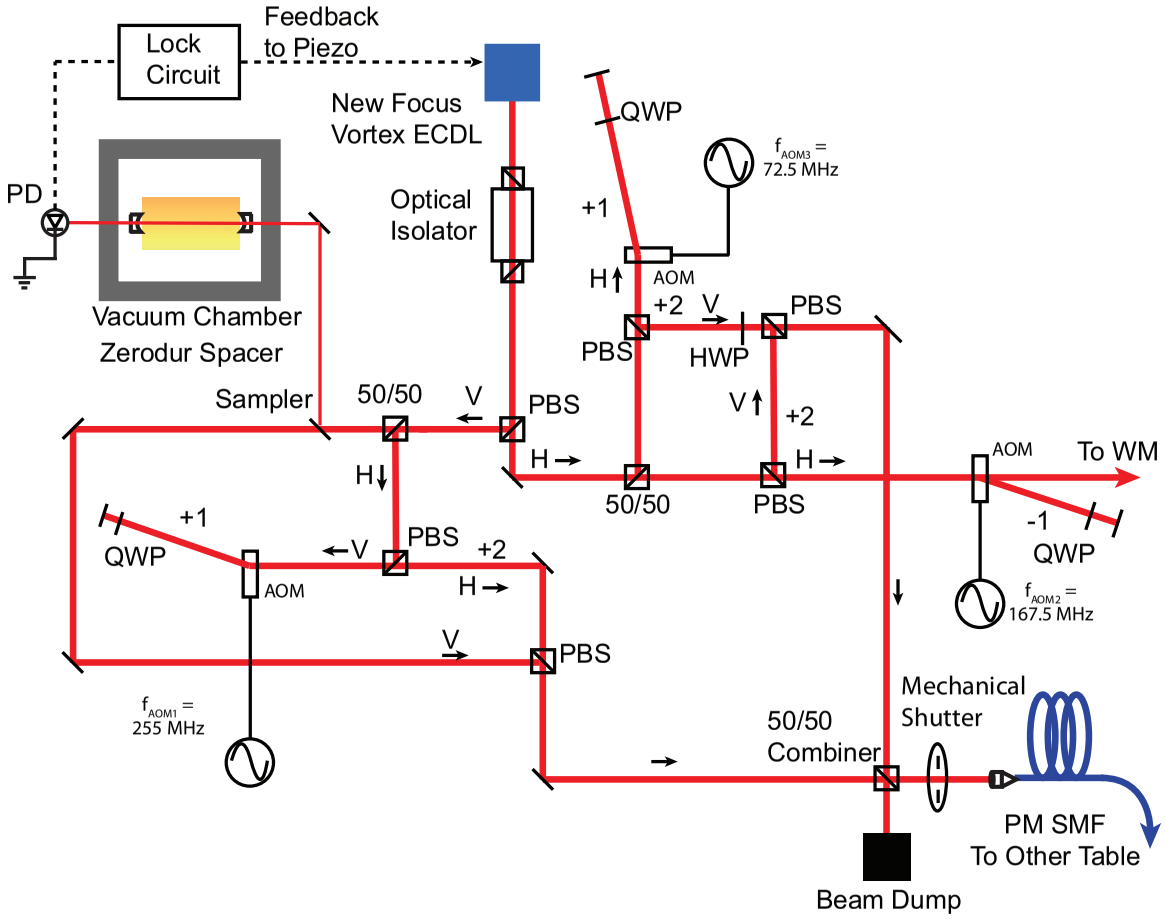

Figure 4.4: Schematic for 650 nm additional laser frequency generation and recombination. The main 650 nm laser beam is split into four paths that are frequency shifted using DPAOMs, and recombined with a combination of PBS and 50/50 cubes. The output of the PM SMF is combined with the 493 nm laser using a dichroic as shown in Figure 4.1.

stabilize the 650 nm laser, and replace the barium hollow cathode lamp (HCL) used in [66]. In addition to having a broad spectral feature (FWHM $\simeq$ 1 GHz), the HCL required several mW of the 650 nm laser beam to generate a good error signal. To keep the laser's linewidth narrow, we elected to lock to an optical reference cavity instead.

The cavity spacer is made of a 9 in. long piece of Zerodur with a diameter of approximately 2 in that was formerly used in the 2 μm system as a scanning cavity. Two custom backside-polished, concave mirrors were purchased from CVI Melles-Griot[2], with 98% reflectivity at 650 nm, a radius of curvature of 0.3 m, a diameter of 1 in., and thickness of 3/8 in. The free spectral range of the cavity is approximately 650 MHz, and the low-order TEM modes are spaced by approximately 100 MHz. The mirrors' reflectivity results in a finesse of approximately 150, resulting in transmission features with FWHM $\simeq$ 4 MHz. The mode matching in our setup is relatively poor, but this allows for one to stabilize the laser to a mode that coincides with the ion's resonance, without the need for a frequency shifting AOM[3]. The reference cavity is housed in a vacuum system that is sealed from the environment, but not continuously pumped to keep it under vacuum. Since the spacer was constructed with Zerodur, it was not necessary to temperature stabilize the cavity, which would not be the case for Invar or SuperInvar. This is due to the low coefficient of thermal expansion which is 0.007 ppm/°C for Zerodur, compared to 0.35 ppm/°C for Super Invar and 1.2 ppm/°C for Invar.

Transmission through this optical cavity is monitored by a fast photodiode and transimpedance amplifier, and is side-of-the-fringe locked using the circuit found in Appendix A. This circuit feeds back to the PZT of the ECDL to keep the laser on resonance with the optical reference cavity. It is likely that this feedback actually broadens the laser's linewidth, but this doesn't appear to be a problem for repumping the barium ion.

To repump the $5D_{3/2}$ level of $^{138}Ba^{+}$ the unshifted beam passes through a mechanical shutter and is coupled into a PM optical fiber, to be combined with the 493 nm beam. At most, one can focus approximately 100 μW of this light onto the ion, which appears to

[2]This information is all encoded in the part number, PR1-650-98-1037-0.3CC.

[3]For full disclosure, we employed a DPAOM system for a while, but found it to be unnecessary

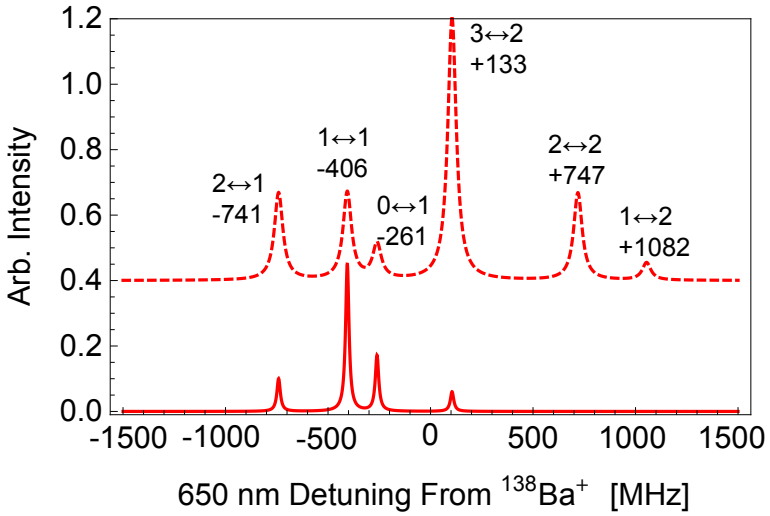

Figure 4.5: Absorption lines of the $5D_{3/2} \leftrightarrow 6P_{1/2}$ transition and 650 laser spectrum for $^{137}Ba^{+}$. The dashed plot shows the absorption features, with intentionally broadened features for clarity, as well as the total shift from the $^{138}Ba^{+}$ resonance. The amplitudes of the features are proportional to the relative strengths of each transition. The solid line shows the spectrum of the 650 nm laser with modulation, as well as relative laser power used to address each of the $5D_{3/2}$ hyperfine levels.

saturate the transition, resulting in unwanted ion heating. The beam is usually attenuated to approximately 10 μW.

To repump $^{137}Ba^{+}$, the situation is more complicated due to the hyperfine structure of both $5D_{3/2}$ and $6P_{1/2}$, as diagrammed in Figure 4.5. As it is, one needs to generate at least four different frequencies of radiation to repump out of the $F = 0, 1, 2, 3$ levels. We attempted to use a fiber-coupled broadband phase modulator to generate the necessary frequencies, but found it difficult to generate sufficient laser power at the desired frequencies without also having large intermodulation products. Additionally, the fiber modulator had insertion loss of approximately 7 dB at 650 nm. The combination of these two effects resulted in a low laser power with a messy spectrum.

Instead, we chose to split our beam into four paths and use double-passed AOMs to

frequency-shift three of the beams. These AOMs are driven at 167.5, 72.5, and 255.5 MHz generated by VCOs to produce light at -335, +145, and +511 MHz offsets from the carrier frequency once double-passed. The light from the four beams is then recombined into a single PM optical fiber using a series of PBS and 50/50 cubes and sent to the other table. The resulting frequencies and approximate powers can be found in Table 4.1, which are then combined with the 493 nm laser beam, to be sent to the ion as shown in Figure 4.1.

A suggested improvement to this system, if one is to trap $^{137}Ba^{+}$ would be to increase the amount of 650 nm radiation in the frequency shifted paths, by switching to custom AOMs that could offer better diffraction efficiency at the frequencies employed. It is unclear that the power used during my tenure was ever sufficient to saturate the $^{137}Ba^{+}$ transitions.

Table 4.1: 650 nm laser frequency shifts and beam powers. Using DPAOMs, additional frequencies of 650 nm light are generated. Due to low diffraction inefficiency in the AOMs at these frequencies, the intensity of the additional beams is reduced.

$5D_{3/2} \rightarrow 6P_{1/2}$ $F \rightarrow F'$	Offset from Carrier [MHz]	Max Power addressing the ion [μW]
$0 \rightarrow 1$	-335	5
$1 \rightarrow 1$	0	70
$2 \rightarrow 1$	+145	20
$3 \rightarrow 2$	+511	40

4.1.3 455 nm Laser

At the time that I started up in the lab, we were utilizing inexpensive Luxeon® Star LEDs to generate about a watt of light at both 455 and 614 nm for the shelving and deshelving processes, respectively. There were a few critical downsides to using these LEDs that culminated in our choice to replace them with lasers. First, the spectral half-width of both LEDs was approximately 20 nm, so one needed to use a narrowband interference filter to choose the correct frequency to address the ion. Secondly, it was difficult to achieve high

intensities of radiation at the ion, due to the large, finite size of the LED itself. This resulted in poor focus, so light scattered off of the trapping apparatus. Some of this scattered light was collected by the PMT, which wasn't a problem, but was irritating. The sum of these problems led to very long shelving and deshelving pulses, of approximately 500 ms each to achieve sufficient transition probability, which made data collection painstakingly slow (< 0.5 Hz experimental repetition rate).

Generating light at 455 nm was a bit of a conundrum when I started in the laboratory, aside from incoherent LEDs, as there were no laser diodes available that could produce the light directly. So, we bought a 910 nm diode, and machined a homebuilt external cavity in the Littrow configuration found in [59] and planned to employ a tapered amplifier / doubling cavity system to produce the light, akin to the 986 nm SHG system. While we got the 910 nm laser working, and were starting to double the light using the old bowtie cavity designed for 924 nm doubling, other students in our group stumbled upon a company that was making direct 450 nm direct diodes[4]. One of these diodes was a bit of a fluke, and happened to lase at approximately 455 nm. So, Spencer Williams removed the old grating for 910 nm light, and replaced it for one suitable for 455 nm and we were in business.

Since Spencer really took on this project, I'll leave it to him to really characterize the laser, as it has some interesting behavior. We generally drive it at high currents so that it is somewhat multimode. The benefit of this is that it does not need to be frequency stabilized to a reference cavity, and one does not need to generate sidebands to shelve $^{137}Ba^{+}$. We find that the laser will shelve the ion with nearly unit probability in < 10 ms running it in this way with a few tens of μW of light at the ion.

The ion is extremely sensitive to any of this leakage light, as it will result in accidental shelving events after absorption of only a few photons. For this reason, we employ a physical shutter identical to that used in the 650 nm laser system to ensure that the light is fully extinguished. As a result, the fastest we can fully open and close the shutter is approximately 8 ms. We found that even if one used a DPAOM as a shutter, with > 60 dB extinction ratio,

[4]The 450 nm light would be useful for a 3-photon photoionization setup, using 791 nm for the first transition, 450 nm for the 2nd transition, and then any of the cooling lasers would complete the ionization. One then does not need a UV source.

one would still watch the ion spontaneously shelve every few seconds, which was proving to be annoying to the user, so some additional measures to extinguish the light are necessary, if one wants to improve the time it takes to shelve the ion.

That being said, the system is quite reliable to use, and has an extremely simple beam path. Light from the Littrow laser passes through an optical isolator, and a HWP, then a PBS (to share with other experiments, or check the frequency on the wavemeter), and through the physical shutter. When the shutter is open, the light is coupled into an optical fiber. The output fiber is mounted to an XYZ translation stage, and focused onto the ion using an AR-coated doublet lens. The focus has a waist of approximately 100 μm, and scatter off of the trap rods seems minimal. We have observe no "ion destabilization" effects due to the shelving laser like that of the LED, as described in Section 3.5.

4.1.4 1228/614 nm Laser

For the reasons described in Section 4.1.3, we also wanted to replace the 614 nm LED with a laser. Again, the 614 nm light cannot be generated by a direct diode at the time of this manuscript, so it is necessary to frequency double 1228 nm light. I did not design, or plan this laser's construction, but made a few minor changes and moved the laser over to our laboratory. To the best of my knowledge, this laser was initially set up by an REU student, Andrea Katz, advised by Adam Kleczewski.

The 1228 nm light is generated by a Toptica DL100 system, with an AR-Coated laser diode. Since the diode is AR-coated the laser is less susceptible to mode-hopping than other lasers in the laboratory. After passing through an optical isolator approximately 30 mW of 1228 nm light is coupled into a waveguide PPLN SHG system, which is very efficient and does not require a build-up cavity to generate sufficient light. Approximately 100 μW of 614 nm light is generated in this way. A small fraction of this light is sent to the wavemeter to monitor the laser frequency. This allows for a very slow manual feedback, which is the only method used to keep the laser on resonance with the $5D_{5/2} \leftrightarrow 6P_{3/2}$ transition, as the laser is inherently stable, and quite resistant to slow drifts and mode-hops.

The remainder of the 614 nm beam is coupled into an optical fiber, and the output

of the fiber is combined with the 493 nm optical pumping beam using a dichroic mirror, and is then focused onto the ion as shown in Figure 4.1. Including all of the losses in the system from fiber coupling and combination with other beams, approximately 1 μW of light is incident on the ion. The light is extinguished with a homebuilt mechanical shutter to ensure that the ion remains shelved long enough for good state detection (approximately 20-50 ms, typically). The shutter is, again, not very fast, and attempting to generate a deshelving pulse of duration < 10 ms will cause the shutter to "misfire", and no light will pass through. A 10 ms pulse will deshelve the ion with high probability, and only requires that the laser is tuned within a few hundred MHz of the resonance frequency. The use of this laser is necessary to get the ion back in the cooling cycle quickly, but these long pulses do not limit the experimental repetition rate. Should one desire to reduce the duration of these pulses, one could use an AOM shutter instead.

4.1.5 2051 nm Laser

While all of the lasers discussed in this chapter are necessary to perform our experiments, the real bread-and-butter of our laboratory is the 2051 nm laser, and the vast majority of credit is due to Adam Kleczewski [33] and Jeff Sherman [66], for its conception and execution. I had just begun at the University of Washington when we really got the laser working, and started driving the first transitions in Ba^+. Much of this work is described in detail in [32, 33, 34], but we now know more about this laser's behavior than at the time of those publications. Since 2012, I've really not made any major changes to the setup, but was the first user to drive $6S_{1/2} \leftrightarrow 5D_{3/2}$ transitions in $^{137}Ba^+$. In this section, I'll summarize how the laser is frequency stabilized to the ULE-spaced high-finesse reference cavity, as well as our best knowledge of the laser's linewidth.

The 2051 nm light is generated by a TmHo:YLF diode pumped solid state laser (DPSS) manufactured by CLR Photonics, which is now a part of Lockheed Martin. This wavelength is deemed 'eye-safe', so these lasers are frequently used in LIDAR applications [41]. Coarse tuning of the laser frequency is achieved by tuning the temperature of the resonator, but this is *very* slow. One can provide faster ($\simeq$ 10 kHz small-signal bandwidth), fine feedback to a

piezoelectric stack, like in an ECDL, however, there is no easy access to the pump current in this DPSS laser, which could provide additional frequency tuning. The manufacturer specified linewidth of the laser is 10 kHz with slow drifts on the order of 1 GHz over a twenty-four hour period. The maximum output power of the laser was measured to be approximately 40 mW at 2051 nm.

At the time of construction, it was decided to frequency double the 2051 nm light to 1025 nm to frequency stabilize the laser, for a number of reasons. The first is that at the time, the state-of-the-art high reflectivity optical coating technology limited cavity finesses to ∼20,000 at 2051 nm, which has improved to be approximately 100,000 as of 2011. At 1025 nm, however, the finesse could be much higher. In fact, the finesse of our ULE spaced cavity is in excess of 300,000, as measured by cavity ring down [5, 34]. Additionally, the necessary electro-optics at 2 μm are more expensive, and less available.

The frequency doubling and stabilization schematic can be found in Figure 4.6, and will be briefly summarized here. The 1025 nm light is generated in a 'bow-tie' cavity with a custom AR-coated PPLN crystal to perform the SHG. This 'bow-tie' cavity is locked to the cavity resonance using the Hansch-Couillaud locking scheme [25] similar to the 986 nm SHG system in Section 4.1.1, and generates approximately 150 μW of 1025 nm light.

This light is frequency shifted using a DPAOM setup, using an AOM with center frequency of 200 MHz, and bandwidth of approximately ±30MHz. This will serve to give us ultimately 60 MHz of laser frequency tuning at the ion. This upshifted light is then coupled into the high finesse ULE-spaced cavity, which has a free spectral range of $\simeq$ 1935 MHz, and is of the design found in [52]. The cavity resonances have FWHM of approximately 6 kHz, so if we stabilize to the top 1% of the cavity feature, this should result in a laser linewidth less than a few hundred Hz. We do not have another source at 2051 nm to compare to, so the ion is our only tool to study the laser's linewidth, which we did in [34].

We demonstrated that the laser has a linewidth less than 500 Hz, as we observed the ion's coherence time to be 3.2 ms on the $6S_{1/2}, m = -1/2 \leftrightarrow 5D_{3/2}, m = -3/2$ transition in $^{138}Ba^{+}$. This coherence time was reported to be consistent with drifts in ambient magnetic fields, so the measured linewidth represents magnetic field noise, and the true linewidth of the laser must be lower. There is one other measurement, that we have done, using

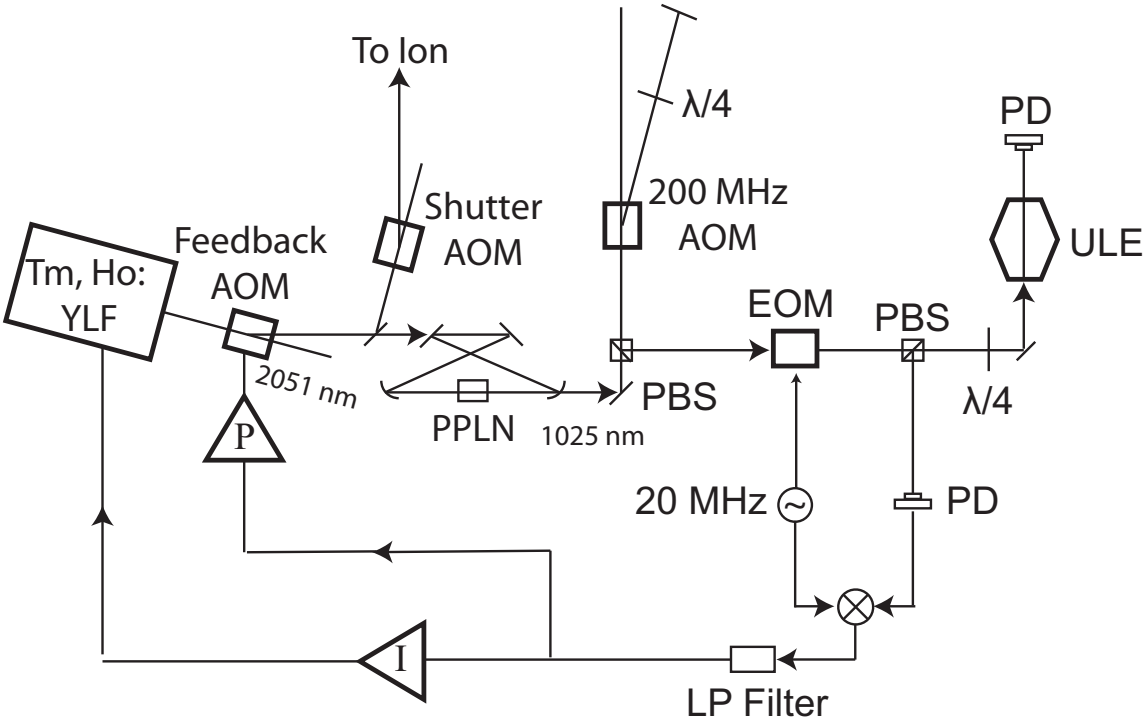

Figure 4.6: Tm,Ho:YLF laser stabilization schematic. Light from the 2051 nm Tm,Ho:YLF laser passes through an AOM and is frequency doubled with a PPLN crystal in a 'bow-tie' cavity configuration. The 1025 nm light is then frequency shifted by a DPAOM, and sent to the ULE spaced cavity as in a PDH scheme [16]. An EOM driven by a 20 MHz oscillator is used to generate the sidebands necessary for frequency stabilization. After passing through a low-pass (LP) filter to remove the 20 MHz modulation, high bandwidth proportional feedback (P) is sent to the feedback AOM, while low bandwidth integral feedback (I) is amplified and fed to the tuning piezo inside the laser head.

the method described in [50], that demonstrates a laser linewidth of approximately 5 Hz, which will be described in Section 5.2. If one were to implement a frequency comb in the laboratory, it would be easy to make a direct measurement of the laser linewidth and absolute frequency, as discussed in [10] and other sources.

The fraction of the beam (approximately 5 mW) that is not used for frequency doubling and stabilization is sent through a Brimrose AOM driven at 55 MHz, which serves as both a shutter, and a means to perform ARP sweeps. Its frequency is generated by an HP8657D synthesizer which has DC frequency modulation (DCFM). Sweeping the DC modulation voltage from -1V to +1V allows for a maximal frequency sweep rate of 400 kHz in 2 ms. The deflected beam passes through a polarizer and custom half-waveplate, to produce nearly linear polarization, which is aligned onto the ion at approximately 90° to the quantization axis. This beam incident on the ion is not perfectly linearly polarized as described in [80], so we are working to reduce polarization effects caused by birefringence in the viewport window. Ultimately, a few mW of tunable 2051 nm light addresses the ion, producing Rabi frequencies on the order of $\Omega \simeq 2\pi \times 10$ kHz. Our choice of orientation allows one to drive the $\Delta m = \pm 2, 0$ transitions depending on the polarization angle relative to the quantization axis, as shown in Figure 2.6.

Using this laser while frequency stabilized to the ULE spaced cavity has a complication, namely that we can only tune the laser 60 MHz out of the total free spectral range of 2 GHz by simply tuning the frequency of the DPAOM frequency shifter. At the time of this publication, one can frequency stabilize the laser to a TEM_{00} mode of the ULE cavity and drive all allowed transitions in $^{138}\mathrm{Ba}^{+}$ at magnetic fields below 5 G. One can additionally tune the laser by three free spectral ranges to be within the DPAOM bandwidth of the $6S_{1/2}, F = 2 \leftrightarrow 5D_{3/2}, F = 2$ transitions. At the moment, the other transitions from $6S_{1/2}, F = 2 \leftrightarrow 5D_{3/2}, F = 0, 1, 3$, are not accessible without making changes to equipment (for example, flipping the orientation of the DPAOM to use the downshifted beam instead of the upshifted beam currently used). As Adam Kleczewski describes [33], there is good coverage of the 2051 nm laser frequency space (1.8 GHz out of a total 1.934 GHz), by making various changes to the laser setup.

4.1.6 Photoionization Lasers at 791 nm and 337 nm

The 791 nm laser is a homebuilt ECDL with a design similar to that of the 455 nm laser described in 4.1.3. Drifts in the frequency are prevented by a side-of-the-fringe lock to a Super-Invar spaced optical reference cavity that is temperature stabilized. The circuit used to lock the frequency is a descendent of that found in Appendix A, and the performance of the temperature stabilization can be found in [51].

The laser running at 337 nm is a Laser Science inc. VSL-337-NDS N_2 laser. It outputs approximately 400 μJ per pulse or 6mW average power when pulsing at a high rate; we typically run at < 10 Hz. The lasers emits a single pulse with each TTL signal sent from the DAQ. The spatial mode of the laser is a rectangle with a square taken out of the upper right corner for many of the N_2 laser in our laboratories. As such, it is difficult to focus the beam tightly through the trap.

The 791 nm laser beam and the 337 nm laser beams are made to propagate parallel to each other, using a D-shaped mirror. Using a UV grade fused silica lens, the 791 nm light is focused tightly through the center of the trap, and the 337 nm is focused enough to not clip the trap rods, but still large enough spot size to ensure spatial overlap of both photoionization beams near the center of the trap. Loading rates of $^{138}Ba^+$ as a function of frequency of the 791 nm laser's frequency reported by the wavemeter can be found in Figure 4.7. This data was taken when the 791 nm laser was oriented at 45° to the Ba flux from the oven, so a Doppler shift of ~ 250 MHz is observed. The loading rate of $^{138}Ba^+$ can be slowed down by pulsing the N_2 laser more slowly (~ 1 Hz), or by decreasing the oven current so that single $^{138}Ba^+$ ions are loaded frequently. This usually only takes a few minutes.

To load $^{137}Ba^+$ it is necessary to detune the laser from the $^{138}Ba^+$ transition frequency. Due to the fact that ^{138}Ba is seven times more abundant than ^{137}Ba, the loading rate is naturally lower for the latter, so a measurement like in Figure 4.7 has not been performed. Instead, the necessary shift from the ^{138}Ba transition has been calculated from the results of [12], and are tabulated in Table 4.2. It is easiest to use the $F = 3/2 \leftrightarrow F' = 3/2$ transition, as it is easy to shift from ^{138}Ba to ^{137}Ba, but the strongest transition is $F = 3/2 \leftrightarrow F' = 5/2$.

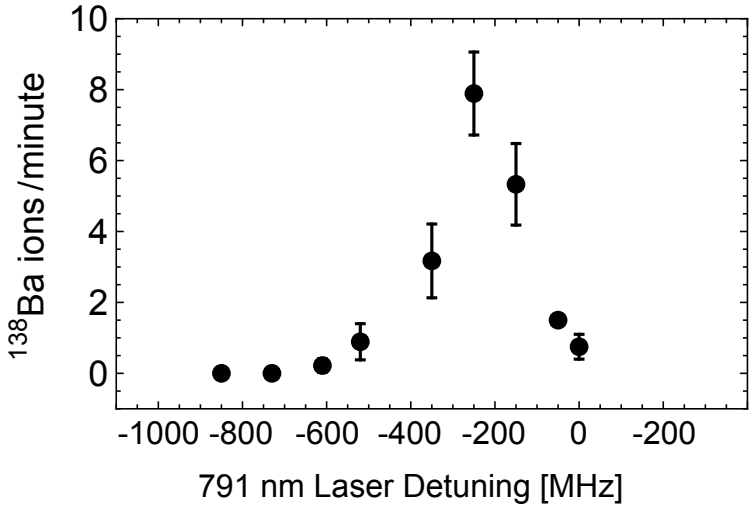

Figure 4.7: Loading rates of $^{138}Ba^{+}$ with Doppler effect. Ions were loaded with the N_2 laser pulsing at 10 Hz. The x-axis is the detuning from the optimal laser frequency measured by the wavemeter for the other experiments in the laboratory where the 791 nm laser $\boldsymbol{k}$-vector is orthogonal to the barium flux. Thus we observe a shift of approximately 250 MHz, and broadening due to the Doppler effect. This shift has been eliminated in a new version of the trapping apparatus.

Table 4.2: Isotope and Hyperfine Shifts for the 791 nm laser transitions for ^{137}Ba from the ^{138}Ba transition. The isotope shift for all of the transitions between hyperfine levels was measured in [24], while the hyperfine structure was reported in [12]. These can be summed to find the total shift for a transition in ^{137}Ba compared to ^{138}Ba, computed in the last column.

$6s^2(^1S_0) \leftrightarrow 6s6p(^3P_1)$ $F \leftrightarrow F'$	$\Delta\nu_{\text{iso.}}$ [MHz]	$\Delta\nu_{\text{HFS}}$ [MHz]	$\Delta\nu_{\text{Total}}$ [MHz]
$3/2 \leftrightarrow 5/2$	183.4(1)	1715.48(6)	1899(1)
$3/2 \leftrightarrow 3/2$	183.4(1)	-1108.98(3)	-925(1)
$3/2 \leftrightarrow 1/2$	183.4(1)	-2928.49(6)	-2745(1)

Aside from the side-of-the-fringe lock to the cavity, the 791 nm laser is only referenced to the wavemeter, which has shown susceptibility to drifts due to the ambient atmospheric pressure and humidity. While we could reference the wavemeter to a stabilized HeNe or other laser, it may be beneficial to build a saturated absorption spectroscopy system to lock the 791 nm to the atomic transitions themselves. This would remove uncertainty in the wavemeter's accuracy and allow for very simple switching between any Ba isotopes.

4.2 Radio-frequency Sources

For both the Landé-g_J factor measurement of ^{138}Ba$^+$(Chapter 6), as well as the hyperfine spectroscopy of ^{137}Ba$^+$ $5D_{3/2}$ (Chapter 7), it is necessary to perform magnetic dipole transitions, which requires oscillating magnetic fields at rf frequencies from $\sim$ 1 MHz to $\sim$ 650 MHz. This section will describe how we generate these magnetic fields.

For all of the spectroscopy, we employ an HP8656B frequency synthesizer, which can output rf signals from 0.1 to 990 MHz signals. It is computer controlled by our data acquisition system via HP-IB interface, the original version of GPIB, which allows us to control the frequency and amplitude of the signal. One drawback is that the settling time for

changing the frequency or amplitude is quite slow (hundreds of ms) on an experimental time scale, as shown in Figure 4.8. This necessitates picking a single frequency and amplitude, and using it for many trials in a row, then changing the settings once, using those settings for many runs, and repeating.

The HP8657B synthesizer is disciplined by a Symmetricom 5071A primary Cs frequency standard via a 10 MHz reference sine wave output. The frequency standard has manufacturer quoted accuracy of $\pm 1 \times 10^{-12}$, and stability of $\leq 1.2 \times 10^{-11}$ at 1 Hz in standard performance mode. By referencing the 8657B synthesizer to the standard, we ensure that the frequency output is both free from drift, and absolutely accurate with traceability to NIST.

The sinusoidal output of the 8657B synthesizer is switched by a MiniCircuits absorptive SPDT switch that has in-out isolation in excess of 75 dB in the "off" state between DC and 1000 MHz, ensuring that when the source is off. This switch also has a fast rise/fall time (10%-90%) of at most 15 ns, producing square pulses in our experiments. From the output of the switch, this rf signal is amplified, passed through a DC block to ensure that no DC current flows, and dropped over a 50 Ω rf resistor, which is connected to a dedicated rf electrode in the trap and then grounded. These steps are necessary so that there is minimal oscillating voltage which could perturb the ion, but a sizable rf current is flowing through the dedicated spin flip electrode.

This rf current then generates a oscillating magnetic field that addresses the ion. The electrode runs parallel to the trap axis several millimeters away from the trap center, producing a magnetic field oriented close to 45° to the quantization axis allowing us to drive $\Delta m_{J,F} = 0, \pm 1$ transitions.

When we are attempting to drive multiple transitions at very different frequencies in a single experiment, it is necessary to use a second synthesizer to alleviate these slow frequency and amplitude switching times. For this, we use a MiniCircuits SSG-6000 borrowed from Prof. Alejandro Garcia's group, which is also referenced to the same Cs frequency standard as the 8656B. We can switch between these two sources using an additional MiniCircuits SPDT switch, to choose which source generates the oscillating magnetic field at the site of the ion.

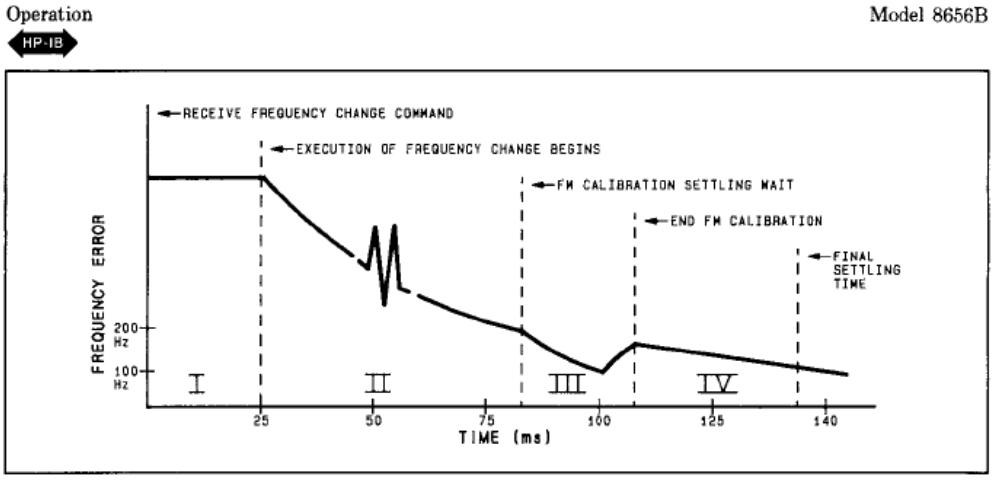

Figure 4.8: Frequency switching characteristics of HP 8656 B synthesizer. Upon changing the frequency, it takes hundreds of ms for the synthesizer to stabilize to the Hz level necessary for high precision spectroscopy. This figure is reproduced from the 8656B user manual.

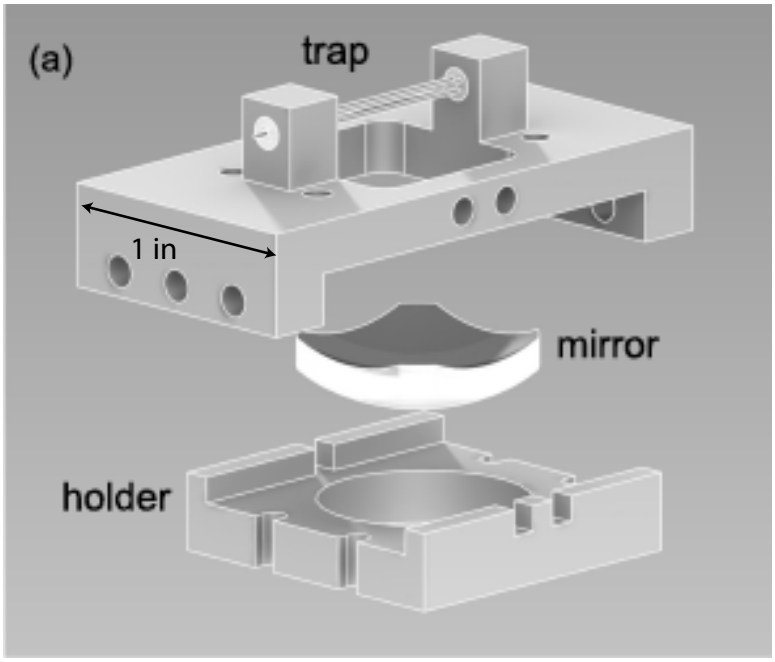

Figure 4.9: Exploded view of the ion trap with spherical mirror. This trap was designed and made by Gang "Rick" Shu, to include a spherical mirror below the trapping electrodes. The distance between trap rods is approximately 1 mm. This figure is reproduced from [68].

4.3 The Linear Paul Trap and Support Apparatus

The ion trap used throughout all of these experiments was the trap described in [68] that previously had a spherical mirror installed under the trapping electrodes to enhance collection of photons emitted by the barium ion. The former design is found in Figure 4.9 reproduced from [68]. This trap was used unmodified from early 2010 to late 2012 in our laboratory. However, it was necessary to break vacuum to make a few modifications to this design to reduce significant ac-Zeeman effects that were observed, and improve optical access to the ion. The details of these upgrades will be briefly summarized in this section.

4.3.1 Modifications to Trapping Apparatus and Electrodes

In the original design, both ends of the trap rods were connected to electrical feedthroughs, which had a few advantages. First, one could run high current through the trap rods to evaporate deposited barium. Additionally, one could flow rf current *through* the trap rods to achieve very quick ground state Zeeman Rabi flops (sending 1.5 W of resonant rf resulted in $t_\pi = 0.6$ μs). Unfortunately, we suspect that the way these rods were connected resulted in closed loops that could cause oscillating currents at the trap rf drive frequency, resulting in large oscillating magnetic fields at the trapped ion's position.

To correct this, we broke these connections so that each rod was only connected on a single end, so that less current would be induced. We also decided that it would be valuable to add dedicated micromotion compensation electrodes in the form of a plate (in a similar place to where the mirror was held in place in Figure 4.9) for vertical compensation, and a rod running close to parallel to the trap to provide horizontal compensation. Again, these were connected in a way that prevents closed loops from being formed.

Additionally, we added a dedicated spin flip electrode to create oscillating magnetic fields at the ion, that would not require any difficult impedance matching since we knew that we would be often changing the frequency of these fields from a few MHz to several hundred MHz. Finally, we decided to do away with some of the electrical feed-throughs found in the original trap, to replace them with viewports. This would allow additional laser access running perpendicular to the trap axis. Sending 2051 nm light through this port could, for example, allow one to observe longer coherence times as the light would be decoupled from the axial motion of the ion in the trap. The result of this work is shown schematically in Figure 4.10, but does not show the additional electrodes.

The final upgrade in this system involves the placement of the barium oven. In the old trap, it was located such that the hot Ba flux was oriented at 45° to the 791 nm photoionization laser beam. A four-pin electrode electrical feedthrough with a Ba oven has been added below the trap now, (out of the page in Figure 4.10), so that the Doppler shift and broadening have been minimized.

To conclude this section, I report typical trapping voltages, and the resulting secular

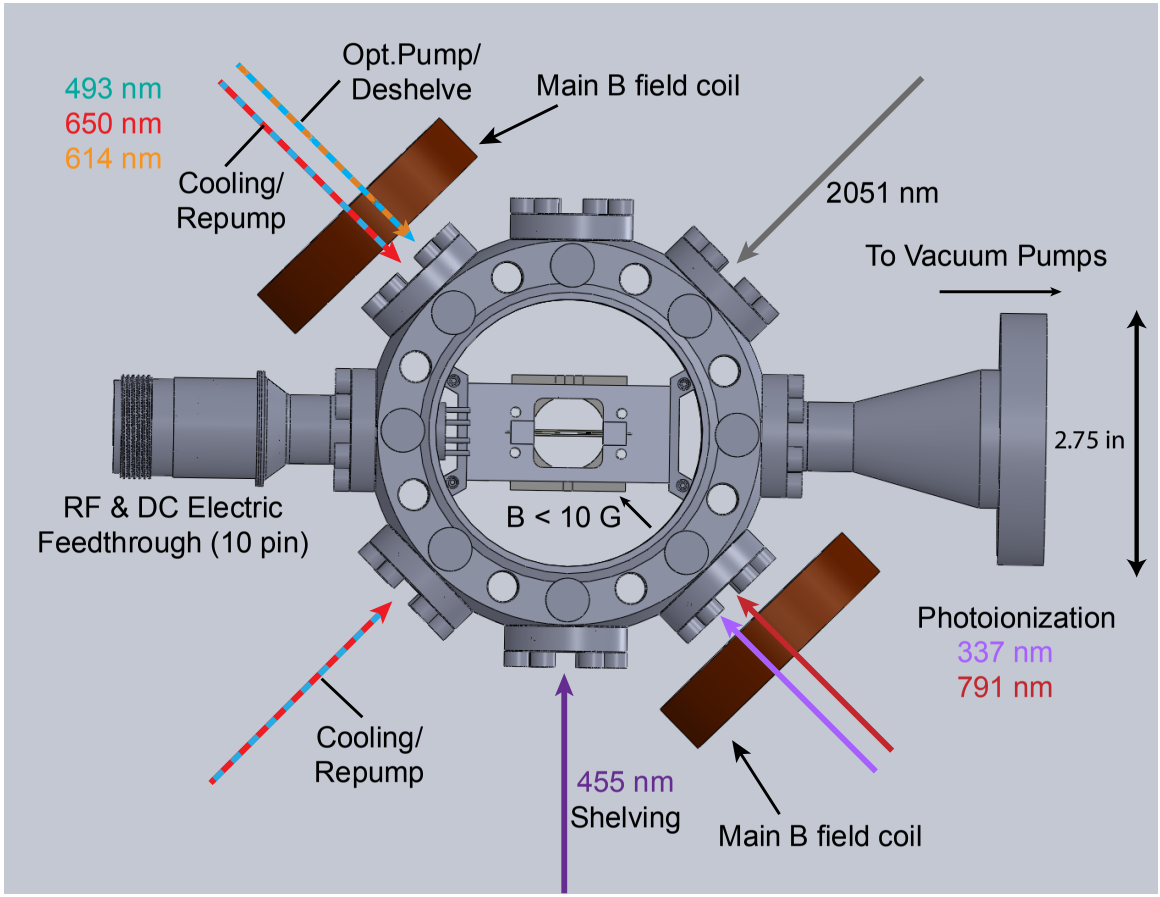

Figure 4.10: Top view of trap with laser access shown. All lasers are focused onto the ion held at the center of the linear Paul trap. The magnetic field coils (shown in red) provide a quantization axis with a field of 10 G or below oriented as shown. This configuration of lasers was that used when the hyperfine spectroscopy measurement was performed.

frequencies. The rf drive is typically between 0.5 and 2.5 W, at approximately 12 MHz, to a resonator with quality factor, Q$\sim$ 200. For a single barium ion, 1 W forward produces radial secular frequencies of about 870 kHz, and $\simeq$ 0.75 W results in 600 kHz frequencies. The endcap are typically at 25 V, which results in an axial secular frequency of approximately 440 kHz. Horizontal micromotion is compensated with $\sim$ 400 V applied to the rod electrode, and vertical micromotion is compensated with $\sim$ 60 V applied to the plate.

The vacuum system is largely unmodified from the previous version. Attached to the main trapping chamber are the vacuum pumps to achieve UHV as shown in Figure 4.11. This includes a titanium sublimation pump and a 20 L/s ion pump, with an ion gauge to measure the pressure. The trap was sealed with an all-metal bakeable valve after a 10 day bake at a temperature of approximately 190 °C, resulting in a pressure of approximately 4×10^{-10} Torr. There may be a small leak or a virtual leak that is preventing us from reaching lower pressures, with evidenced by the observation that the pressure slowly creeps from 4×10^{-10} Torr up to 6×10^{-10} Torr over a period of about two weeks. The reasons for this leak are unclear, but might be due to a poor seal on the all-metal bakeable valve. It may be necessary to replace the gasket of this valve, but for now, flashing the titanium sublimation pump by running 40 A of current through its filaments for 60 s will bring this pressure back down.

4.3.2 Photon Collection System

Photons emitted from the barium ion are collected by a long working distance Mitutoyo 10x microscope objective with numerical aperture of 0.28 approximately 30 mm above the ion that collects approximately 2% of the total fluorescence. This light is refocused through a pinhole, which serves as a spatial filter to reject stray light caused by room lights and scatter off of the viewports. The collected light is spectrally filtered by a custom 493 nm narrow band interference filter to prevent other frequencies from reaching the PMT. Using a motorized flipper mirror, we can choose whether the collected light is imaged on either a Hamamatsu PMT or an Andor iXon+ EMCCD camera.

Using knowledge of the axial trap frequency ($\omega_{\text{axial}} = 2\pi \times 390$ kHz), we can find the

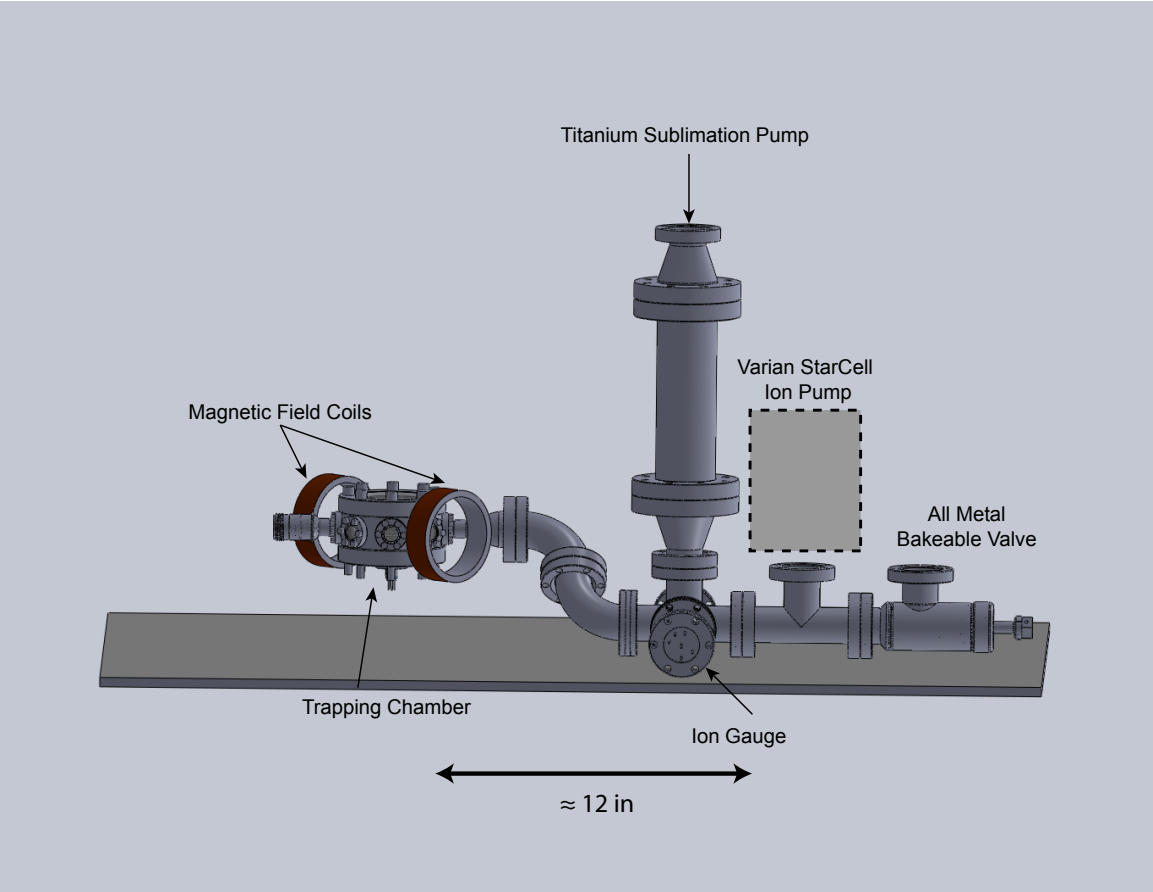

Figure 4.11: Ion trap vacuum chamber with UHV pumping system. Pressure is maintained at approximately 4×10^{-10} Torr as read by the ion gauge with the ion pump continuously running and bi-weekly "flashes" of the titanium sublimation pump. Ion fluorescence is collected through a viewport on the top of the trapping chamber.

separation between a pair of ions by balancing the trap's restoration force,

$$F_{\text{restore}} = m\omega_{\text{axial}}^2 x, \tag{4.1}$$

and the Coulomb repulsion

$$F_{\text{c}} = \frac{1}{4\pi\epsilon_0}\frac{q^2}{(2x)^2}, \tag{4.2}$$

where x is the distance from the center of the trap. Plugging in numbers for the charge (1 e) and mass (138 AMU), we find that $x = 3.5$ μm, so the separation between a pair of ions is 7.0 μm. On our CCD camera, we observe the ions to be spaced by 62 pixels, with a square pixel size of 16 μm as quoted by the manufacturer, so the magnification of our imaging system is approximately 140. We observe a slight coma on our ions as shown in Figure 4.12[5], which is believed to be due slight misalignment of the optics in the photon collection system but this plays no role in our experiment.

4.3.3 Future Upgrade - Magnetic Shielding

It make sense at this point to address the future need for magnetic shielding surrounding the ion trap to shield the ion from fast fluctuations and slow drifts of the ambient magnetic field in the laboratory. But first, let us motivate the need for the upgrade by describing the current state of the situation. In early 2013, Tom Noel and I observed that the magnetic field wasn't constant at the site of the ion run to run when we were doing rf spectroscopy of $6S_{1/2}$ and $5D_{5/2}$ Zeeman structure, but these were slow measurements taking at least a few minutes. I spoke to members of the EDM group, and they said that the King County Metro Transit system electric buses produced large magnetic fields whenever a bus driver would press the accelerator of the electric buses. This is because the currents would flow along the overhead wires, that were not balanced. Wanting to observe this for myself, I borrowed a fluxgate magnetometer from the the gravity group, and set it up near the ion trap overnight. The dramatic results can be found in Figure 4.13.

We observed vertical magnetic field fluctuations on the order of 10 mG that lasted on the order of 10-30 s and were relatively unpredictable. Since the bus line runs multiple

[5]This image was taken on with different endcap voltages, and thus a different axial secular frequency resulting in a separation of 11 μm.

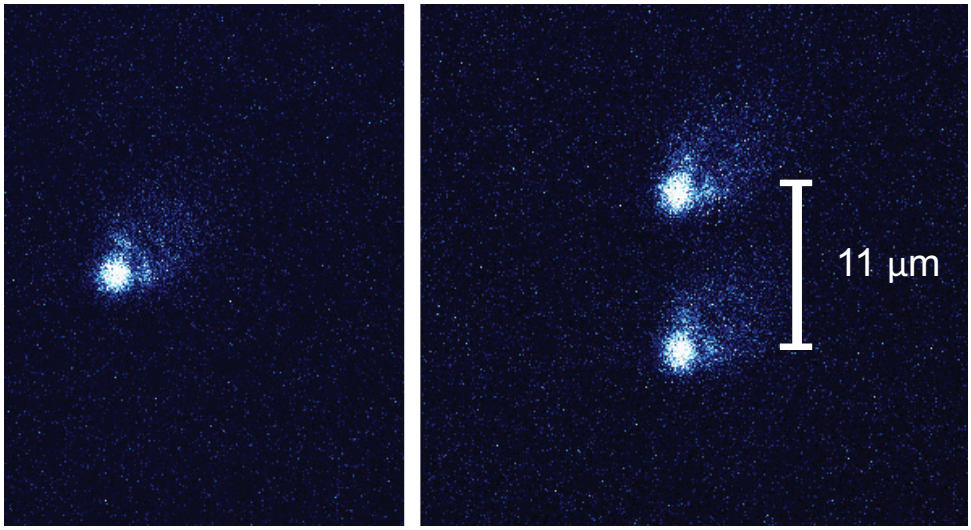

Figure 4.12: False-color images of a laser-cooled single $^{138}Ba^{+}$ (left panel) and a double (right panel) imaged by collected fluorescence at 493 nm on the EMCCD camera. These images were taken minutes apart with continuous loading. Upon loading, a second ion displaces the pair from the center of the trap. The pair of ions are separated by 100 pixels, and thus 11 μm in the vacuum chamber on this day. The coma that extends up and to the right arises because the imaging axis is slightly tilted, and causes no effect on our experiment.

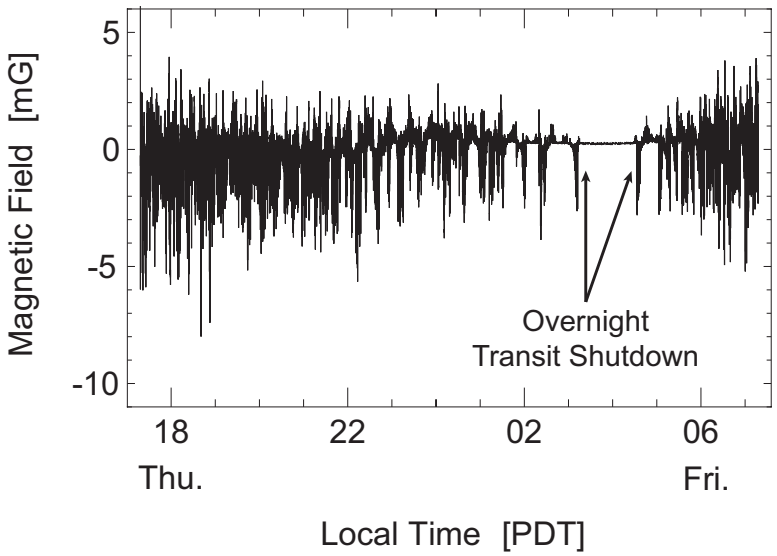

Figure 4.13: Observed magnetic field fluctuations in the vertical direction in the laboratory on March 20-21, 2013, measured with a fluxgate magnetometer in 2 s intervals. The transit system was responsible for fast magnetic field fluctuations on the order of 10 mG. The stabile region from 3:15 AM PDT to 4:30 AM concides with the nightly transit system shutdown.

buses at a time, these fluctuations are convolved because buses operate in both directions and draw current. The data found in Figure 4.13 started during rush hour at approximately 5:30 PM, and continued until 8 AM the following day. The smoking gun in all of this was the remarkably quiet period between 3:15 AM and 4:30 AM, when the transit system runs no buses. During this time, the field was quiet to 20 μG.

I contacted the city, and found out that they were in process of fixing these unbalanced currents. But for the mean time the only way to take data would be on weekends when the city would be running gas buses, which is exactly what I did for the Landé-g_J experiment. This made it immediately obvious that to use the experiment effectively, we would need to have passive μ-metal magnetic shielding surrounding our ion trap.

This was a relatively constrained problem, since we require optical access from six directions, and electrical feedthroughs on the bottom and side, and the ability to pump down on the trap from the side. Additionally, with the magnetic dipole transition moment measurement in mind, we knew we would want to be able to precisely rotate the orientation of the magnetic field. The final design can be found in exploded view in Figure 4.14 and semi-transparent surrounding the ion trap in Figure 4.15.

One of the most notable features of the shield are the "stove-pipes" that were recommend by Professor Blayne Heckel. Addition of this small amount of material allows for significant enhancement of shielding, when a cutout is required. Doing finite-element analysis, it is predicted that this shield will reduce slow fluctuations and drifts by a factor of a few hundred in the vertical direction, and approximately 100 in the horizontal direction.

After we had ordered the shielding from Amuneal in June 2013, I later learned that the repairs to the transit system had been completed, and that the magnetic field was significantly quieter. To quantify the change in our laboratory, I let the fluxgate magnetometer run again overnight, with the results in Figure 4.16. Since the field was much quieter, it was assumed that it was not necessary to deploy the shielding on the trap for the duration of the nuclear magnetic octupole experiment. However, as will be discussed in Chapter 7, the shielding may indeed have proved useful. Installing the shielding certainly makes certain things, such as coarsley aligning a laser beam through the center of the trap, more difficult, but will ultimately be necessary for all future experiments. It is my hope that this shield

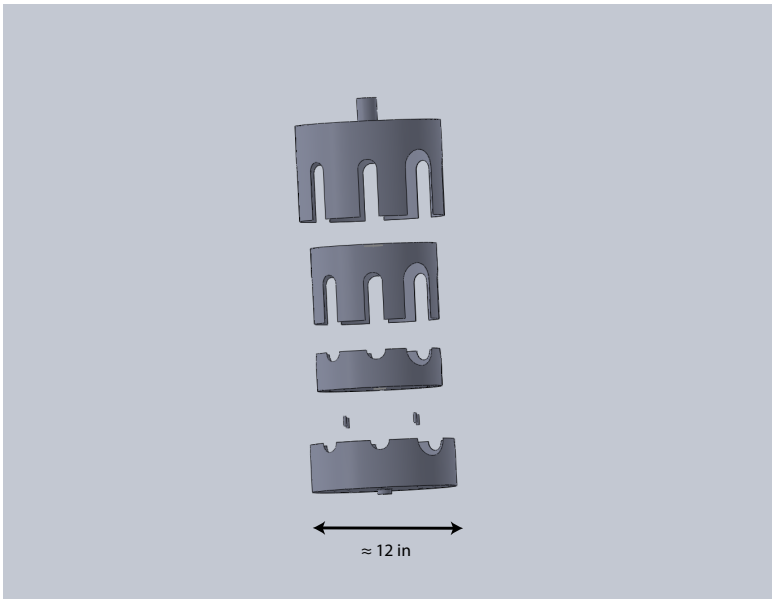

Figure 4.14: Exploded view of magnetic shield assembly. Two layer shielding is designed to reduce magnetic field fluctuations without losing optical or electrical access to the ion trapping chamber. The shield is designed to press fit together with minimal deformation.

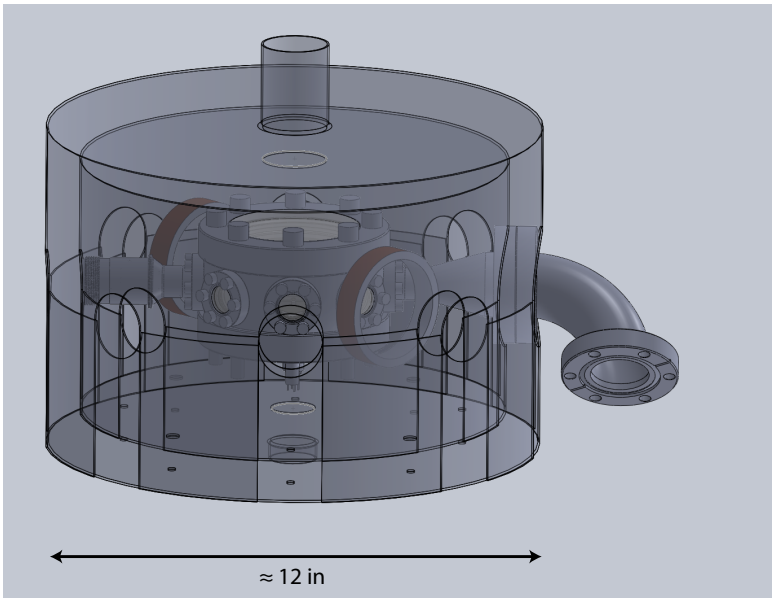

Figure 4.15: Semi-transparent view of shielding installed on ion trap.

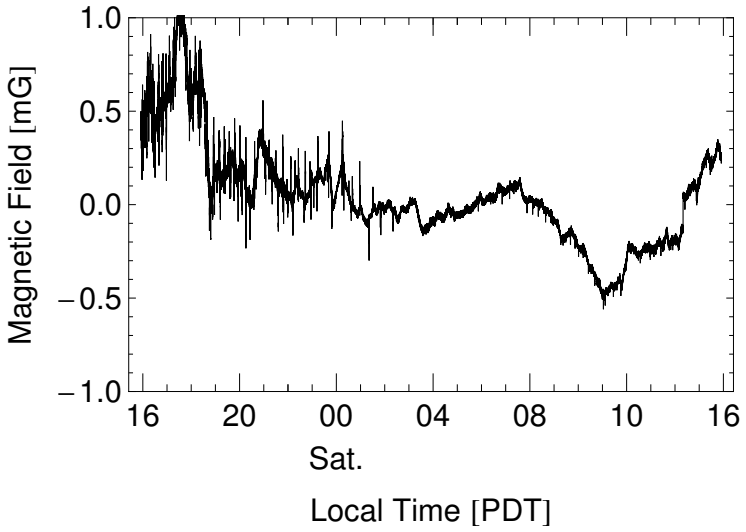

Figure 4.16: Observed magnetic field fluctuations in laboratory after transit repair. Measured with a fluxgate magnetometer in 2 s intervals started on Friday, June 21, 2013, the magnetic field is noticeably quieter, enabling one to take data during the day during the week. Note that the vertical scale is reduced by a factor of 10 from Figure 4.13.

can follow future trap redesigns, and provide stable magnetic fields for years to come.

Chapter 5

ION DECOHERENCE MEASUREMENTS WITH THE 2051 NM LASER

Before we dive into the measurements of Ba^+ atomic structure, it would be worthwhile to go through a pair of quick measurements that we did to assess the temperature of a laser-cooled $^{138}Ba^+$ as well as a measurement of the 2051 nm laser's linewidth. We'll go through the assumptions used to reach these conclusions, and briefly describe the measurements. One should really consider these efforts to be diagnostics of our entire trapping/cooling apparatus, and the 2051 nm laser itself.

5.1 Measurement of the temperature of laser cooled $^{138}Ba^+$

We go to great pains to ensure that our ion is Doppler cooled well, and constantly fiddle with the 493 nm and 650 nm laser beam power and frequency. Most often we just look at the image of the ion on the EMCCD camera, and look for a couple of features that could be symptomatic of a hot ion. If the ion is quite cold, it resembles a point source, and will produce a characteristic Airy Disc image on the camera. Should we find the ion to be 'hot', it will look 'fuzzy' on the camera. If the ion is being cooled really poorly, it will actually show evidence of visibly oscillating in the trap with an amplitude of a few microns. It's possible to improve the ion's stability in the trap by eliminating these symptoms, but once this is done, is the ion at the Doppler limited temperature? Ten times the Doppler limit? A hundred?

To determine the temperature, we are going to preform a Rabi oscillation experiment with as fast a Rabi frequency as possible. This discussion will follow the treatment found in [60], so I won't go into the derivation the formulae . The procedure we used is as follows, and assumes that one has already found the resonance frequency of a $6S_{1/2} \leftrightarrow 5D_{3/2}$ transition.

(a) Doppler cool the ion on the 493 nm and 650 nm transitions, and extinguish the primary

493 nm cooling beam.

(b) Optically pump to one of the ground state Zeeman sublevels, using the secondary, circular-polarized 493 nm beam.

(c) Extinguish all of the lasers.

(d) Expose the ion to a square pulse of resonant 2051 nm light of fixed duration, t

(e) Turn on the 455 nm beam, so that if the ion was in $6S_{1/2}$, it will be shelved 89% of the time, and if it was in the $5D_{3/2}$ level, it will remain there.

(f) Turn on the cooling beams and record if the ion is 'bright' or 'dark'.

(g) Deshelve if necessary to return to the cooling cycle.

(h) Vary the 2051 nm pulse duration.

(i) Repeat steps (a-h) many times at each pulse duration to accumulate statistics (100 times in this case). The full, automated experiment takes approximately an hour, but requires minimal oversight.

The resulting plot shows the probability of finding the ion to be 'dark' as a function of the 2051 nm laser's exposure time in Figure 5.1, where Rabi oscillations as described by Eq. 2.46. This function does not account for a source of decoherence, which is readily observed in the data. The source of this decay can be due to a number of sources including laser linewidth, laser drift from resonance, magnetic field drifts, and ion temperature. The way the experiment is performed rules out laser drift from resonance, and magnetic field drifts, because each of these effects would result in a reduction of contrast independent of pulse duration. If we reduce the intensity of the laser source, we observe a longer coherence time, indicating that the laser's linewidth is not the limiting factor for the data in Figure 5.1. Thus, the mechanism of decoherence is due to the ion's temperature, supported by evidence that the coherence time is dependent on the Rabi frequency from similar experiments.

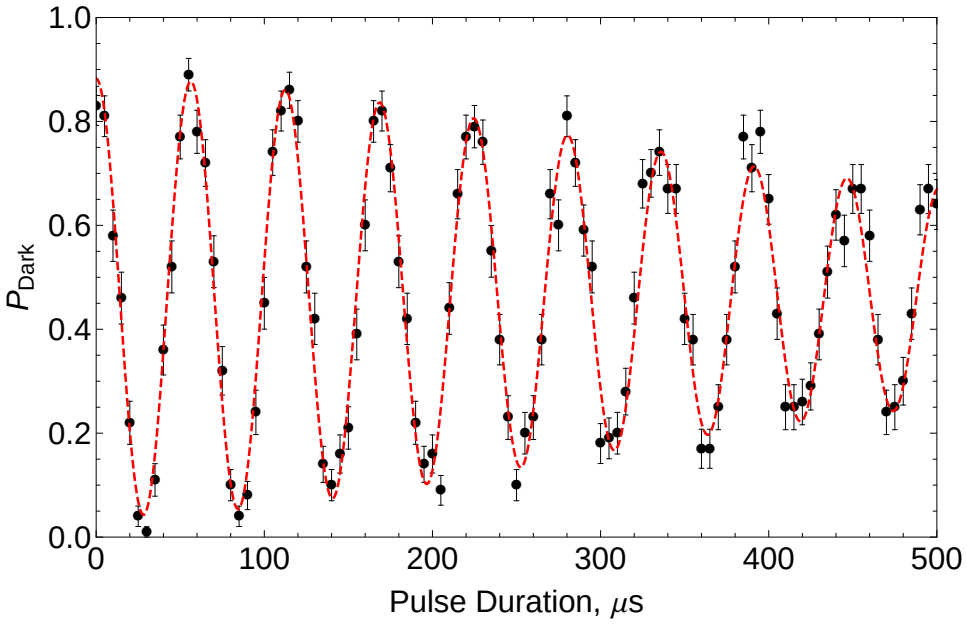

Figure 5.1: Rabi oscillation using the 2051 nm laser with decoherence due to finite ion temperature. The probability of finding a 'dark' ion is plotted against the pulse duration of the resonant 2051 nm radiation. Each pulse duration is attempted in succession, and then the whole sequence is repeated 100 times to accumulate statistics. The red, dashed line shows the least-squares fit accounting for the finite ion temperature as discussed in the body of the text. The reduced χ^2 of the fit is 1.90 for the 4-parameter fit.

This analysis relies upon the fact that the Rabi frequency, Ω is a function of n, the occupation number of the ion's quantized motion in a harmonic potential due to its finite temperature. The weakest trap direction will have the lowest secular frequency and thus the highest average occupation number, $\bar{n}$ following the equipartition theorem. We have made the assumption that only the weakest trap direction contributes to the decoherence. In our trap, this is the axial frequency, ω_{axial}. Since we are on resonance with the 'carrier' of the transition, we do not change the occupation number when we drive the $6S_{1/2} \leftrightarrow 5D_{3/2}$ transition. The Rabi frequency of the n-th transition is modified by

$$\Omega_n = \Omega_0 L(n, \eta^2), \tag{5.1}$$

where Ω_0 would be the Rabi frequency for an ion in the ground state of the harmonic potential, $n = 0$, and η is the Lamb-Dicke parameter, which we will define shortly. The function that modifies Ω_0 is the n-th order Laguerre polynomial, approximated by

$$L(n, \eta^2) = 1 - \eta^2 n + \frac{1}{4}\eta^4 n(n-1) + ... \tag{5.2}$$

which we will truncate at the third term because the Lamb-Dicke parameter, $\eta \ll 1$. Finally, there is a weighting factor for the n-th Rabi frequency, which for a thermal state is given by:

$$w(n, \bar{n}) = \frac{1}{\bar{n}+1}\left(\frac{\bar{n}}{\bar{n}+1}\right)^n. \tag{5.3}$$

So, the probability of finding a dark ion in our experiment is described using:

$$P_{\text{dark}}(t) = s - \frac{ps}{2}\left(1 - \sum_{n=0}^{\infty} w(n, \bar{n})\cos(\Omega_n t)\right), \tag{5.4}$$

where s is the shelving efficiency by the 455 nm laser pulse, and p is the probability of optically pumping to the correct ground state Zeeman sublevel. Before we can find the least squares fit to the data shown in Figure 5.1, we must calculate the Lamb-Dicke parameter, η as in [83], which requires knowledge of ω_{axial}. It is given by $\eta = k_z z_{\text{axial}}$, where, k_z is the projection of the wavevector on the direction of the ion's motion, and z_{axial} describes the size of the zero-point simple harmonic oscillator wave function:

$$z_{\text{axial}} = \left(\frac{\hbar}{2m\omega_{\text{axial}}}\right)^{1/2}, \tag{5.5}$$

and m is the mass of the ion. Thus, the Lamb-Dicke parameter is given by:

$$\eta = \left(\frac{\hbar}{2\pi}\left(\frac{2\pi}{\lambda}\cos(\frac{\pi}{4})\right)^2 \frac{1}{2m\omega_{\text{axial}}}\right)^{1/2} \tag{5.6}$$

where λ is the wavelength of radiation, and we have used the fact that the 2051 nm laser is at 45° to the axial direction. Plugging in numbers, and $\omega_{\text{axial}} = 2\pi \times 410$ kHz, we find $\eta \simeq 0.020$. With all of this in hand, we can combine the previous equations and do a least squares fit using free parameters s, p, $\bar{n}$, and Ω_0. Note that we only sum over the first few hundred terms, to make actual computation run quickly. The results for Figure 5.1 were $s = 0.889$ (which agrees with expectations from branching ratio found in

[38]), $p = 0.96$ (demonstrating that we have good fidelity to optically pump to our chosen state), $\Omega_0 = 2\pi \times 18$ kHz, and $\bar{n} = 72$. The Doppler limited temperature defined in [17] converts to an average occupation number, is approximately 25, so we find that our ion is at approximately 3 T_D, where we have used the equipartition theorem implicitly.

This effort tells us that we are doing a good job Doppler cooling our ion to milliKelvin temperatures, but that we are not at the theoretical limit. This is probably because our lasers are not at the perfect detuning, or intensity. Mainly this discussion was meant to serve as a quick diagnostic of our ion's temperature, and an example of how we use the indirect shelving technique and quantum jump spectroscopy to perform a measurement.

One final thing to note is that if for some reason, we are suddenly cooling the ion poorly, then the average occupation number $\bar{n}$ will increase significantly. If this is the case and thus we can reach a point where we observe a fast decoherence time. One must ensure that this does not occur while an experiment is running.

5.2 2051 nm laser linewidth measurement with adiabatic rapid passage

The final diagnostic that I will discuss is a measurement of our 2051 nm laser's linewidth when frequency stabilized to the high finesse ULE-spaced reference cavity. As I mentioned earlier, we used the result of our work [34], and reached the conclusion that our laser had a linewidth of less than 500 Hz, but were limited by fluctuations in the magnetic field. To improve our knowledge of this laser's behavior, we thought of two directions to make an improved estimate. First we could use the 'clock' transition in $^{137}Ba^{+}$, ($6S_{1/2}, F = 2, m_F = 0 \leftrightarrow 5D_{3/2}, F = 0, m_F = 0$) which is magnetically insensitive and can thus be a great diagnostic tool. For a number of reasons detailed in Section 4.1.5, we have not yet observed this transition. After a discussion with Tom Noel, I realized that some of the magnetic field noise and other slow drifts could be eliminated to shed light on the laser's linewidth. The technique that would be used to eliminate these effects is adiabatic rapid passage, where one can sweep the laser from far below resonance to far above resonance. The benefit of this technique is that it is immune to slow drifts in laser frequency or the ion's resonance, due to the fact that one will always sweep over the transition in question with appropriate sweep parameters.

The details of this technique are thoroughly described in [50] and [51], so I won't derive them, but simply use the result. The procedure for detection by means of shelving is nearly identical to that of Section 5.1, except that instead of using a fixed duration, fixed frequency pulse of 2051 nm radiation, we sweep the laser frequency across the resonance at a rate, α. We vary the sweep rate, and record the shelving efficiency as a function of the sweep rate. We can then convert this value, which includes shelving probability, and optical pumping probability to look at a normalized transfer probability as a function of sweep rate, $P_{\text{trans}}(\alpha)$, given by the following conversion:

$$P_{\text{trans}}(\alpha) = \frac{s - P_{\text{shelve}}}{ps}, \tag{5.7}$$

where p is the probably of optically pumping to the correct ground state ($p \simeq 0.95$), and s is the indirect shelving probability ($s \simeq 0.88$). The experimental results can be found in Figure 5.2.

Using the theoretical model found in [40], we can write the probability of successfully transferring the ion to the $5D_{3/2}$ level:

$$P_{\text{trans}}(\alpha) = \frac{1}{2}\left(1 - e^{-\pi\Gamma\Omega/\alpha}\right) + e^{-\pi\Gamma\Omega/\alpha} P_{LZ} \tag{5.8}$$

where Γ is a dephasing rate equal to the inverse of the coherence time of the laser, Ω is the Rabi frequency on resonance, and P_{LZ} is the probability of adiabatic passage in the Landau-Zener model, given by

$$P_{LZ} = 1 - e^{-\pi\Omega^2/\alpha}. \tag{5.9}$$

Note that the quantities have been not been converted to "experimental units", namely that Ω and Γ are angular frequencies. Fitting this function to the data found in Figure 5.2, has a reduced χ^2 of 2.7, largely because of the point of the slowest sweep rate, where the ion was not behaving very well. The best fit parameters are $\Omega = 2\pi \times 2.04$ kHz, and $\Gamma = 2\pi \times 5$ Hz. If we are to assume that our laser noise spectrum is Lorentzian, then we can identify Γ with the FWHM laser linewidth, as $\Delta_{\text{FWHM}} = \Gamma/\pi = 1.5$ Hz.

This data would suggest that we are doing a very good job narrowing the linewidth of the laser, as the manufacturer quoted linewidth of a free-running laser is expected to be

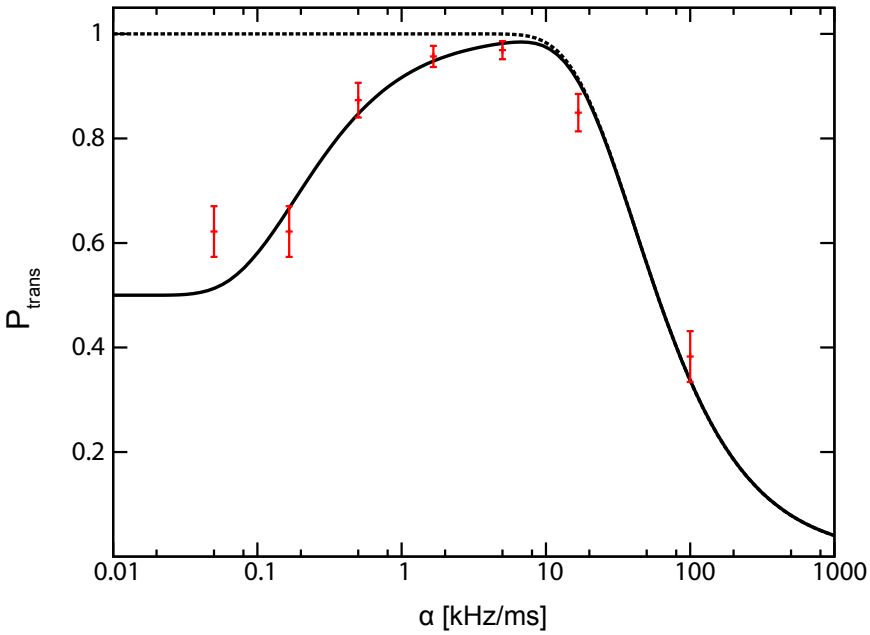

Figure 5.2: Normalized transfer efficiency from adiabatic passage as a function of sweep rate for the 2051 nm laser. The data is shown in red with statistical error bars, and the black, solid curve is the best fit for the function found in Eq. 5.8 with free parameters Ω and Γ which represent the Rabi frequency and dephasing rate, respectively. The black, dashed curve would be the transfer efficiency if there was no dephasing ($\Gamma = 0$).

10 kHz. If a frequency comb is developed in our laboratory, it would be quite interesting to see if the linewidth is really as narrow as this result suggests, as well as at what time scale various noise sources enter.

Chapter 6

MEASUREMENT OF THE LANDÉ g_J FACTOR OF ^{138}Ba$^+$, $5D_{5/2}$

Before I dive into a discussion of the measurement of the Landé g_J factor of the $5D_{5/2}$ level of ^{138}Ba$^+$, I want to place the measurement in a little bit of context, and motivate why we undertook this effort in not one, but two ion traps of the laboratory. At the time, I was undergoing an effort to measure the hyperfine structure of the $5D_{5/2}$ level of ^{137}Ba$^+$, but was having difficulty loading ^{137}Ba$^+$, and was sharing the 1762 nm laser with Tom Noel. In the downtime, I was working on the atomic theory that would surround the measurement, and was wondering how accurate the rf spectroscopy would need to be to place a check on the atomic theory, and observe the nuclear magnetic octupole moment. I wrote a Mathematica notebook to numerically calculate the hyperfine and Zeeman structure (like in Section 2.2.4), and found that if I were to simply use the result of the measurement found by Nathan Kurz et al., [39], it would be not be possible to resolve the octupole moment's contribution to the structure.

Since I had already been using the 1762 nm laser to populate Zeeman sublevels of ^{138}Ba$^+$ reliably, it was relatively easy to start performing magnetic dipole transitions in both the $6S_{1/2}$ and $5D_{5/2}$ Zeeman manifolds. Unfortunately, I quickly realized that there was a problem. I was observing a disagreement to Nathan's measurement at the 1% level, which was *much* larger than either of our statistical uncertainties. As a sanity check, I asked Tom to do a measurement to see if he was observing similar effects. Asking these questions ultimately led to a collaborate measurement of the $5D_{5/2}$, g_J factor by Tom and I which is the highest precision to date. Along the way, we found that the lab's previous measurement in [39] was heavily shifted by a couple of outlying data points, which upon reanalysis needed to be removed. It ended up that I needed to reconstruct the trapping apparatus as a result of large ac-Zeeman effects caused large currents at the rf-drive frequency, informed by the efforts of [37]. Ultimately, all of our measurements came into good agreement, and in [27],

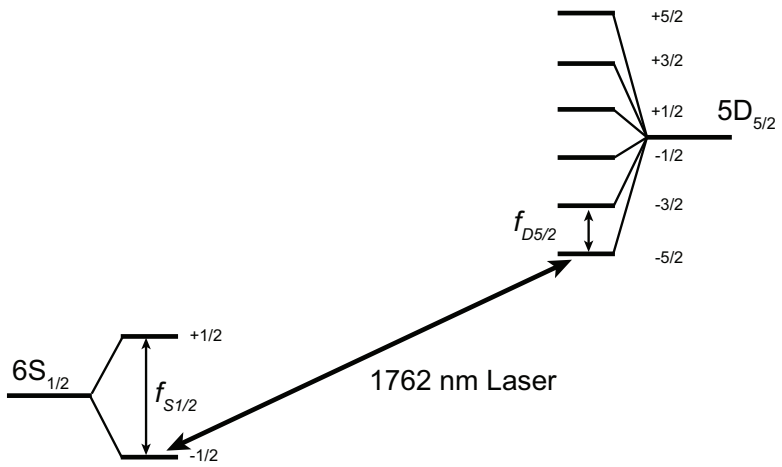

Figure 6.1: Energy levels and transitions employed for the Landé g factor measurement.

we reported the g_J factor to be 1.200 372$(4_{\mathrm{stat}})(7_{\mathrm{sys}})$.

Tom has already detailed the effort undertaken in his trapping apparatus in his thesis [51], so the discussion for the remainder of the chapter will describe the measurements made in my trap.

6.1 Experimental Procedure

To measure the g_J factor of the $5D_{5/2}$ level of $^{138}Ba^{+}$we performed rf spectroscopy of the ground state, $6S_{1/2}$, and the 'shelved' state $5D_{5/2}$. The relevant energy levels are sketched out in Figure 6.1 Since it is slightly more complicated than the measurement of the $6S_{1/2}$ Zeeman splitting, I will now describe the procedure used to measure the $5D_{5/2}$ Zeeman splitting:

(a) Doppler cool the ion with the 493 and 650 nm lasers for 50 ms.

(b) Extinguish the primary 493 nm beam by switching off a single-passed AOM, and use the optical pumping beam to populate $6S_{1/2}, m = -1/2$ for approximately 20 ms. Switch off the single-passed AOM that shutters the optical pumping beam, and switch off the 4 GHz EOM, so that any 493 nm leakage light is detuned by 4 GHz. Extinguish the 650 nm beam with a physical shutter.

(c) Populate $5D_{5/2}, m = -5/2$ using an ARP sweep of the 1762 nm laser.

(d) Wait for a TTL signal from line trigger circuit (to ensure that this step occurs at the same point in the 60 Hz ac phase) to start a fixed duration pulse of constant frequency rf magnetic field to attempt to drive the $5D_{5/2}, m = -5/2 \rightarrow m = -3/2$ transition.

(e) Sweep the 1762 nm laser's frequency so that if the ion were in $m = -5/2$, it is returned to the ground state, and if the ion were in $m = 3/2$, it is unaffected.

(f) Turn on the cooling lasers to check to see if the ion was bright. If an rf-transition occurred, the ion would be 'dark', and if the rf-transition failed, the ion would be 'bright'.

(g) Deshelve the ion using 614 nm light to return the ion to the cooling cycle if it were dark.

(h) Repeat steps (a)-(g) many times (40-100) to accumulate statistics at a single rf-frequency.

(i) Adjust the frequency of the rf synthesizer and repeat until we've scanned across a resonance. We will define the resonant frequency as $f_{D_{5/2}}$.

The procedure to perform the ground state Zeeman splitting measurement is quite similar, but only requires one sweep of the 1762 nm laser. The observed resonant frequency of the ground state Zeeman splitting will be defined as $f_{S_{1/2}}$.

In Figure 6.2, typical results of the experimental procedure for the $6S_{1/2}$ and $5D_{5/2}$ levels are shown. We plot the probability of finding the ion in the 'dark' state against the frequency of the oscillating magnetic field, with error bars indicating the 1-σ statistical standard deviations based on 100 trials at each frequency. The curves are four-parameter least-squares fits to the standard Rabi oscillation function for coherent excitation by a square pulse of radiation with duration t:

$$P_{\text{dark}}(f) = \alpha + \beta \frac{\Omega^2}{W^2} \sin^2 \left[W \frac{t}{2} \right], \tag{6.1}$$

where $W^2 = \Omega^2 + [2\pi(f - f_0)]^2$. Two of the fit parameters are scaling factors α and β, which account for optically pumping to the wrong ground state sublevel ($m = +1/2$) and imperfect transfer efficiency with the 1762 nm laser. The other two are the Rabi frequency of the transition, Ω, and the resonance frequency, f_0. Note that fitting to a Lorentzian or Gaussian will yield a resonance frequency that agrees within the statistical uncertainty with our fit, but result in a larger reduced χ^2 as these functions don't represent the proper lineshape.

Recalling Section 2.1.2, the resonance frequencies of the Zeeman transitions in each level are given by:

$$f_i = \frac{1}{h} g_i \mu_B B, \tag{6.2}$$

where h is Planck's constant, g_i is the Landé g_J factor of the state in question, μ_B is the Bohr magneton, and B is the magnitude of the static laboratory magnetic field. Using the two resonance frequencies measured in our experiments , $g_{D_{5/2}}$ can thus be calculated from

$$g_{D_{5/2}} = g_{S_{1/2}} \frac{f_{D_{5/2}}}{f_{S_{1/2}}}, \tag{6.3}$$

assuming that the magnetic field remans constant over the duration of the experiment. At the time, we used the measured value of $g_{S_{1/2}}$ from [35]: 2.002 490 6(11), but in hind sight we could have used the improved value from [46]. Since they agree to approximately 1-σ, and do not limit the precision of our experiment, it is not necessary to reanalyze the data. Should one want to improve upon our measurement of $g_{D_{5/2}}$, the updated value from the Penning trap could prove useful.

To perform the measurement, we interleaved measurements of the ground state splitting with the 'shelved' state splitting as quickly as possible, so that we could account for magnetic field drift. Each pair of independent frequency scans constitutes a measurement of the g-factor. The results of these measurements are summarized in Figure 6.3, shown with a combined statistical uncertainty and systematic uncertainty. The squares are the measurements from my ion trapping apparatus, while the circles are from Tom Noel's. The black line shows the weighted mean, and the grey bars represent the combined 1-σ confidence interval. The statistical uncertainty arises from the binomial uncertainties in the measured

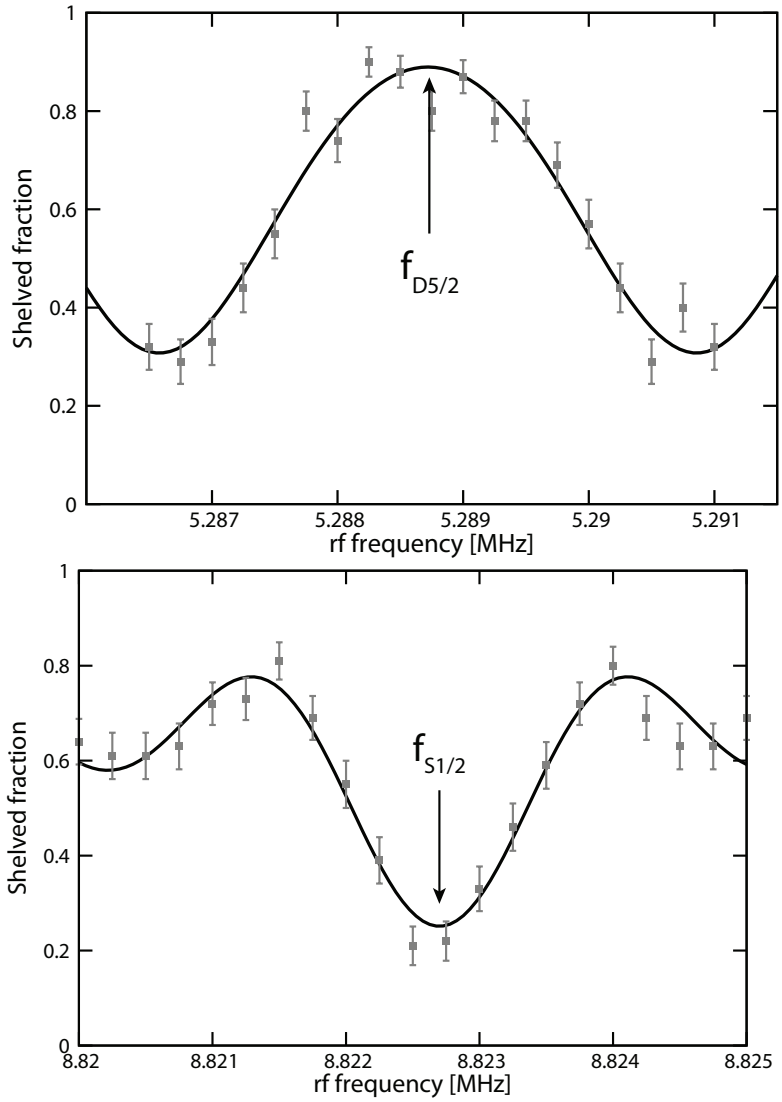

Figure 6.2: Results of rf spectroscopy of Zeeman transitions in $5D_{5/2}$ and $6S_{1/2}$. Typical experimental data showing the shelved fraction of the ions plotted against the frequency of the oscillating magnetic field. The upper plot shows the $5D_{5/2}$ resonance, and the bottom shows the $6S_{1/2}$ resonance. Statistical error bars are shown, calculated from a binomial distribution based on 100 trials at each rf frequency. A least-squares fit function based on Eq. 6.1 is overlaid. The fitted values of the resonance frequencies are 5.288 72(4) MHz with a reduced χ^2 of 2.04 for the upper plot, and 8.822 70(3) MHz with a reduced χ^2 of 1.29 for the lower plot, and are indicated by arrows.

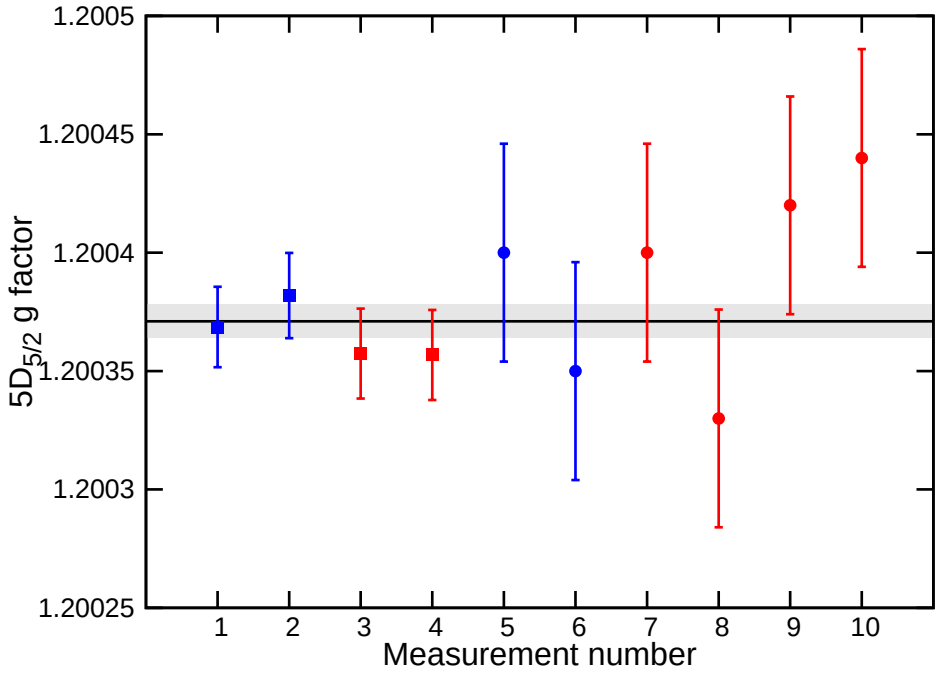

Figure 6.3: Summary of measurements of the Landé g factor of $5D_{5/2}$. The 10 measurements of $g_{D_{5/2}}$ are shown. The measurements for my trap are shown with squares and circles are for Tom's. The different colors, blue and red, indicate different trap depths used, which could manifest an ac-Zeeman effect. The errors bars represent calculated 1-σ combined uncertainties. The weighted mean of the measurements of each apparatus agree to within 1-σ. The solid line represents the weighted mean of all 10 measurements, and a 1-σ confidence interval is shown in grey.

shelved fractions at each frequency, propagated through to an error in the fit resonance frequency, f_0. The systematic uncertainty is discussed in the following section.

6.2 Systematic Effects

There are several systematic effects that could skew the measurement of $g_{D_{5/2}}$; however, all appear to be well-controlled in our experiments. We will analyze the effects due to magnetic field fluctuation, magnetic field gradients, the ac-Zeeman effect, ac-Stark effect and 60-Hz jitter. One additional vote of confidence is that our two experiments in two

different apparatus agree quite well. If there were some large, lurking systematic, it would have likely shown up in one trap or the other, but not both equally.

In our paper [27], we discussed these effects in descending order of size. Here I should briefly discuss the state of affairs before a new trap was constructed. Essentially what we observed were large shifts of the frequencies if we varied the trap depth (especially if the micromotion was not compensated well). For example, one day's data showed a shift of nearly 10 kHz if we changed the trap drive rf power from 3 W to 4 W over the course of minutes. This shift is of similar to the size found in [37], and is simply unacceptable for our work. While I spent about a month looking for reasons, this shift was too large to be magnetic field drift, and was repeatable. Every measurement I did had a larger splitting at high trap rf than low, which is consistent with an ac-Zeeman effect as the trap drive was always detuned to the blue (at the time $\omega_{\rm rf} \simeq 22$ MHz) from the atomic transition. As described in Section 4.3.1, we eliminated possible induction loops and rf-mismatch, and this seems to have eliminated the problem for the Landé g experiment.

The presence of trapping rf voltages may cause an ac-Zeeman effect that would perturb the resonance frequencies of the ground and excited states differently. This effect could manifest itself because the ion exhibits uncompensated micromotion and oscillates at ω_{rf} in the magnetic field gradient described above, or due to an ac current at ω_{rf} produced by the trapping electrodes. Either method causes an oscillating magnetic field at the site of the ion, and depends on the amplitude of the rf voltage that drives our trap. We find that an ac-Zeeman effect does not result in a statistically significant shift. The measurements at low (high) trap rf voltage are shown in Figure 6.3 in blue (red). We can then place a fractional error below the 10^{-6} level for this measurement.

We were really worried about magnetic field fluctuations, especially since we observed that the bus was causing large spikes in the magnetic field during the day on weekdays as was described in Section 4.3.3. To avoid this, I took data on weekends, when I knew that the buses were running with gas rather than electricity. I additionally set up the fluxgate magnetometer and monitored the magnetic field over the entire duration of the experiment, so that if the magnetic field jumped wildly, I could ignore that data, but this precaution ended up not being necessary. Over the entire course of the experiment, we

observed approximately 100 μG drifts in the magnetic field on the fluxgate magnetometer.

The largest drift in the magnetic field during the course of a single measurement (approximately 400 s) corresponded to a 20 μG drift in the ambient magnetic field. This results in a conservative systematic error of 1.3×10^{-5} on each measurement of $g_{D_{5/2}}$. Since the magnetic field will fluctuate randomly, multiple measurements will reduce this error. Any fast fluctuations of the magnetic field would result in broadening of the Zeeman resonance lineshape. Tom, on the other hand, repeatedly measured the ground state splitting, $f_{S_{1/2}}$ as quickly as possible, and found that the magnetic field fluctuated randomly by approximately 100 μG in a 5-minute period, resulting in an uncertainty of 4.6×10^{-5}. For more details, see [51].

A magnetic field gradient could affect this measurement if the ion were to shift its position in the trap over the course of the experiment. At the time, Tom and I had very similar apparatus to produce the static magnetic field, and estimated that our magnetic field gradients would be on the same order of magnitude. Tom measured a gradient along the trap axis of 0.14 G/cm. In any event, monitoring the ion's position using the EMCCD camera showed that the ion does not change its position by more than 1 μm, which places an upper limit of 1×10^{-5} on the systematic uncertainty of $g_{D_{5/2}}$ due to ∇B.

One must also worry about leakage light that can shift the Zeeman energy levels through the vector ac-Stark effect. This could be due to the 1762 nm laser, the 493 nm laser, or the 614 nm laser for us. To assess these effects, one must estimate the Rabi frequency caused by the excitation by resonant leaking light, and also the detuning. To work through a single example, it was known that the 493 nm laser could saturate the $6S_{1/2} \leftrightarrow 5D_{3/2}$ transition with approximately 40 μW of radiation. When extinguished we could observe approximately 10 pW. Thus the Rabi frequency should be of order 10 kHz on resonance, using the fact that the transition is saturated by approximately 10 μW, which would have a Rabi frequency of $\Omega \simeq 2\pi \times 17$ MHz . However, when the light is extinguished using the EOM and AOM combined, the beam is detuned by approximately 4.1 GHz. Then example there would be an energy shift ~ 1 mHz. Considering all of the leakage light powers and the detunings from resonances, we can place a fractional error $< 10^{-6}$ on our experiments. We have additional confirmation that this is the case, as Tom and I have different amounts

of leakage light that could address the ion at different detunings, which should affect our measurements differently, but do not observe a statistically significant difference in our results.

Tom goes through a nice measurement of how the magnetic field changes as a function of the 60 Hz ac phase using the ion in with the line [51]. This is because any equipment powered by the wall voltage will radiate a magnetic field at 60 Hz . He observed a 60 Hz magnetic field of approximately 2.5 mG peak to peak. This is a good order of magnitude estimate for our trap as well. For this effect to manifest itself, one would need to have jitter on the timing of the the rf spectroscopy pulse. We estimate that this comes in below the 10^{-7} level.

A summary of all of these systematic effects can be found in Table 6.1. Finally, we report that we have measured the Landé g factor of the $5D_{5/2}$ level of $^{138}Ba^{+}$ to be 1.200 372$(4_{\mathrm{stat}})(7_{\mathrm{sys}})$. The reduced χ^2 of these ten measurements were found to be 0.65. This measurement for the $5D_{5/2}$ level Landé g_J factor of has a factor of 70 reduction in statistical error compared to [39], and remains to the best of my knowledge, the most accurate measurement to date. This agrees with another recent measurement [42] at the 3-σ level.

Table 6.1: A summary of systematic error estimates for our experimental apparatuses.

Error Source	$\Delta g_{D_{5/2}}$ Matt	$\Delta g_{D_{5/2}}$ Tom
B Fluctuations	1.3×10^{-5}	4.6×10^{-5}
B Gradient	1×10^{-5}	1×10^{-5}
ac Zeeman Effect	10^{-6}	10^{-6}
60Hz Jitter	10^{-7}	$< 10^{-7}$
Total	1.6×10^{-5}	4.7×10^{-5}

6.3 Conclusions and Future Directions

Now that magnetic shielding has been built for the apparatus, it seems quite possible that one could measure the Landé g factor of $5D_{5/2}$ (or $5D_{3/2}$ for that matter) to an even higher

accuracy. It would all rely upon the the best ground state g factor measurement found in [46], however. It is my opinion that even though we could improve upon this measurement, it may not be important enough to merit undertaking the task. I reiterate that we underwent this measurement to enable our effort to measure the $5D_{5/2}$ hyperfine splittings, and our new measurement should offer sufficient accuracy for this effort. Additionally a group of theorists has offered a calculations to test their theory of g-factor anomalies and compared to our work (see [22], for example), however, our current measurement should, again, be at sufficient accuracy for now. All of that being said, it seems possible to improve this measurement by at least an order of magnitude with the inclusion of shielding, but this should not be the sole justification.

Chapter 7

MEASUREMENT OF THE $^{137}Ba^{+}$ HYPERFINE INTERVALS AND OBSERVATION OF THE NUCLEAR MAGNETIC OCTUPOLE MOMENT

And now, we can finally get to the measurement of the hyperfine intervals of $^{137}Ba^{+}$. But before we launch straight into the measurement itself, we should take a paragraph to motivate the problem. At the time of the proposal to measure the nuclear magnetic octupole moment of $^{137}Ba^{+}$ in [3], there had been only one other measurement of an octupole moment. The work by Tanner et al. [20] had a surprising result that the nuclear shell model underestimated the magnitude of the octupole moment for ^{133}Cs by a factor of 40. Despite the fact that the nuclear shell model is a coarse approximation, the result was surprising nonetheless. It was suggested that a measurement in $^{137}Ba^{+}$ could offer insight to the problem, as it contains one additional proton and three extra neutrons, which isn't drastically different. I should note that [33] offers a nice treatment of the theory surrounding calculations of these multipole moments. Lastly, this measurement would provide a great opportunity to benchmark the experimental apparatus on the way to a measurement of PNC in Ba^{+} [18] that requires many of the same techniques and equipment.

That being said, it's time to launch into the experimental effort. We will employ basically every technique that we discussed in all of the previous sections in concert. Fortunately, many systems can be checked using a single $^{138}Ba^{+}$ ion, so one can know that most of the systems are setup and working reliably before attempting to trap $^{137}Ba^{+}$. That being said, all of the spectroscopy requires that a $^{137}Ba^{+}$ is trapped, and well laser cooled. Should the cooling performance drop, it will be difficult to populate the hyperfine sublevels with the 2051 nm laser and perform state readout at the end. For the readers' reference, a schematic of the hyperfine manifold with the magnetic dipole transitions used in the experiment is shown in Figure 7.1. In brief, what we will do is interleave measurements of the magnetic field (by measuring the $\Delta m_F = \pm 1$ and taking the difference in these two frequencies), with

measurements of the magnetic 'insensitive' transitions ($\Delta m_F = 0$), which we will call f_{32}, f_{21}, and f_{10}.

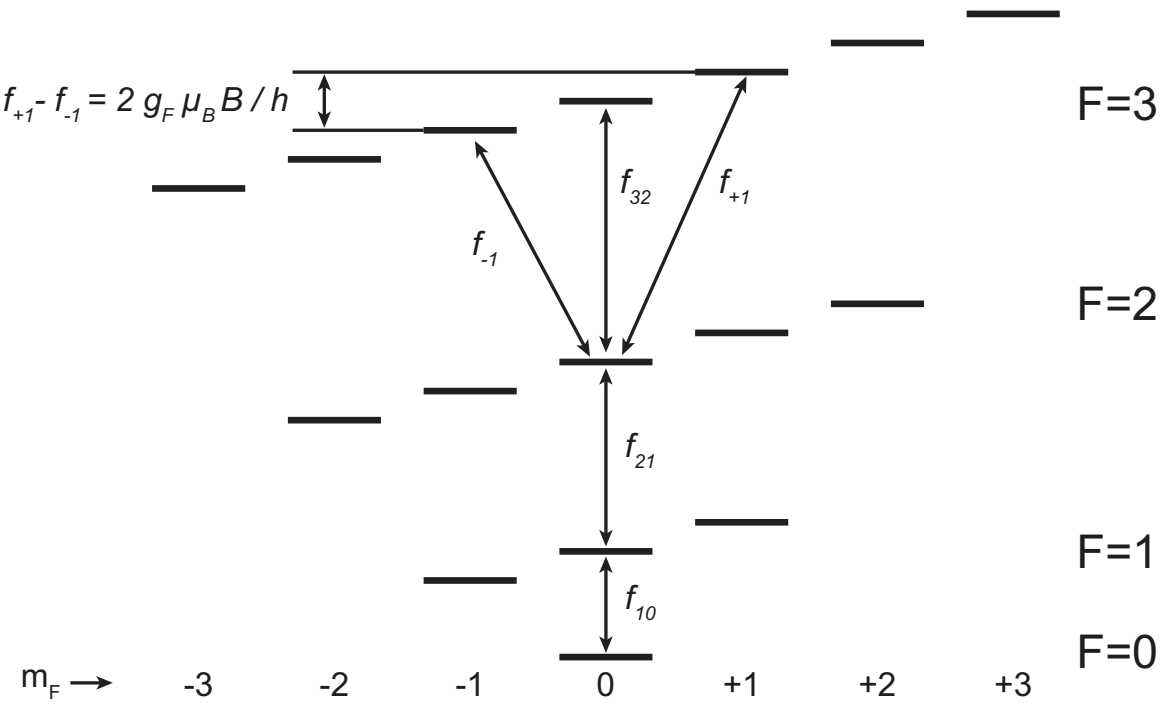

Figure 7.1: $5D_{3/2}$ Hyperfine manifold energy level diagram with relevant transitions. The hyperfine intervals and Zeeman sublevels are depicted, with the magnetic quantum number, m_F increasing from left to right. We use the $\Delta m_F = \pm 1$ transitions to calibrate the magnetic field, which are insensitive to the quadratic Zeeman effect.

What we really care about is what the hyperfine splittings would be at zero magnetic field (where laser cooling is inefficient), so we will measure the splittings at several magnetic fields, and use our knowledge of the quadratic Zeeman effect to extrapolate to zero magnetic field. Along the way, we'll concern ourselves with the higher order Zeeman effects that could cause perturbations, as well as a number of other systematic effects.

7.1 Experimental Procedure

We start by trapping a $^{137}Ba^{+}$ ion using the 791 nm laser detuned by -925 MHz from the ^{138}Ba resonance and the N_2 laser. Once a single ion is trapped, we Doppler cool and compensate micromotion by changing the trap depth repeatedly, and adjust the horizontal and vertical compensation, until the ion's image does not visibly move on the EMCCD camera as a function of the trap depth. The laser frequencies and powers are then adjusted with until the ion is cooled as efficiently as possible. From there we can start the experimental procedure:

(a) Doppler cool the ion using the linearly polarized cooling beam with two frequencies of 493 nm light, and the four frequencies of 650 nm light for approximately 50 ms.

(b) Extinguish the 493 nm beam, and expose the ion to the secondary, circularly polarized 493 nm beam for approximately 20 ms. The fluorescence will cease, and the ion will be optically pumped to the stretched state, $6S_{1/2}, F = 2, m_F = -2$.

(c) We then extinguish all of the 493 nm light, by switching the shutter AOM for the optical pumping beam, and switch the EOM off as well so that any leakage light (less than 1 pW) will be detuned by 4 GHz. The four 650 nm beams are all extinguished using a mechanical shutter to ensure that there is absolutely no leaking red light.

(d) Drive a resonant π-pulse with the 2051 nm laser to populate the $5D_{3/2}, F = 2, m_F = 0$, which takes approximately 60 μs, once triggered on the 60 Hz ac line.

(e) Wait for the next TTL pulse from the 60 Hz line trigger to start a fixed duration pulse of constant frequency rf magnetic field to attempt a transition between hyperfine levels. This pulse is approximately 500 μs in duration for the $\Delta m_F = \pm 1$ transitions, and 30 ms for the $\Delta m_F = 0$ transitions, and the HP8756B amplitude is set such that these are π-pulses on resonance.

(f) Expose the ion to another, identical, pulse of 2051 nm radiation. If the rf transition occurred, then the ion will remain in $5D_3/2$, but if it failed, the ion will be returned the the ground state.

(g) Apply a 20 ms pulse of 455 nm radiation to 'shelve' the ion if it is in $6S_{1/2}$.

(h) Turn on the cooling lasers to perform state detection and record the ion's fluoresence for 50 ms. If the rf-transition was successful, the ion be bright, and if it failed, then the ion will be dark (up to ineffeciencies in optical pumping, transfer to $5D_{3/2}$, and shelving).

(i) Deshelve the ion if necessary, using a 20 ms pulse of 614 nm radiation.

(j) Repeat steps (a) - (i) many times (between 50 and 100) to accumulate statistics at a single rf frequency. This sequence can take up to a minute, depending on how many trials are used.

(k) Change the frequency of the HP8657B synthesizer, and repeat, scanning over the resonance of the desired transition. The synthesizer must be given time to settle for the reasons discussed in Section 4.2.

This procedure requires knowledge of the frequency and π-time of the E2 transition at 2051 nm, as well as approximate knowledge of the hyperfine transition frequency and π-time in question. Typically we use higher rf powers when searching for the transition initially, then decrease the rf power, and increase the pulse duration accordingly[1]. For the measurement of f_{-1}, f_{+1}, f_{32}, and f_{21}, this is the full procedure, but for measuring f_{10} we have to insert a few additional operations as follows:

(a) Populate $5D_{3/2}, F = 2, m_F = 0$ using steps (a) through (d) as before.

(b) Drive a resonant π-pulse with $t_\pi \simeq 300$ μs, to populate $5D_{3/2}, F = 1, m = 0$ using the Minicircuits Synthesizer that is referenced to the HP8656B.

[1]Decreasing the 8656B output power by 20 dB will increase the π-time by a factor of 10.

(c) Wait for a TTL pulse from the 60 Hz line trigger to start a fixed duration pulse of constant frequency rf magnetic field (sourced by the HP8656B synthesizer) to attempt a transition between $F = 1$ and $F = 0$. This pulse is typically 8 ms in duration when attempting to measure the f_{10} with high precision.

(d) Apply a π-pulse identical to step (b) using the Minicircuits synthesizer. It will return the ion to $F = 2, m_F = 0$ if the spectroscopy step was not successful.

(e) Repeat steps (f)-(k) from the earlier procedure to perform state detection and check whether an rf transition occurred.

To calibrate the magnetic field and measure the resonance frequency of one of the magnetically insensitive transitions, we perform a series of rf-spectroscopy scans as quickly as possible. For example, to measure f_{32}, we first scan across, f_{+1}, then f_{32}, f_{-1}, f_{32} again, and finally f_{+1}. This lets us calibrate the magnetic field twice, and have two measurements of the hyperfine splitting with Hz-level precision. This whole sequence takes approximately an hour. We then repeat a similar procedure for f_{21}, and f_{10}, change the magnetic field by adjusting the current on the main magnetic field coils, and repeat everything. Examples of the narrowband resonance features for the three $\Delta m_F = 0$ transitions at approximately $\boldsymbol{B} \simeq 1.65$ G are found in Figure 7.2. Examples of the magnetic field calibration scans are found in Figure 7.3.

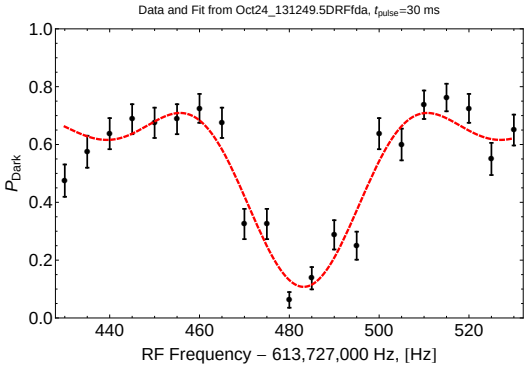

(a) Best fit parameters for the $3 \leftrightarrow 2$ transition: $\Omega = 118(14)$ rad/s, $\alpha = 0.709(27)$, $\beta = -0.63(1)$, $f_{32} = 613\ 727\ 483.16(59)$ Hz, reduced $\chi^2 = 3.1$

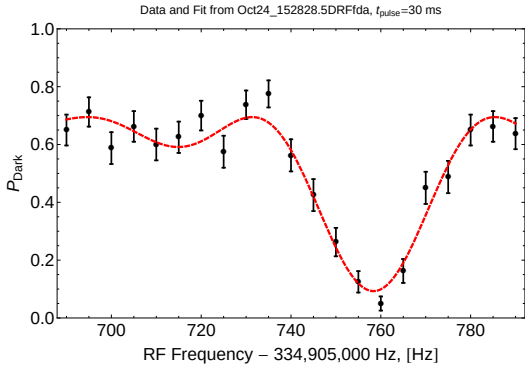

(b) Best fit parameters for the $2 \leftrightarrow 1$ transition: $\Omega = 122(9)$ rad/s, $\alpha = 0.69(2)$, $\beta = -0.65(8)$, $f_{21} = 334\ 905\ 758.38(63)$ Hz, reduced $\chi^2 = 1.5$

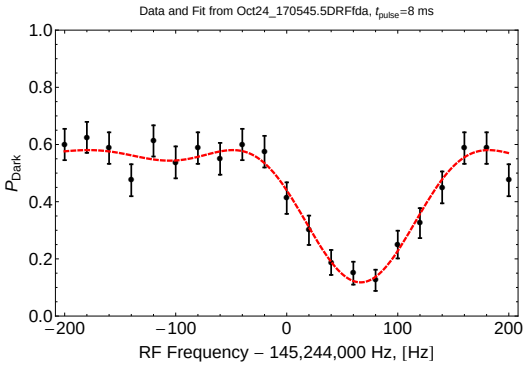

(c) Best fit parameters for the $1 \leftrightarrow 0$ transition: $\Omega = 388$ rad/s, $\alpha = 0.58(1)$, $\beta = -0.52(15)$, $f_{10} = 145\ 244\ 066.5(3.4)$ Hz, reduced $\chi^2 = 0.68$

Figure 7.2: Typical resonance scans for the $\Delta m_F = 0$ transitions between hyperfine levels of the $5D_{3/2}$ level of $^{137}Ba^+$. The probability of finding a dark ion is plotted against the frequency of the HP8656B synthesizer that drives the oscillating magnetic field used for spectroscopy. The red line shows the best least-squares fit to the function found in Equation 7.1. Each data point represents 80 trials at a single frequency. The $F = 1 \leftrightarrow F' = 0$ resonance has lower contrast because of inefficiencies in the additional steps required to perform this experiment, which necessitated a faster Rabi frequency.

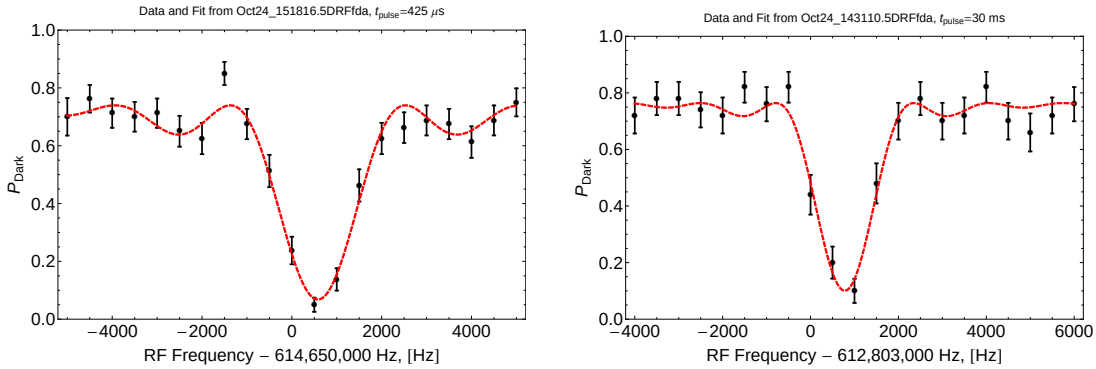

(a) Best fit parameters for the $3 \leftrightarrow 2$, $\Delta m_F = +1$ transition: $\Omega = 8260 \pm 590$ rad/s, $\alpha = 0.74(1)$, $\beta = -0.69(6)$, $f_{+1} = 614\,650\,581(45)$ Hz, reduced $\chi^2 = 1.1$. The pulse duration for this scan was 425 μs.

(b) Best fit parameters for the $3 \leftrightarrow 2$, $\Delta m_F = -1$ transition: $\Omega = 3530 \pm 1800$ rad/s, $\alpha = 0.76(1)$, $\beta = -0.83(51)$, $f_{-1} = 612\,803\,779(50)$ Hz, reduced $\chi^2 = 0.86$. The pulse duration for this scan was 600 μs.

Figure 7.3: Typical resonance scans for the $\Delta m_F = \pm 1$ transitions between hyperfine levels of the $5D_{3/2}$ level of $^{137}Ba^+$. The probability of finding a dark ion is plotted against the frequency of the HP8656B synthesizer that drives the oscillating magnetic field used for spectroscopy. The red line shows the best least-squares fit to the function found in Equation 7.1. Each data point represents 80 trials at a single frequency. These two scans are used to calibrate the magnetic field.

7.2 Data analysis

7.2.1 Extraction of resonance frequencies from spectroscopy

From the data like that in Figure 7.2, we need to extract the resonance frequency and the standard error on this parameter. Like in the Landé-g_J experiment, we will use a four-parameter least squares fit to the Rabi oscillation function for coherent excitation by a square pulse of radiation with duration t (identical to Equation 7.1):

$$P_{\text{dark}}(f) = \alpha + \beta \frac{\Omega^2}{W^2} \sin^2 \left[W \frac{t}{2} \right], \tag{7.1}$$

where $W^2 = \Omega^2 + [2\pi(f - f_0)]^2$. The fit parameters α and β for the offset and amplitude of the peaked-function are not nearly as simple as they were for the Landé-g_J experiment, since we require more steps to perform the spectroscopy that can all have some inefficiency. We could introduce many more parameters to account for each effect (e.g. optical pumping probability, shelving efficiency, etc) separately, but the most important feature is the resonance frequency f_0. The best-fit parameters can be found for a few examples in Figure 7.2. As a final note, the parameters for amplitude, β, and Rabi frequency, Ω are not independent parameters, which explains the large uncertainty of these values.

7.2.2 Calibration of Magnetic Field and 60 Hz Correction.

It was simple to calibrate the magnetic field (or unnecessary from a different point of view) for the Landé g_J experiment of Chapter 6 as there was just the linear Zeeman effect to worry about. This isn't the case for the levels of the $5D_{3/2}$ hyperfine manifold in $^{137}Ba^+$, which have quadratic Zeeman effects coming in at several kHz/G^2. We could account for these just using theory, but it requires a bit of circular logic. To precisely calculate the quadratic Zeeman shifts, we would need good knowledge of the hyperfine splittings, which is exactly what we're trying to measure.

To get around this, we can use a pair of transitions to calibrate the magnetic field instead, namely the $F = 2, m_F = 0 \leftrightarrow F = 3, m_F = \pm 1$ transitions, that have a frequency $f_{\pm 1}$, respectively. All of the states involved will have quadratic Zeeman shifts, but $F = 3, m_F = \pm 1$ will have a common second order shift. Since the $F = 2, m_F$ initial state is

shared, its quadratic Zeeman shift is common mode as well, and will also drop out when we find the difference between the two frequencies. The magnetic field can thus be calculated using:

$$B = \frac{f_{+1} - f_{-1}}{2g_F\mu_B/h}, \tag{7.2}$$

where g_F was defined in Equation 2.26, and has a value of 0.399 494 004(15), using the results of [46] and [36] for g_J and g_I, and μ_B is the Bohr magneton. The uncertainty on g_F does not limit the uncertainty in magnetic field calibration. Thus, for each pair of measurements of f_{+1} and f_{-1} we are able to calibrate the magnetic field.

There is one important correction that we will need to apply to account for: a 60- and 120-Hz oscillating magnetic field in the laboratory that was observed to be radiating from transformers in the vicinity of the ion trap. Using a fluxgate magnetometer borrowed from Prof. Blayne Heckel's group[2], we measured the oscillating magnetic field along the quantization axis of our trap as shown in Figure 7.4, triggered by the same line trigger that starts the spectroscopy rf pulses. This shows that over the course of the 8 ms pulse used to measure f_{10} and 30 ms pulse used to measure f_{21} and f_{32}, the time-averaged magnetic field $\boldsymbol{B}$ is larger than what was measured during the magnetic field calibration scans (which only take 425 μs and 600 μs, for f_{+1} and f_{-1} respectively).

To account for this effect, we find the time-averaged magnetic field change over a pulse of duration τ given by:

$$\Delta B(\tau) = \frac{1}{\tau}\int_0^\tau f_B(t)\mathrm{d}t, \tag{7.3}$$

where $f_B(t)$ is the fit function to the data in Figure 7.4. The form of this function is:

$$f_B(t) = C_1 \sin\left(2\pi \times 60t + \phi_1\right) + C_2 \sin\left(2\pi \times 120t + \phi_2\right), \tag{7.4}$$

with t in seconds. The best fit parameters to the data are $C_1 = 0.46$ mG, $C_2 = -1.03$ mG, $\phi_1 = 0.46$ rad, $\phi_2 = 1.80$ rad. For example, for an 8 ms pulse, the time-averaged magnetic field was 1.3 mG higher than the magnetic field calibration accounted for.

We can apply a shift to the measured frequency of f_{10}, f_{21}, and f_{32}, using the knowledge of the second order Zeeman effect (which is known to sufficient accuracy to account for these

[2] A one axis Schnostedt DM2220 fluxgate magnetometer

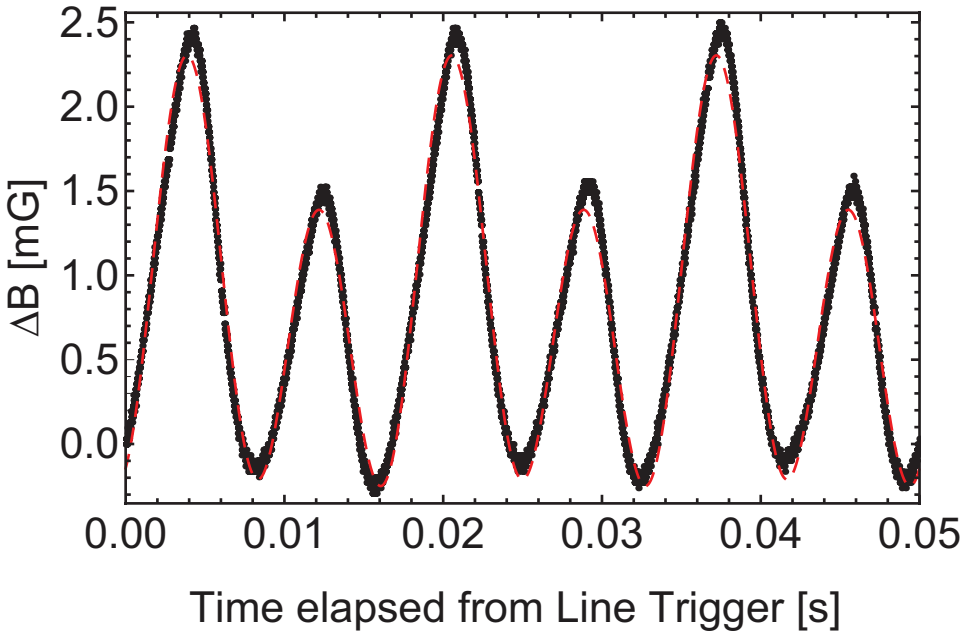

Figure 7.4: 60- and 120-Hz ac magnetic field observed at the ion trap. The data (black dots, making a line) represent 5,000 samples taken at 100,000 samples per second, referenced to a TTL pulse from the same line trigger that starts the experimental procedure. The magnetometer was oriented along the ion's quantization axis, and a dc offset has been removed. The data fit to the function found in Equation 7.4, with the best fit shown as the red, dashed line.

magnetic fields). The value of the shift for pulse duration τ is:

$$\Delta f_x = -2Q_x B \Delta B(\tau) \tag{7.5}$$

where Q_x is the second order Zeeman coefficient calculated from the values in Table 2.5 for the transition in question and B is the magnetic field calculated from the magnetic field calibration described earlier. Ultimately, we don't know that the magnitude of the ac-magnetic field measured by the fluxgate magnetometer outside the vacuum chamber is the same as the magnetic field observed by the ion. So to account for this, we will include a conservative uncertainty of half the size of the overall shift. For f_{32}, f_{21} and f_{10} the rough size of these corrections are +3 Hz, +15 Hz, and −60 Hz, respectively.

One final note, since the experiments to measure f_{+1} and f_{-1} have different rf-spectroscopy pulse durations, the longer pulse will interrogate the ion with a slightly larger time-averaged magnetic field. We account for this by correcting the magnetic field for each experiment by -110 ± 55 μG. This effect will be small compared to the ac-magnetic field, but this effect is on the order of the statistical uncertainty from the magnetic field calibration.

7.2.3 Extrapolating to find the zero-field hyperfine splittings

After calibrating the magnetic field for each measurement of the resonance frequency of the $\Delta m_F = 0$ transitions at five magnetic fields ranging between approximately 1 and 2 G, we can perform a final two-parameter, weighted least squares fit to the data:

$$f_x(B) = W_x + Q_x B^2, \tag{7.6}$$

where W_x represents the zero-field splitting such that $W_F = \Delta E_F - \Delta E_{F-1}$, and Q_x is the difference in the quadratic Zeeman shifts for the two states in question. The results of the measurements of f_{32}, f_{21}, and f_{10} are plotted against the measured magnetic field in Figures 7.5, 7.6, and 7.7 respectively. The best fit parameters for each of these curves are summarized in Table 7.1.

Table 7.1: Measured hyperfine splittings of $^{137}Ba^{+}$, $5D_{3/2}$, and measured quadratic Zeeman effects with comparison to second-order perturbation theory. The comparisons between calculated and measured Q show good agreement.

Transition	Zero-field Splitting [Hz]	Measured Q [Hz/G^2]	Calculated Q [Hz/G^2]
W_3	613 730 631.0(1.1)	-1 155.11(65)	-1 153
W_2	334 921 349.5(2.7)	-5 712.7(1.7)	-5 708
W_1	145 193 653 (29)	+18 465(17)	+18 544

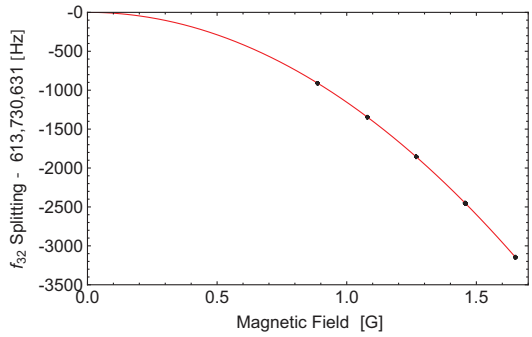

(a) Measured resonance frequencies f_{32} plotted against magnetic field are shown in black, with the quadratic fit shown in red. Error bars are shown, but are not visible at this scale.

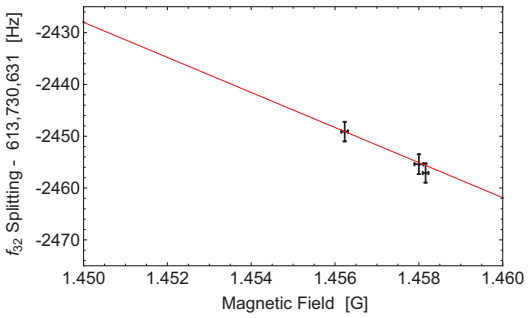

(b) Magnified view of three runs over two days found in (a) shown in black, with the same fit shown in red. The horizontal and vertical error bars represent the 1-σ uncertainty in f_{32} from fitting to the Rabi oscillation functions, as well as the uncertainty in the correction due to 60/120 Hz magnetic field.

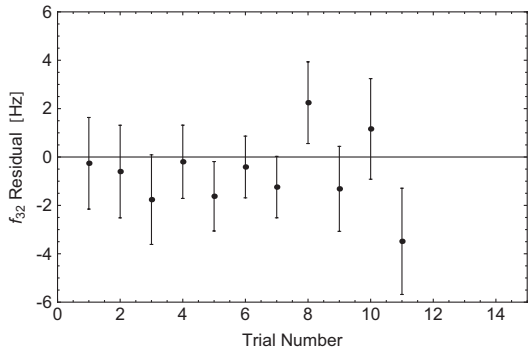

(c) Residuals from the best fit function plotted against chronological trial number

Figure 7.5: The $5D_{32}, F = 3 \leftrightarrow F = 2, \Delta m_F = 0$ hyperfine splitting extrapolated to zero-field. The weighted least-squares fit parameters to Equation 7.6 are $W_3 =$ 613 730 631.0(1.1) Hz, and $Q_{32} = -1\ 155.11(65)$ Hz/G^2 with a reduced $\chi^2 = 0.75$

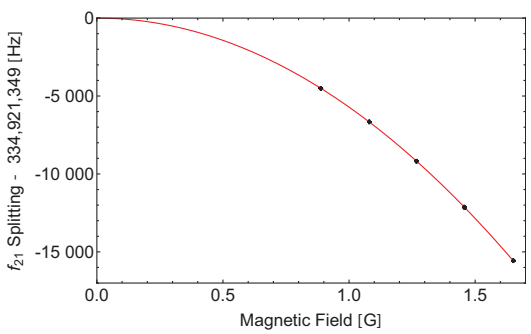

(a) Measured resonance frequencies f_{21} plotted against magnetic field are shown in black, with the quadratic fit shown in red. Error bars are shown, but are not visible at this scale.

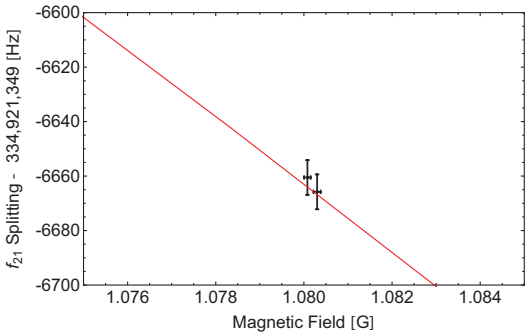

(b) Magnified view of two runs found in (a) shown in black, with the same fit shown in red. The horizontal and vertical error bars represent the 1-σ uncertainty in f_{21} from fitting to the Rabi oscillation functions, as well as the uncertainty in the correction due to 60/120 Hz magnetic field.

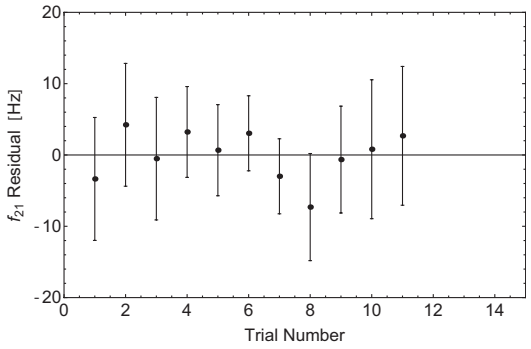

(c) Residuals from the best fit function plotted against chronological trial number

Figure 7.6: The $5D_{32}, F = 2 \leftrightarrow F = 1, \Delta m_F = 0$ hyperfine splitting extrapolated to zero-field. The weighted least-squares fit parameters to Equation 7.6 are $W_2 =$ 334 921 349.5(2.7) Hz, and $Q_{32} = -5\ 712.7(1.7)$ Hz/G^2 with a reduced $\chi^2 = 0.26$

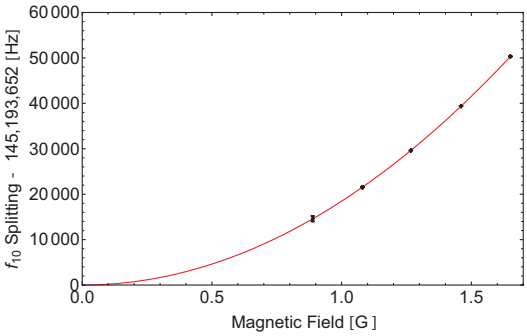

(a) Measured resonance frequencies f_{10} plotted against magnetic field are shown in black, with the quadratic fit shown in red. Error bars are shown, but are barely visible at this scale.

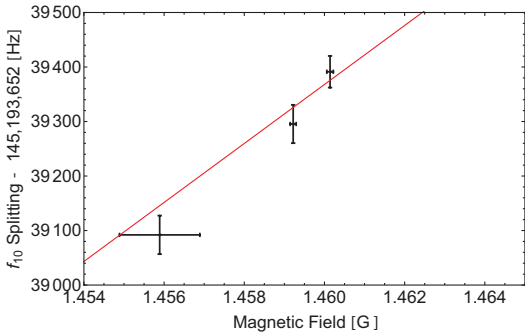

(b) Magnified view of three runs found in (a) shown in black, with the same fit shown in red. The horizontal and vertical error bars represent the 1-σ uncertainty in f_{10} from fitting to the Rabi oscillation functions, as well as the uncertainty in the correction due to 60/120 Hz magnetic field.

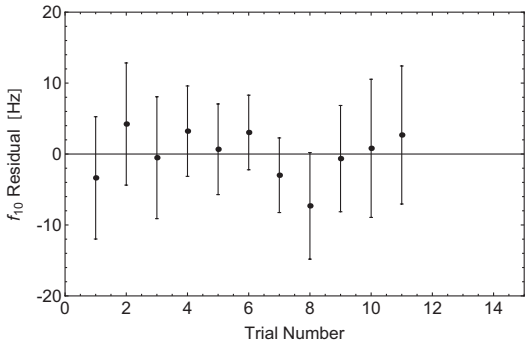

(c) Residuals from the best fit function plotted against chronological trial number

Figure 7.7: The $5D_{32}, F = 1 \leftrightarrow F = 0, \Delta m_F = 0$ hyperfine splitting extrapolated to zero-field. The weighted least-squares fit parameters to Equation 7.6 are $W_2 =$ 145 193 653(29) Hz, and $Q_{10} = +18\ 465(1.7)$ Hz/G^2 with a reduced $\chi^2 = 0.71$

7.3 Systematic Effects

As with the measurements of the Zeeman splittings in $^{138}Ba^{+}$ for the Landé g experiment, we must investigate a number of systematic error sources that could skew our measurement. Because we are finding resonant frequencies between magnetically sensitive transitions, most of these effects will be due to unwanted ac or dc magnetic fields. We will analyze the effects due to magnetic field fluctuation over the course of an experiment, magnetic field gradients, ac-Zeeman effects, ac-Stark effects, and higher order Zeeman effects. At the end of each subsection, if applicable, suggestions for apparatus modifications to reduce these effects are described. These systematic effects are difficult to observe using the ion, so we will attempt to quantify their effects using knowledge from the characterization of the apparatus. In general, it appears that all of these effects are controlled within the statistical uncertainty quoted for W_3, W_2, and W_1.

7.3.1 Magnetic Field Fluctuations

We have accounted for the effects due to the 60/120 Hz oscillating magnetic field in the trap, but not slow drifts in the magnetic field. It has been observed repeatedly that the magnetic field will drift over the time it takes to complete the spectroscopy procedure (approximately an hour). For example, over the course of data taken one day, we saw a slow, linear drift in f_{+1} of approximately 1 000 Hz over the course of four hours, which corresponds to approximately 2 mG at the ion.

The experimental procedure of measuring f_{+1}, f_x, and f_{-1} takes approximately 30 minutes in total. Typically this is broken up into 10 minutes to measure f_{+1} and f_{-1} each, and approximately 15 minutes for the longer interrogation times used for the $\Delta m_F = 0$ transitions. This systematic would manifest itself if there were continuous drift in tending towards higher (or lower) fields over the course of all of the experiments, but this was not observed. The largest drift over the course of a single measurement run, (approximately 30 minutes), corresponds to a 1 mG drift in the ambient magnetic field, leading to at most 60 Hz on the measurement of f_{10}, which is comparable to the uncertainty on the 60/120 Hz correction. These drifts seem to be largely random, so from day to day, this effect will be

averaged over multiple measurements.

The bus system described in Section 4.3.3 still produces fast fluctuations in the magnetic field, but they are on the order of 500 μG, for tens of seconds, which could affect several shelving experiments, but not a frequency scan overall.

To reduce all of these effects, which would be necessary to improve upon the experiment, one should implement the passive magnetic shielding described in 4.3.3, and possibly actively compensate for fluctuations in the ambient magnetic shield as is done in the ^{199}Hg electric dipole moment experiment [72].

7.3.2 Magnetic Field Gradient

The presence of a magnetic field gradient in our ion trap could cause a systematic effect if the ion's trapped position changed over the course of an experiment. Spencer Williams measured a gradient on the trap axis of approximately 150 μG/μm in the axial direction by shifting the trapped ion's position by a known amount measurable on the EMCCD camera, and observing a change in the ^{138}Ba$^+$ $6S_{1/2}$ ground state Zeeman splitting. We do not observe that the ion changes its position by more than 1 μm, over the course of an hour, so the magnetic field should not change by more than 75 μG over an experimental run (approximately 30 minutes). This effect would result in a shift on the order of our statistical uncertainty of the magnetic field calibration, and well below the effects of the 60/120 Hz magnetic field uncertainty.

One can reduce the effects of magnetic field gradients by ensuring that magnetic field coils are made in pairs, arranged in a Helmholtz configuration. In our case, the main magnetic field coils are arranged as shown in Figure 4.10, while the vertical and horizontal trim coils are just single, unpaired coils that have fewer turns and smaller currents to cancel stray vertical and magnetic fields (ensuring optical pumping with good fidelity). Should having magnetic field gradients manifest as a problem in future experiments, one could easily replace single trim coils with pairs instead. One must also concern themselves with how much the ion's trapped position changes over time, though this seems to be sufficient in our current trap.

7.3.3 ac-Zeeman Effects

An ac Zeeman effect occurs whenever there is an oscillating magnetic field that is detuned from a resonance and appear as scalar, vector and tensor shifts, much like the light shifts observed by [66]. We will assume that we have a magnetic field, $\tilde{B}$, that oscillates at frequency $\omega_{\tilde{B}}$, which shifts the energy of a state $|i\rangle$ by:

$$\Delta E_{\mathrm{ac-Zeeman}} = -\frac{\hbar\Omega_{\tilde{B}}^2}{4}\sum_j \left|\left\langle j\right|\hat{J}_q\left|i\right\rangle\right|^2\left(\frac{1}{\omega_{ij}-\omega_{\tilde{B}}}\right) \tag{7.7}$$

where

$$\Omega_{\tilde{B}} = \frac{\mu_B g_J|\tilde{B}|}{\hbar} \tag{7.8}$$

is the Rabi frequency if the oscillating field were on resonance, $\hat{J}_q$ is the rank-q angular momentum operator that depends on the orientation of $\tilde{B}$ with respect to the static magnetic field. The term $\omega_{ij}-\omega_{\tilde{B}}$ is the detuning from the resonance frequency between state $|i\rangle$ and $|j\rangle$. For the rest of the discussion, we will assume that the field is polarized in a way that maximally produces ac-Zeeman effects. This would be circularly polarized for $\hat{J}_{\pm1}$ and linear along the quantization axis for $\hat{J}_0$.

With that discussion in mind, we will look at several potential sources of oscillating magnetic fields observed by the ion, and consider the detuning from various resonances. First, we consider the ion's motion in the magnetic field gradient discussed in the previous section, which is along the axial direction. Since the ion has a finite temperature, it will oscillate at the secular frequency, ω_z, in the magnetic field gradient. Thus, in the frame of the ion, there will be an oscillating magnetic field at $\omega_z \simeq 2\pi \times 410$ kHz. Using the results of Section 5.1, we find that the ion's amplitude of oscillation due to its finite temperature is approximately 81 nm, resulting in $\tilde{B} = 12$ μG. This results in a Rabi frequency $\Omega_{\tilde{B}} = 2\pi \times 1$ Hz. The nearest resonance is between Zeeman sublevels within a given single F, with ω_{ij} of order 1 MHz, thus the detuning is greater than 10 kHz, producing shifts on the order of mHz at most. Shifts between hyperfine levels of different F are even smaller, as the detuning is on the order of 150 MHz at the least. The ion's motion in the radial direction is of similar size, again resulting in negligible shifts.

Another possible effect is due to the ion's micromotion at ω_{rf}, the drive frequency of

the trap, in the magnetic field gradient, or due to unbalanced currents in the trap structure that produce oscillating magnetic fields at the same frequency. We compensate the ion's micromotion to within 1 μm using the compensation electrodes, so again at most the $\tilde{B}$ is 150 μG for the ion's micromotion in the gradient. Our trap for this measurement is driven at $\omega_{\rm rf} \simeq 2\pi \times 12$ MHz, so this effect will be negligible as the detuning from resonance from Zeeman sublevels within a single hyperfine level is approximately 10 MHz, and still > 150 MHz between different hyperfine levels. If there were large uncompensated currents, these would have been observed (but were not) in the Landé-g experiment, because the drive frequency was closer in frequency to the ground state Zeeman resonance.

During the measurement of f_{10} we employ two rf-synthesizers to perform the operations necessary for spectroscopy. The Rabi frequency of the $F = 2, m = 0 \leftrightarrow F = 1, m = 0$ synthesizer when switched on is approximately $2\pi \times 1.5$ kHz. When the rf-switch is off, there is in excess of 70 dB of isolation, indicating that the Rabi frequency is reduced to $2\pi \times 0.5$ Hz, and the detuning is likely on the order of tens to hundreds of Hz. We have not observed this effect at a statistically significant level, but it may need to be considered for future experiments.

7.3.4 ac Stark Shifts

An off-resonant light shift (or ac Stark shift) could arise from leaking laser light that is near resonance to a transition addressing the $5D_{3/2}$ hyperfine level in question. To ensure that this effect is negligible, the 650 nm beams used for repumping were extinguished with a physical shutter. The other transition that could be worrisome is due to the 2051 nm beam, but it is already a weak transition $\Omega \simeq 2\pi \times 8$ kHz, so when shuttered using an AOM operating at 55 MHz, shifts due to this light will again be negligible (less than 1 mHz).

7.3.5 Higher Order Zeeman Effects

At our highest magnetic field, 1.7 G, we should consider higher order Zeeman effects, beyond the quadratic form. To do this, we will use the numerical model described in Section 2.2.4, and compare the analytic quadratic form, to the numerical solution to the com-

plete Hamiltonian. Primarily, this would affect f_{10} as it has the smallest energy denominator $f_{10} \simeq 145$ MHz, and thus mixes $F = 1$ and $F = 0$. At 1.7 G, the difference between the full Hamiltonian solution, and the pure quadratic Zeeman effect was calculated to be approximately 2 Hz for f_{10}, which is, again, negligible compared to the statistical uncertainty in the measurement, as well as the correction term applied. Should one desire to improve the experiment, it will likely be necessary to work at smaller magnetic fields $\boldsymbol{B} < 1$ G, where the correction would be less than 500 mHz.

7.3.6 Summary

To the best of our knowledge, the systematic effects listed are controlled below the level of our statistical uncertainty, and do not pose a problem to this measurement. Should one want to make an improvement by an order of magnitude or more, it will be necessary to rein in the magnetic field drifts, fluctuations, as well as the 60-Hz magnetic field oscillation. It may also be necessary to reduce magnetic field gradients as well as the ion's motion in the trap. Implementing a dark state destabilization scheme [6] may be necessary to work at low enough fields to allow for the highest precision.

7.4 Calculation of Hyperfine Constants

We can now calculate the hyperfine constants, A, B, and C for the $5D_{3/2}$ level of $^{137}Ba^{+}$ using the results of Section 2.2.3, temporarily ignoring 2nd-order theory corrections.

$$A(5D_{3/2}) = \frac{1}{20}W_1 + \frac{4}{25}W_2 + \frac{21}{100}W_3 + \text{2nd order corrections} \tag{7.9}$$

$$B(5D_{3/2}) = -\frac{1}{4}W_1 - \frac{2}{5}W_2 + \frac{7}{20}W_3 + \text{2nd order corrections} \tag{7.10}$$

$$C(5D_{3/2}) = \frac{1}{80}W_1 - \frac{1}{100}W_2 + \frac{1}{400}W_3 + \text{2nd order corrections} \tag{7.11}$$

Plugging in the values from Table 7.1, we obtain the hyperfine constants found in Table 7.2.

To find the nuclear magnetic octupole moment, we need to account for a second-order theory correction, specifically the cross term, ζ, of the magnetic dipole moment (M1) with the electric quadrupole moment (E2). This second order hyperfine shift is derived in [33],

[4], and [3], so we will simply quote the result:

$$C(5D_{3/2}) = \frac{1}{80}W_1 - \frac{1}{100}W_2 + \frac{1}{400}W_3 - \frac{1}{2000\sqrt{21}}\zeta. \tag{7.12}$$

The dipole-quadrupole correction term was calculated in [3] to be

$$-\frac{1}{2000\sqrt{21}}\zeta = 3.17 \text{ Hz}. \tag{7.13}$$

We can extract the nuclear magnetic octupole moment of $^{137}Ba^{+}$using another result of [3][3]:

$$C(5D_{3/2}) + 3.17 \text{ Hz} = 0.581(13)\left(\frac{\Omega}{\mu_N \times \text{b}}\right) \text{ kHz} \tag{7.14}$$

where Ω is the nuclear octupole moment in units of μ_N is the nuclear magneton times b, the barn $= 10^{-24}$ cm^2. Thus, we arrive at our final result:

$$\Omega = 0.0631(12)\mu_N \times \text{b}. \tag{7.15}$$

7.5 Conclusions

Since these hyperfine intervals have been measured by another group in [43], it's possible to directly compare the results. We find that our measurements of f_{32}, f_{21}, and f_{10} all agree to approximately 3-σ. We observe higher statistical uncertainty in each of these zero field splittings by an order of magnitude, largely because we worked at higher magnetic fields, necessary to laser cool $^{137}Ba^{+}$ effieicntly. As a result, the ion was more susceptible to magnetic field fluctuations, which are the dominant source of uncertainties. This suggests that

[3]Note that the sign is reversed from [3] following private communication with Professor Andrei Derevianko.

Hyperfine Constant	Measured Value [Hz]
$A(5D_{3/2})$	189 730 531(1.5)$_{\text{stat}}$
$B(5D_{3/2})$	44 538 767.9(7.1)$_{\text{stat}}$
$C(5D_{3/2})$	33.74(0.36)$_{\text{stat}}$

Table 7.2: Measured Hyperfine Constants for the $5D_{3/2}$ level of $^{137}Ba^{+}$(uncorrected). The 1-σ statistical uncertainties arise from extrapolating to zero-magnetic field.

in order to make a significant improvement, it would be necessary to implement magnetic shielding, so that the ion would experience a quieter magnetic field over the duration of the experiment. In all, we show good agreement in the measurement of the hyperfine splittings, further suggesting that lurking systematics would not be common to two completely disjoint experiments.

The nuclear magnetic octupole moment measured here has a relative uncertainty of 2.5%, which places a good check on the models presented by nuclear and atomic theory. The proposal for this experiment, using the nuclear shell model, predicted that the hyperfine constant $C(5D_{3/2})$ would be -23 Hz [3]. Our result of 33.74 Hz (uncorrected for 2nd order terms in the hyperfine interaction) agrees in sign from the nuclear shell model prediction, following private communications with Professor Andrei Derevianko. Our measurement does not, however, show a nuclear magnetic octupole moment 40 times larger than the nuclear shell model would predict as was observed in [20], nor did the result in [19] so perhaps ^{133}Cs was an anomaly. The recent semi-emperical[4] measurements of nuclear magnetic octupole moments with comparison to nuclear shell model predictions can be found in Table 7.3. In each of these experiments with a prediction, the nuclear shell model underestimates the size of the nuclear magnetic octupole moment.

Table 7.3: Summary of octupole measurements compared to theoretical predictions where available. The size for the ^{137}Ba+ measurements appears to come from a difference in sign for the 2nd order correction term which is explained further in [42].

Atom	Semi-emperical Ω [$\mu_N \times$ b]	Shell Model Prediction Ω [$\mu_N \times$ b]	Reference
^{133}Cs	0.82(10)	0.022	[20]
^{87}Rb	-0.58(39)	0.30	[19]
^{171}Yb	-34.4(21)	—	[70]
^{137}Ba$^+$	0.050 61(56)	—	[42]
^{137}Ba$^+$	0.0631(12)	0.035	This work and [3]

[4]Using the experimentally measured values for C, and using theoretical calculations of the atomic structure to extract Ω.

Chapter 8

CONCLUSIONS AND FUTURE DIRECTIONS

While my personal effort was to measure the hyperfine intervals of $5D_{3/2}$ and along the way measure the Landé g factor of $5D_{5/2}$, this wasn't what the collective *we* set out to do, nor is it the highest reaching fruit on the tree. I would be remiss to not provide at least a cursory discussion of where we are and where we are going with regards to a measurement of parity nonconservation (PNC) in Ba^+, as we have had a few discussions of several nice stepping stone measurements.

8.1 Parity Nonconservation in Ba^+

There are a few reasons why one would want to pursue a measurement of PNC in Ba^+, and it frequently resurfaces as a topic of theoretical and experimental interest at every conference I have attended to date. The fact of the matter is that it is a difficult measurement, but that should not dissuade future researchers to continue the progress which has been underway since it was originally proposed by Fortson in 1993 [18]. To date, there has still only been a single measurement of parity violation in atomic systems, namely [84], but experiments in Yb^+ [58], and in Ra^+ [77] appear to still be progressing. The astute reader will notice that these are all heavy ions, with large atomic number, Z.

We should first look at the theoretical foundation of these PNC experiments, namely, that the weak interaction does not conserve parity symmetry and this can manifest itself by allowing forbidden transitions to occur. How this manifests itself in Ba^+ is that for the $6S_{1/2}$ level, the valence electron has a nonzero probability of being inside the nucleus, thus $|\psi(0)|^2 \neq 0$. While it is there, it can exchange a virtual Z_0 vector boson with a quark, which mixes $6P_{1/2}$ with $6S_{1/2}$, so that the ground state becomes:

$$6S_{1/2} + i\epsilon_{\mathrm{PNC}}\ 6P_{1/2}, \tag{8.1}$$

where $\epsilon_{\mathrm{PNC}} \sim \mathcal{O}(10^{-11})$. The ground state that was previously considered to be only parity

even, now has a tiny component that is parity-odd. The electromagnetic interactions, however, *must* conserve parity. So, driving a transition forbidden by parity symmetry considerations is a result of the parity nonconserving weak interaction in the nucleus. It is well known that these parity violating matrix elements scale with Z^3 (for example, see, [31]), so using heavy ions, like Ba^+ ($Z = 56$), Yb^+ ($Z = 70$), and Ra^+ ($Z = 88$) take advantage of this scaling. As with many experiments, there are advantages and disadvantages with a candidate species for experimental reasons, but we will limit our discussion to Ba^+.

The matrix element for our transition between the ground state (now with a small admixture of $6P_{1/2}$) and the the long lived $5D_{3/2}$ level has the following form:

$$\left\langle 6S_{1/2}\right| \hat{E2} + \hat{M1} \left|5D_{3/2}\right\rangle + \left\langle 6P_{1/2}\right| \epsilon_{PNC}\ \hat{E1} \left|5D_{3/2}\right\rangle, \tag{8.2}$$

where we haven't been careful about phase relations. Thus, the transition between $6S_{1/2}$ and $5D_{3/2}$ can be driven by either an electric quadrupole transition (E2) or a magnetic dipole transition (M1), and from the parity violating term $6P_{1/2} \leftrightarrow 5D_{3/2}$ can be driven by an electric dipole transition (E1). Each separate matrix element can be written as a Rabi frequency, such that Ω_{E2} is the electric quadrupole contribution, Ω_{M1} is the magnetic dipole contrbution, and Ω_{PNC} is the parity violating electric dipole contribution. These will all interfere in the total Rabi frequency of the transition, Ω, so that keeping the leading terms:

$$\Omega^2 = |\Omega_{E2} + \Omega_{M1} + \Omega_{\mathrm{PNC}}|^2 = \Omega_{E2}^2 + \Omega_{M1}^2 \pm 2\mathrm{Re}\left(\Omega_{E2}\Omega_{\mathrm{PNC}}^*\right) \pm 2\mathrm{Re}\left(\Omega_{E2}\Omega_{M1}^*\right). \tag{8.3}$$

Since $\Omega_{E2} \gg \Omega_{M1} \gg \Omega_{PNC}$, the large E2 amplitude both enhances the PNC term (which is good), and the M1 term (which could mimic the PNC effect and pose serious problems to the experiment). Theorists have made several predictions for what this magnetic dipole transition amplitude should be, as in [62] and [22]. The problem with this involves the scale of these Rabi frequencies. If we look at the magnitude of each of the terms in Equation 8.3, we find that the E2-E1$_{\mathrm{PNC}}$ interference term (what one would like to measure) is reduced in magnitude by $\mathcal{O}(10^{-7})$ from Ω_{E2}^2. The parity violating term is also dominated by the E2-M1 interference which has a magnitude of $\mathcal{O}(10^{-2})$ in the worst possible configuration. Thus if we have light that inadvertently contributes to Ω_{M1}, it could pose serious problems as this could mimic and drown out the miniscule parity-violating term.

The experimental procedure requires a number of reversals of the laser fields at the ion's position to check for the small parity violating contribution to the Rabi frequency. This requires nearly perfect control of the 2051 nm beam polarization, which is no small feat for the experimenters in general, but is made more difficult by the fact that the ion is surrounded by a vacuum chamber, with glass viewports that have undergone torques when attached to the vacuum chamber, and heated / cooled during the trap bakeout to 150°C necessary to achieve UHV. We have already observed that the stress in these viewports can induce birefringence as shown in [80], which will introduce a phase retardance along some stressed axis (or even worse, a polarization gradient across the beam itself).

The experimenter must then ask themselves how pure the polarization needs to be. Is it 100:1, 100,000:1, or even better? The answer hinges on the magnitude of M1, and the fact of the matter is that no one has measured this transition amplitude. Should theorists have overestimated M1, then the constraints are lessened for the experimenter, but if they have underestimated, then it could be an even more difficult experiment than we previously thought. To settle this debate and determine how to proceed, we have already developed much of the apparatus necessary to perform the M1 amplitude measurement, as well as proposed an experimental procedure in [80].

Ultimately the experimental measurement of M1 will be left on the shoulders of Spencer Williams, who has already made advances on this front by rotating a linearly polarized (or slightly elliptically polarized) 2051 nm laser beam, and measuring the Rabi frequency as a function of the polarization angle with respect to the quantization axis. This can be used to calibrate the polarization and alignment angles with respect to the the magnetic field at the site of the ion (see Figure 2.6), as well as show how much ellipticity is introduced by the viewport. This work lets us get a handle on how the polarization is affected by the interaction with the glass in the viewport, using the ion as the sensor.

This work to measure M1 and ultimately PNC will require a very stable magnetic field, the ability to vary the angle of the 2051 nm laser's orientation with respect to the quantization axis, and excellent control of the laser's polarization. To this end, the magnetic shield described in Chapter 4 will be absolutely necessary for the future experiments, because the magnetic field fluctuations simply introduce too many problems for the experimenter.

As a final note, the original proposal by Fortson [18], requires that the experimenter construct an optical cavity within the vacuum chamber to create a strong standing wave of 2051 nm radiation. At this point, one can measure a light shift arising from PNC depending on the phase of the electric fields used to enhance E2 and $E1_{PNC}$ (see [66] for more details). Demonstration of ions trapped in an optical cavity has been shown in many experiments, for example, [8], and a similar effort must be undertaken within our laboratory to develop the ability to create a standing wave of 2051 nm radiation such that there is node, or anti-node at the site of the ion. In the mean time, it seems that observing a light shift using rf spectroscopy caused by a near-resonant 2051 nm running wave would be a nice next step towards the full PNC experiment.

I have absolutely no qualms saying that the path ahead for this experiment (and experimenters!) will be challenging experimentally and theoretically. At the time of this manuscript, no problems that have surfaced that would make the experiment impossible for a technical reason, so progress will continue slowly but surely. Though it won't be my own adventure, I am confident that future students will take the torch carried by many past experimenters and continue the adventure begun so many years ago.

BIBLIOGRAPHY

[1] L Allen and JH Eberly. *Optical Resonance, Two-Level Atoms*. Dover, New York, 1975.

[2] L. Armstrong. *Theory of the hyperfine structure of free atoms*. Wiley-Interscience, 1971.

[3] K. Beloy, A. Derevianko, V. A. Dzuba, G. T. Howell, B. B. Blinov, and E. N. Fortson. Nuclear magnetic octupole moment and the hyperfine structure of the $5D_{3/2,5/2}$ states of the Ba^+ ion. *Phys. Rev. A*, 77(5):052503, May 2008.

[4] K. Beloy, A. Derevianko, and W. R. Johnson. Hyperfine structure of the metastable $^3P_2$ state of alkaline-earth-metal atoms as an accurate probe of nuclear magnetic octupole moments. *Phys. Rev. A*, 77:012512, Jan 2008.

[5] Giel Berden, Rudy Peeters, and Gerard Meijer. Cavity ring-down spectroscopy: Experimental schemes and applications. *International Reviews in Physical Chemistry*, 19(4):565–607, 2000.

[6] D. J. Berkeland and M. G. Boshier. Destabilization of dark states and optical spectroscopy in zeeman-degenerate atomic systems. *Phys. Rev. A*, 65:033413, Feb 2002.

[7] DJ Berkeland, JD Miller, JC Bergquist, WM Itano, and DJ Wineland. Minimization of ion micromotion in a paul trap. *Journal of Applied Physics*, 83(10):5025–5033, 1998.

[8] B. Casabone, A. Stute, K. Friebe, B. Brandstätter, K. Schüppert, R. Blatt, and T. E. Northup. Heralded entanglement of two ions in an optical cavity. *Phys. Rev. Lett.*, 111:100505, Sep 2013.

[9] Claude Cohen-Tannoudji. *Atom-Photon Interactions: Basic Processes and Applications*. Wiley, New York, 1992.

[10] S. T. Cundiff and J. Ye. Colloquium: Femtosecond optical frequency combs. *Reviews of Modern Physics*, 75:325–342, March 2003.

[11] J. J. Curry. Compilation of wavelengths, energy levels, and transition probabilities for ba i and ba ii. *Journal of Physical and Chemical Reference Data*, 33(3):725–746, 2004.

[12] U. Dammalapati, S. De, K. Jungmann, and L. Willmann. Isotope shifts of 6s5d3d-6s6p1p1 transitions in neutral barium. *The European Physical Journal D*, 53(1):1–8, 2009.

[13] W. Demtröder. *Atoms, Molecules, and Photons*. Springer, 2006.

[14] Ralph G. DeVoe and Christian Kurtsiefer. Experimental study of anomalous heating and trap instabilities in a microscopic ^{137}Ba ion trap. *Phys. Rev. A*, 65:063407, Jun 2002.

[15] Matthew R. Dietrich. *Barium ions for quantum computation*. PhD thesis, University of Washington, Seattle, WA 98195, 2009.

[16] R. W. P. Drever, J. L. Hall, F. V. Kowalski, J. Hough, G. M. Ford, A. J. Munley, and H. Ward. Laser phase and frequency stabilization using an optical resonator. *Applied Physics B: Lasers and Optics*, 31(2):97–105, June 1983.

[17] Christopher J. Foot. *Atomic Physics*. Oxford University Press, New York, NY, 2005.

[18] Norval Fortson. Possibility of measuring parity nonconservation with a single trapped atomic ion. *Phys. Rev. Lett.*, 70(16):2383–2386, Apr 1993.

[19] V Gerginov, C E Tanner, and W R Johnson. Observation of the nuclear magnetic octupole moment of 87rb from spectroscopic measurements of hyperfine intervals. *Canadian Journal of Physics*, 87(1):101–104, 2009.

[20] Vladislav Gerginov, Andrei Derevianko, and Carol E. Tanner. Observation of the nuclear magnetic octupole moment of Cs133. *Phys. Rev. Lett.*, 91(7):072501, Aug 2003.

[21] P.K. Ghosh. *Ion Traps*. International series of monographs on physics. Clarendon Press, 1995.

[22] G. H. Gossel, V. A. Dzuba, and V. V. Flambaum. Calculation of strongly forbidden $m1$ transitions and g-factor anomalies in atoms considered for parity-nonconservation measurements. *Phys. Rev. A*, 88:034501, Sep 2013.

[23] Kurt Gottfried and Tung-Mow Yan. *Quantum Mechanics: Fundamentals*. Springer-Verlag, New York, NY, 2004.

[24] P. Grundevik, M. Gustavsson, G. Olsson, and T. Olsson. Hyperfine-structure and isotope-shift measurements in the $6s5d \leftrightarrow 6p5d$ transitions of ba i in the far-red spectral region. *Z. Phys. A*, 312(1–2):1–9, 1983.

[25] T.W. Hansch and B. Couillaud. Laser frequency stabilization by polarization spectroscopy of a reflecting reference cavity. *Optics Communications*, 35(3):441 – 444, 1980.

[26] A. Härter, A. Krükow, A. Brunner, and J. Hecker Denschlag. Long-term drifts of stray electric fields in a paul trap. *Applied Physics B*, 114(1-2):275–281, 2014.

[27] Matthew R. Hoffman, Thomas W. Noel, Carolyn Auchter, Anupriya Jayakumar, Spencer R. Williams, Boris B. Blinov, and E. N. Fortson. Radio-frequency-spectroscopy measurement of the Landé g_j factor of the $5D_{5/2}$ state of Ba^+ with a single trapped ion. *Phys. Rev. A*, 88:025401, Aug 2013.

[28] John David Jackson. *Classical Electrodynamics*. John Wiley and Sons, Hoboken, NJ, 1999.

[29] S. R. Jefferts, T. P. Heavner, T. E. Parker, and J. H. Shirley. Nist cesium fountains: current status and future prospects. In *Proceedings of SPIE 6673, Time and Frequency Metrology*, volume 6673, pages 667309–667309–9, 2007.

[30] Hans Karlsson and Ulf Litzén. Revised ba i and ba ii wavelengths and energy levels derived by fourier transform spectroscopy. *Physica Scripta*, 60(4):321, 1999.

[31] I.B. Khriplovich and S.K. Lamoreaux. *CP Violation Without Strangeness: Electric Dipole Moments of Particles, Atoms, and Molecules*. Texts and monographs in physics. Springer-Verlag, 1997.

[32] A. Kleczewski, M. Hoffman, E. Magnuson, B. Blinov, and N. Fortson. Frequency doubling and stabilization of a Tm,Ho:YLF laser at 2051 nm to a high finesse optical cavity. *ArXiv e-prints*, May 2011.

[33] Adam Kleczewski. *Towards a measurement of the nuclear magnetic octupole moment of barium-137*. PhD thesis, University of Washington, Seattle, WA 98195, 2011.

[34] Adam Kleczewski, Matthew R. Hoffman, J. A. Sherman, Eric Magnuson, B. B. Blinov, and E. N. Fortson. Coherent excitation of the $6S_{1/2}$ to $5D_{3/2}$ electric-quadrupole transition in $^{138}ba^+$. *Phys. Rev. A*, 85:043418, Apr 2012.

[35] H. Knab, K.H. Knöll, F. Scheerer, and G. Werth. Experimental ground state g_j factor of ba+ in a penning ion trap. *Zeitschrift für Physik D Atoms, Molecules and Clusters*, 25(3):205–208, 1993.

[36] K. H. Knöll, G. Marx, K. Hübner, F. Schweikert, S. Stahl, Ch. Weber, and G. Werth. Experimental g_J factor in the metastable $5d_{3/2}$ level of ba^+. *Phys. Rev. A*, 54(2):1199–1205, Aug 1996.

[37] Timo W. Koerber. *Measurement of light shift ratios with a single trapped $^{138}Ba^+$ ion and prospects for a parity violation experiment*. PhD thesis, University of Washington, Seattle, WA 98195, 2003.

[38] N. Kurz, M. R. Dietrich, Gang Shu, R. Bowler, J. Salacka, V. Mirgon, and B. B. Blinov. Measurement of the branching ratio in the $6p_{3/2}$ decay of *baii* with a single trapped ion. *Phys. Rev. A*, 77(6):060501, Jun 2008.

[39] N. Kurz, M. R. Dietrich, Gang Shu, T. Noel, and B. B. Blinov. Measurement of the landé g factor of the $5D_{5/2}$ state of ba ii with a single trapped ion. *Phys. Rev. A*, 82:030501, Sep 2010.

[40] X. Lacour, S. Guérin, L. P. Yatsenko, N. V. Vitanov, and H. R. Jauslin. Uniform analytic description of dephasing effects in two-state transitions. *Phys. Rev. A*, 75(3):033417, Mar 2007.

[41] P. Laporta, M. Marano, L. Pallaro, and S. Taccheo. Amplitude and frequency stabilisation of a tm–ho:yag laser for coherent lidar applications at 2.1 m. *Optics and Lasers in Engineering*, 37(5):447 – 457, 2002.

[42] Nicholas C. Lewty, Boon Leng Chuah, Radu Cazan, Murray D. Barrett, and B. K. Sahoo. Experimental determination of the nuclear magnetic octupole moment of $^{137}ba^{+}$ ion. *Phys. Rev. A*, 88:012518, Jul 2013.

[43] Nicholas C. Lewty, Boon Leng Chuah, Radu Cazan, B. K. Sahoo, and M. D. Barrett. Spectroscopy on a single trapped $137ba^{+}$; ion for nuclear magnetic octupole moment determination. *Opt. Express*, 20(19):21379–21384, Sep 2012.

[44] E. Lindroth and A. Ynnerman. *Ab initio* calculations of g_j factors for li, be^{+}, and ba^{+}. *Phys. Rev. A*, 47:961–970, Feb 1993.

[45] B. K. Mani and D. Angom. Atomic properties calculated by relativistic coupled-cluster theory without truncation: Hyperfine constants of mg^{+}, ca^{+}, sr^{+}, and ba^{+}. *Phys. Rev. A*, 81:042514, Apr 2010.

[46] G. Marx, G. Tommaseo, and G. Werth. Precise g_j- and g_i-factor measurements of ba+ isotopes. *The European Physical Journal D - Atomic, Molecular, Optical and Plasma Physics*, 4(3):279–284, 1998.

[47] I. Marzoli, J. I. Cirac, R. Blatt, and P. Zoller. Laser cooling of trapped three-level ions: Designing two-level systems for sideband cooling. *Phys. Rev. A*, 49:2771–2779, Apr 1994.

[48] P. J. Mohr, B. N. Taylor, and D. B. Newell. CODATA recommended values of the fundamental physical constants: 2010. *Reviews of Modern Physics*, 84:1527–1605, October 2012.

[49] Warren Nagourney, Jon Sandberg, and Hans Dehmelt. Shelved optical electron amplifier: Observation of quantum jumps. *Phys. Rev. Lett.*, 56(26):2797–2799, Jun 1986.

[50] T. Noel, M. R. Dietrich, N. Kurz, G. Shu, J. Wright, and B. B. Blinov. Adiabatic passage in the presence of noise. *Phys. Rev. A*, 85:023401, Feb 2012.

[51] Thomas W. Noel. *Ion Photon Entanglement with Barium*. PhD thesis, University of Washington, Seattle, WA 98195, 2014.

[52] Mark Notcutt, Long-Sheng Ma, Jun Ye, and John L. Hall. Simple and compact 1-Hz laser system via an improved mounting configuration of a reference cavity. *Opt. Lett.*, 30(14):1815–1817, 2005.

[53] Hilmar Oberst. *Resonance fluorescence of single barium ions*. PhD thesis, Universität Innsbruck, A-6020 Innsbruck, Austria, 1999.

[54] B. Odom, D. Hanneke, B. D'Urso, and G. Gabrielse. New measurement of the electron magnetic moment using a one-electron quantum cyclotron. *Phys. Rev. Lett.*, 97:030801, Jul 2006.

[55] Wolfgang Paul. Electromagnetic traps for charged and neutral particles. *Rev. Mod. Phys.*, 62:531–540, Jul 1990.

[56] E H Pinnington, R W Berends, and M Lumsden. Studies of laser-induced fluorescence in fast beams of sr + and ba + ions. *Journal of Physics B: Atomic, Molecular and Optical Physics*, 28(11):2095, 1995.

[57] O. Poulsen and P. S. Ramanujam. Time-differential level-crossing g-value measurements of the $6p^2p$ fine-structure levels in ^{138}Baii using an optical-induced orientation or alignment of a fast ionic beam. *Phys. Rev. A*, 14:1463–1467, Oct 1976.

[58] S. Rahaman, J. Danielson, M. Schacht, M. Schauer, J. Zhang, and J. Torgerson. MW-Optical Double Resonance in $\hat{}\{171\}\{Yb\}\hat{}+$ Trapped Single Ion and its Application for Precision Experiments. *ArXiv e-prints*, April 2013.

[59] L. Ricci, M. Weidemüller, T. Esslinger, A. Hemmerich, C. Zimmermann, V. Vuletic, W. König, and T.W. Hänsch. A compact grating-stabilized diode laser system for atomic physics. *Optics Communications*, 117(5–6):541 – 549, 1995.

[60] C Roos. *Controlling the quantum state of trapped ions*. PhD thesis, Karl-Franzens-Univ. Graz, Graz, 2000.

[61] U. I. Safronova. Relativistic many-body calculation of energies, lifetimes, hyperfine constants, multipole polarizabilities, and blackbody radiation shift in ^{137}Ba ii. *Phys. Rev. A*, 81:052506, May 2010.

[62] B. K. Sahoo, Md. R. Islam, B. P. Das, R. K. Chaudhuri, and D. Mukherjee. Lifetimes of the metastable $^2d_{32,52}$ states in ca^+, sr^+, and ba^+. *Phys. Rev. A*, 74:062504, Dec 2006.

[63] Bijaya K. Sahoo, Geetha Gopakumar, Rajat K. Chaudhuri, B. P. Das, Holger Merlitz, Uttam Sinha Mahapatra, and Debashis Mukherjee. Magnetic dipole hyperfine interactions in $^{137}ba^+$ and the accuracies of the neutral weak interaction matrix elements. *Phys. Rev. A*, 68:040501, Oct 2003.

[64] Bijaya Kumar Sahoo. Relativistic coupled-cluster theory of quadrupole moments and hyperfine structure constants of $5d$ states in ba^+. *Phys. Rev. A*, 74:020501, Aug 2006.

[65] J. J. Sakurai. *Modern Quantum Mechanics*. Addison-Wesley, 1994.

[66] Jeffrey A. Sherman. *Single barium ion spectroscopy: light shifts, hyperfine structure, and progress on an optical frequency standard and atomic parity violation*. PhD thesis, University of Washington, Seattle, WA 98195, 2007.

[67] Bruce W. Shore. *The Theory of Coherent Atomic Excitation*, volume 2. Wiley-Interscience, New York, NY, 1990.

[68] Gang Shu. *Novel Ion Traps for Enhanced Fluorescence Collection and Single Photon Sources Based on Barium Ions*. PhD thesis, University of Washington, Seattle, WA 98195, 2010.

[69] R.E. Silverans, G. Borghs, P. De Bisschop, and M. Van Hove. Hyperfine structure of the 5d ^2d_J states in the alkaline-earth ba ion by fast-ion-beam laser-rf spectroscopy. *Phys. Rev. A*, 33:2117–2120, March 1986.

[70] Alok Singh, D. Angom, and Vasant Natarajan. Observation of the nuclear magnetic octupole moment of ^{173}yb from precise measurements of the hyperfine structure in the $^3P_2$ state. *Phys. Rev. A*, 87:012512, Jan 2013.

[71] A. V. Steele, L. R. Churchill, P. F. Griffin, and M. S. Chapman. Photoionization and photoelectric loading of barium ion traps. *Phys. Rev. A*, 75:053404, May 2007.

[72] M. D. Swallows, T. H. Loftus, W. C. Griffith, B. R. Heckel, E. N. Fortson, and M. V. Romalis. Techniques used to search for a permanent electric dipole moment of the ^{199}hg atom and the implications for *CP* violation. *Phys. Rev. A*, 87:012102, Jan 2013.

[73] R C Thompson. Precision measurement aspects of ion traps. *Measurement Science and Technology*, 1(2):93, 1990.

[74] S. Trapp, G. Marx, G. Tommaseo, A. Klaas, A. Drakoudis, G. Revalde, G. Szawiola, and G. Werth. Hyperfine structure and g factor measurements on ba+ and eu+ isotopes. *Hyperfine Interactions*, 127(1-4):57–64, 2000.

[75] William L. Trimble. *High-resolution spectroscopy of $^{115}In^{+}$ and prospects for an indium ion optical frequency reference.* PhD thesis, University of Washington, Seattle, WA 98195, 2007.

[76] M. Van Hove, G. Borghs, P. De Bisschop, and R.E. Silverans. Hyperfine structure of 5d 2 d 3/2 135,137ba ions by collinear fast beam laser-rf double resonance spectroscopy. *Zeitschrift für Physik A Atoms and Nuclei*, 321(2):215–219, 1985.

[77] O.O. Versolato, L.W. Wansbeek, G.S. Giri, J.E.vanden Berg, D.J.vander Hoek, K. Jungmann, W.L. Kruithof, C.J.G. Onderwater, B.K. Sahoo, B. Santra, P.D. Shidling, R.G.E. Timmermans, L. Willmann, and H.W. Wilschut. Atomic parity violation in a single trapped radium ion. *Hyperfine Interactions*, 199(1-3):9–19, 2011.

[78] P Villemoes, A Arnesen, F Heijkenskjold, and A Wannstrom. Isotope shifts and hyperfine structure of 134-138 ba ii by fast ion beam-laser spectroscopy. *Journal of Physics B: Atomic, Molecular and Optical Physics*, 26(22):4289, 1993.

[79] K. Wendt, S.A. Ahmad, F. Buchinger, A.C. Mueller, R. Neugart, and E.-W. Otten. Relativistic j-dependence of the isotope shift in the 6s-6p doublet of ba ii. *Zeitschrift für Physik A Atoms and Nuclei*, 318(2):125–129, 1984.

[80] Spencer R. Williams, Anupriya Jayakumar, Matthew R. Hoffman, Boris B. Blinov, and E. N. Fortson. Method for measuring the $6S_{1/2} \leftrightarrow 5D_{3/2}$ magnetic-dipole-transition moment in ba^{+}. *Phys. Rev. A*, 88:012515, Jul 2013.

[81] D. J. Wineland, R. E. Drullinger, and F. L. Walls. Radiation-pressure cooling of bound resonant absorbers. *Phys. Rev. Lett.*, 40:1639–1642, Jun 1978.

[82] D. J. Wineland and Wayne M. Itano. Laser cooling of atoms. *Phys. Rev. A*, 20:1521–1540, Oct 1979.

[83] DJ Wineland, C Monroe, WM Itano, D Leibfried, BE King, and DM Meekhof. Experimental issues in coherent quantum-state manipulation of trapped atomic ions. *Journal of Research of the National Institute of Standards and Technology*, 103(3), 1998.

[84] C. S. Wood, S. C. Bennett, D. Cho, B. P. Masterson, J. L. Roberts, C. E. Tanner, and C. E. Wieman. Measurement of parity nonconservation and an anapole moment in cesium. *Science*, 275(5307):1759–1763, 1997.

[85] G.K. Woodgate. *Elementary Atomic Structure*. Oxford University Press, USA, 1980.

[86] N. Yu, W. Nagourney, and H. Dehmelt. Radiative lifetime measurement of the Ba^+ metastable $D_{3/2}$ state. *Phys. Rev. Lett.*, 78(26):4898–4901, Jun 1997.

Appendix A

650 NM SIDE-OF-THE-FRINGE LOCKING CIRCUIT

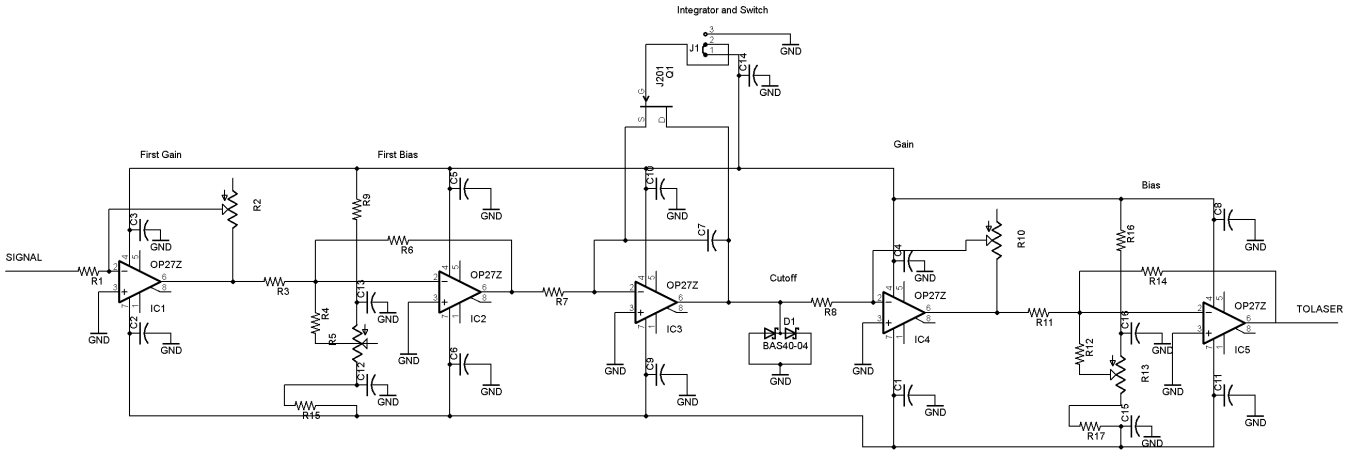

Figure A.1: Circuit diagram for the 650 nm laser side-of-the-fringe lock. The first two operational amplifier stages set the gain and offset for the photodiode signal. The third op-amp is an integration stage that will maintain the side-of-the-fringe lock. The last two stages set the overall offset and locking range for the circuit. A switch lets the user reset the integrator, and relock the circuit manually. Detailed values for resistors, potentiometers, and other circuit elements can be found in the laboratory notebooks.

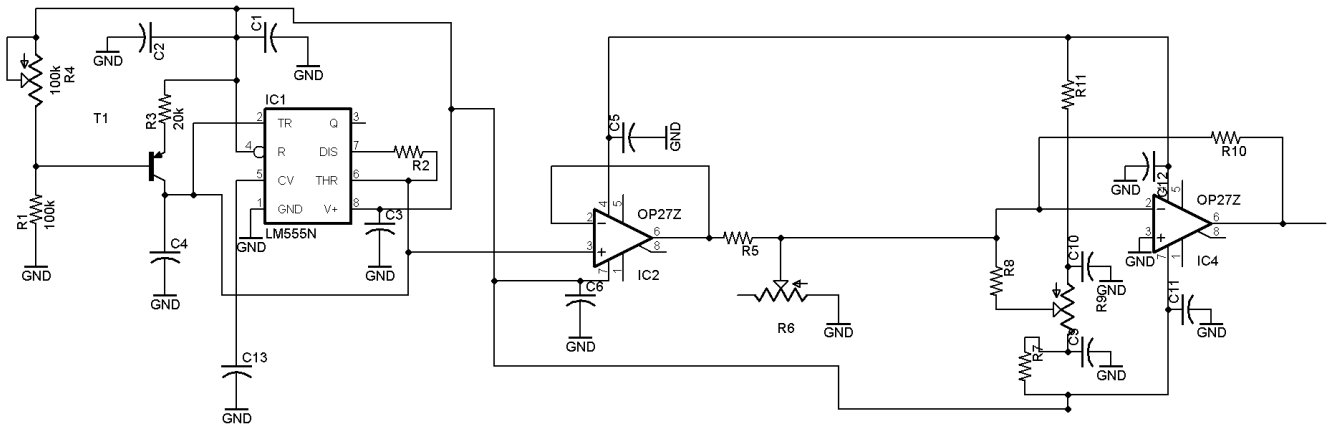

Figure A.2: Circuit diagram for the 650 nm laser frequency sweep circuit used when aligning light into the optical reference cavity. A variable frequency sawtooth wave is generated from the LM555, that is amplified and offset using two operational amplifiers. This lets us ramp the laser's frequency from low to high over a user-set range to ensure that it sweeps over a full free spectral range of a cavity. Detailed values for resistors, potentiometers and other circuit elements can be found in the laboratory notebooks.

VITA

Matthew Hoffman was born to Kirk and Linda Hoffman in Denver, Colorado. He attended the University of Puget Sound in Tacoma, WA and dabbled with atomic physics, working on a project to build a laboratory demonstration of the Zeeman effect in sodium for upper-level classes with Professor Alan Thorndike. He also took a summer jaunt to Menlo Park, CA where he did a National Science Foundation Research Experience for Undergraduates with Dr. Dusan Pejakovic observing vibrational levels of oxygen molecules at SRI International. After graduating with a Bachelor of Science in physics, he returned back to Colorado, and briefly attended the University of Colorado at Boulder, helping to rebuild a disassembled ultrafast laser in Professor Steve Cundiff's group at JILA. This sealed his interest in atomic physics and lasers, so he immediately joined Boris Blinov's group before his first quarter as a graduate student at the University of Washington even began.